**Ana Sofia Rodrigues Machado**

Mestre em Engenharia Biológica

# LocoMouse: a novel system for studying the role of cerebellum in gait coordination

Dissertação para obtenção do Grau de Doutor em Bioengenharia (MIT)

Universidade do Minho

Orientador: Megan Rose Carey, Ph.D.,
Investigadora Principal
Champalimaud Center for the Unknown

Co-orientador: Manuel Nunes da Ponte, Ph.D.,
Professor Catedrático
Universidade Nova de Lisboa

TÉCNICO
LISBOA

Júri:

Presidente: Prof. Doutora Maria Luísa Dias de Carvalho de Sousa Leonardo
Arguentes: Doutor César Miguel Pereira Soares Mendes
Doutor Paulo de Castro Aguiar

Vogais: Doutor Rui Manuel Marques Fernandes da Costa
Doutor Michael Brian Orger
Prof. Doutor Hugo Filipe Silveira Gamboa

FACULDADE DE
CIÊNCIAS E TECNOLOGIA
UNIVERSIDADE NOVA DE LISBOA

**Dezembro 2016**

**LocoMouse: a novel system for studying the role of cerebellum in gait coordination**

Copyright © Ana Sofia Rodrigues Machado, Faculty of Sciences and Technology, NOVA University of Lisbon.

The Faculty of Sciences and Technology and the NOVA University of Lisbon have the right, perpetual and without geographical boundaries, to file and publish this dissertation through printed copies reproduced on paper or on digital form, or by any other means known or that may be invented, and to disseminate through scientific repositories and admit its copying and distribution for non-commercial, educational or research purposes, as long as credit is given to the author and editor.

This work was developed in the context of the MIT Portugal Program, area of Bioengineering Systems, in collaboration with the Champalimaud Research Programme, Champalimaud Center for the Unknown, Lisbon, Portugal. The project entitled *LocoMouse: a novel system for studying the role of cerebellum in gait coordination* was carried out at the Champalimaud Research Programme, Champalimaud Center for the Unknown, Lisbon, Portugal, under the scientific supervision of Megan R. Carey, Ph.D, and under the guidance of the Thesis Committee composed by Rui M. Costa, Ph.D, and Michael B. Orger, Ph.D. This work was supported by the fellowship SFRH/BD/51210/2010 from Fundação para a Ciência e Tecnologia, Portugal, to Ana Machado and by the Starting Grant from the European Research Council to Megan R. Carey.

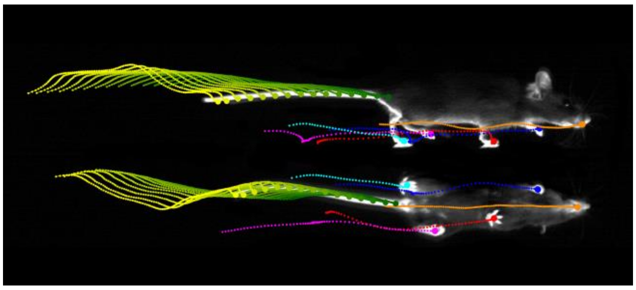

Para a minha família: *Tiago, Irmãos*
*e Pais*

# Acknowledgements

First, I would like to thank my supervisor Megan Carey for the unique opportunity to conduct my research in her lab. Her supervision and support was key in many moments of my thesis and life. I would like to thank her for all the guidance, good advice and friendship. Thank you!

I would like to thank Rui Costa and Michael Orger for all support, guidance and inspiration. I also thank Prof. Manuel Nunes da Ponte and Prof José Silva Lopes for all support.

A special thank you to all the people in the lab. Without your help, this would not have been possible. A thank you to Dana for good discussions and conversations, to João Fayad for patient and support, to Hugo for positive spirit, to Catarina for good advice (old buddy), to Ritinha for kindness, for to Dominique for guidance, to Jovin for your smile, to Tracy for support and kindness, to Dennis for support and to João C, Hugo, Jorge, Carla, Vinay, Inês P, Inês V, Marina, Ana C for the valuable contributions to this project. A special thank you to Tati for all the friendship, kindness and all the runs that we did together. The 10k would not have been possible without you.

Gostaria de agradecer os meus amigos de infância; à Diana A, à Diana B, à Vanessa, ao Moniz, à Sofia S. Aos amigos da faculdade; à Maria Joana (por estar sempre lá), à Sofia (a primeira mamã das 4), à Vânia (a destemida). Às meninas da D. Esperanza; à Patrícia e especialmente à Gé pelas palavras de apoio e pelas caminhadas por Algés.

Um agradecimento especial à minha família. Ao meu irmão mais novo “puto”, ao meu irmão mais velho e à minha mãe e ao meu pai pelo apoio e pela amizade. Um agradecimento especial, ao Vasco, à Natália e ao Diogo, pelas idas ao Leroy, pela amizade, pela paciência e por estarem sempre presentes.

Por fim, um agradecimento especial ao Tiago por acreditares em mim e em nós, pelo nosso Newton, por seres a minha casa.

# Abstract

Smooth and efficient walking requires the coordination of movement across different parts of the body. The cerebellum plays an important role in this process, yet the specific neural circuit mechanisms of whole-body coordination are poorly understood. Although sophisticated genetic tools exist to manipulate the cerebellar circuit in mice, analyses of mouse gait have typically been limited to gross performance measures and lack detail about precision and timing of limb movements.

In this project, I developed an automated, high-throughput, markerless 3D tracking system (LocoMouse) for quantifying locomotion in freely walking mice. Using LocoMouse, I showed that locomotor parameters for individual limbs vary systematically with mouse walking speed and body size. In visibly ataxic Purkinje cell degeneration (*pcd*) and *reeler* mice, I found that 3D limb trajectories and, especially, interlimb and whole-body coordination are specifically impaired. Our findings suggest a failure to predict the consequences of movement across joints, limbs, and body. These experiments were essential to establish a quantitative framework for whole-body locomotor coordination in mice (Machado, Darmohray et al. eLife 2015).

The LocoMouse system was then combined with optogenetic tools to ask how different output regions of the cerebellum differentially contribute to locomotor coordination. I expressed ChR2 in Purkinje cells and stimulated their terminals in the medial, interposed, and lateral cerebellar nuclei of freely walking mice. Here, I identified locomotor parameters that were specifically related to the manipulation of each nucleus. Acute disruption of neural activity in medial and interposed nuclei immediately perturbed ongoing locomotion. In contrast, similar manipulation of Purkinje cell inputs to the lateral nucleus had no observable effect on ongoing locomotor behavior. These results are broadly consistent with previous anatomical and lesion studies suggesting a medial-to-lateral functional organization of cerebellar outputs.

Taken together, these experiments isolated impairments in interlimb and whole-body coordination in mice with cerebellar manipulations. In contrast, spinal cord mutant mice revealed impairments at the intralimb level with no alteration in the interlimb coordination. I characterized distinct motor deficits associated with manipulations in different brain regions and identified and quantified core features of cerebellar ataxia in mice. These experiments establish the LocoMouse system, combined with genetic manipulations, as a powerful system to dissect cerebellar circuit mechanisms of coordinated locomotion.

**Keywords**: Motor coordination, ataxia, cerebellum, motor quantification

# Resumo

O cerebelo desempenha um papel importante na coordenação do movimento das diferentes partes do corpo durante a locomoção. No entanto, os mecanismos neuronais cerebelares associados à coordenação motora são desconhecidos. Embora existam ferramentas genéticas sofisticadas para manipular o circuito cerebelar, a análise quantitativa da coordenação motora em ratinhos ainda é limitativa.

Neste projeto desenvolvi um sistema para analisar e quantificar a locomoção em ratinhos – o LocoMouse. O sistema deteta automaticamente (sem marcadores) as diferentes partes do corpo e regista as suas trajetórias a 3 dimensões com elevada resolução. Com o LocoMouse verificou-se que os parâmetros locomotores (cinemáticos) de cada membro variam com a velocidade e o tamanho do ratinho. Nos ratinhos mutantes *pcd* e *reelers* descobriu-se que as suas perturbações motoras eram específicas. Durante a locomoção os ratinhos apresentaram alterações na trajetória (y, z) dos membros e na coordenação motora das diferentes partes do corpo. Foram depois usadas Ferramentas de optogenética foram depois usadas para manipular com precisão os diferentes núcleos do cerebelo. A combinação desta manipulação genética com o LocoMouse permitiu-me identificar perturbações locomotoras especificas de cada núcleo. Manipulações nos núcleos fastigial e globosos levaram a alterações no movimento durante a locomoção dos ratinhos, enquanto que manipulações no núcleo denteado não levaram a qualquer perturbação no movimento. Os resultados aqui obtidos são consistentes com estudos anteriores que sugerem que o cerebelo apresenta uma organização funcional médio-lateral.

O uso de ratinhos com mutações no cerebelo, ratinhos com mutações na coluna vertebral e ratinhos com manipulações precisas no circuito cerebelar permitiram-me distinguir e identificar parâmetros locomotores específicos do cerebelo. Estas experiências foram fundamentais para se poder estabelecer um sistema quantitativo de coordenação motora em ratinhos (Machado, Darmohray et al. eLife 2015).

Palavras chaves: Coordenação motora, ataxia, cerebelo, quantificação motora

# Table of Contents

**Acknowledgements** IX

**Abstract** XI

**Resumo** XIII

**Table of Contents** XV

**Index of Figures** XIX

**Index of Tables** XXI

**List of Abbreviations** XXIII

**Chapter 1: General introduction** 1

1.1 Circuits involved in locomotion: An overview 3

1.2 Role of the cerebellum in motor coordination 5

1.2.1 Cerebellum circuit: Its inputs and outputs 6

1.2.2 Cerebellar function: Lesions of Cerebellar Nuclei 7

1.2.3 Mutant ataxic mice, as an animal model, to study cerebellum function 8

1.3 Assessing motor coordination: Motor behavioral tasks 9

1.4 Thesis outline and main goals 11

**Chapter 2: LocoMouse: A high throughput system to quantify locomotion in freely walking mice** 12

2.1 Introduction 15

2.2 Methods 16

2.3 Results 21

2.3.1 Custom built behavior apparatus 21

2.3.1.1 Hardware and data acquisition 22

2.3.1.2 Tracking whole body movement in 3D: Computer vision algorithm and machine learning 23

2.3.2 Wild-type data analysis: Individual limbs in wild-type mice vary consistently with walking speed and body-size 26

2.3.2.1 Using linear mixed effects models to predict basic stride parameters 26

2.4 Discussion 29

**Chapter 3: Quantifying specific impairments in cerebellar ataxic mice (*pcd* and *reeler* mice)** 31

3.1 Introduction 33

3.2 Methods 35

3.3 Results 37

3.3.1 Single limb: Differences in forward trajectories of the paw can be accounted for by walking speed and body size; impairments are restricted to off-axis movement 37

3.3.2 Interlimb: Front-hind coordination is specifically impaired, while left-right coordination is preserved 43

3.3.3 Whole-body: In *pcd* and *reeler* the side-to-side (y) tail movement can be predicted by a passive model 47

3.4 Discussion 48

**Chapter 4: Optogenetic manipulation of distinct deep cerebellar nuclei differentially effects coordinated locomotion in mice** 51

4.1 Introduction 53

4.2 Methods 55

4.3 Results 57

4.3.1 Targeting the deep cerebellar nuclei with spatial and temporal precision: from medial to lateral region 57

4.3.2 Only medial and interposed nucleus show perturbation in overground during optogenetic manipulation. Lateral nucleus shows no effects 58

4.3.2.1 Using LocoMouse system to quantify specifically motor impairments during deep cerebellar nuclei manipulation. Speed and stance onset by trial 59

4.3.2.2 Distinguishing and quantifying locomotor parameters that are specific to each deep cerebellar nucleus 59

4.5 Discussion 69

**Chapter 5: LocoMouse a sensitive tool to assess specific and detail motor function in spinal cord mutant mice** 71

5.1 Introduction 73

5.2 Methods 74

5.3 Results 77

5.3.1 Using LocoMouse to reveal specific motor impairments in spinal cord mutant mice 77

5.3.2 Kinematic parameters of a single limb: Stride length is impaired 77

5.3.3 3D paw trajectories: Side to side (y) and vertical (z) movement are perturbed during swing phase 79

5.3.4 Interlimb: Gait and support patterns are preserved during overground locomotion 81

5.3.5 Nose and tail oscillation across speed bins and tail segments: Impairments are restricted to tail segments 82

5.4 Discussion 86

**Chapter 6: Conclusions** 89

**References** 97

# Index of Figures

**Figure 1.1.** Circuits involved in Locomotion. 4

**Figure 1.2.** Cerebellum circuit: From medial to lateral. Its inputs and outputs. 7

**Figure 2.1.** LocoMouse system for analyzing mouse locomotor coordination. 22

**Figure 2.2.** Front panel and flowchart of the data acquisition software. 23

**Figure 2.3.** Computer vision algorithms and machine learning techniques to track whole-body movements. 24

**Figure 2.4.** Trajectories of whole-body in 3D. 25

**Figure 2.5.** LocoMouse tracking validation. 26

**Figure 2.6**. Basic stride parameters can be predicted using only walking speed and body size. 27

**Figure 2.7.** Properties of wildtype mice used for linear mixed-effects model 28

**Figure 3.1.** Sagittal sections of the mouse brain to compare cerebellar morphology between wildtype, *pcd* and *reeler* mice. 34

**Figure 3.2.** Differences in forward paw trajectories in *pcd* can be accounted for by walking speed and body size. *Reeler* mice and littermate controls have similar body size. 38

**Figure 3.3**. Basic stride parameters for *pcd* are not different from their size-matched controls. *Reeler* mice and littermates control have comparable body size. 39

**Figure 3.4.** Basic stride parameters for hind right paw. Differences in swing duration. 40

**Figure 3.5.** 3D paw trajectories for wildtype controls. 41

**Figure 3.6.** Impairments are restricted to off-axis movement for *pcd* and *reeler* mice. 42

**Figure 3.7.** 3D paw trajectories for *pcd* and *reeler* mice. 43

**Figure 3.8.** Wildtype mice walked in a symmetrical trot pattern across speeds. 44

**Figure 3.9.** Front-hind limb coordination is specifically impaired in *pcd* and *reeler* mice. 45

**Figure 3.10.** *Pcd* and *reeler* mice spent more time with more paws on the ground. 46

**Figure 3.11.** Nose and tail movements across speed bins for controls, *pcd* and *reeler* mice. 47

**Figure 3.12.** Visualization of impaired whole-body coordination in *pcd* and *reeler* mice. 48

**Figure 4.1.** Using L7CreChR2YFP mice to target the deep cerebellar nuclei: from medial to lateral region 58

**Figure 4.2.** Optogenetic manipulation of medial and interposed nuclei reduce ongoing movement during overground locomotion 60

**Figure 4.3.** Basic stride parameters are severely impaired during optogenetic manipulation in medial nucleus. Interposed stimulation showed a mild perturbation. 61

**Figure 4.4.** All four paws are severely impaired during optogenetic manipulation in medial nucleus. Only the right side is affected in the Interposed A nucleus. 62

**Figure 4.5.** Optogenetic manipulation of medial and interposed A nuclei induce impairments in 3D paw trajectories. 63

**Figure 4.6.** Instantaneous peak velocity reveals specific differences across paws and nucleus, during photostimulation. 65

**Figure 4.7.** Interlimb coordination between stimulated strides and no stimulated trials. 66

**Figure 4.8**. Mice with medial and interposed A nucleus photostimulation spent more time with more paws on the ground. No significant differences were found in interlimb coordination. 67

**Figure 4.9.** Nose and tail movements across speed bins for medial, int A and lateral nuclei optogenetic manipulation. 68

**Figure 5.1.** Using the LocoMouse system to quantify specifically motor impairments in spinal cord mutant mice. 78

**Figure 5.2.** Stride length is impaired in *Dll4*f/f*Nestin-Cre* and *Dll1*f/+*Dll4*f/f*Nestin-Cre* mice. 79

**Figure 5.3.** Side to side (y) and vertical (z) movement are perturbed during swing phase for *Dll4*f/f*Nestin-Cre* and *Dll1*f/+*Dll4*f/f*Nestin-Cre* mice. 80

**Figure 5.4.** Gait and support patterns are preserved during overground locomotion. 82

**Figure 5.5.** Nose and tail oscillation across speed bins and tail segments. Impairments are restricted to tail movement in *Dll4*f/f*Nestin-Cre* and *Dll1*f/+*Dll4*f/f*Nestin-Cre* mice. 83

**Figure 5.6.** Impact of *Dll1* and/or *Dll4* deletion on the number of NeuN+ neurons and CHX10+ interneurons in the adult spinal cord. 85

# Index of Tables

**Table 2.1.** Image Feature Size 19

**Table 2.2.** Using linear mixed effects models to predict individual limb parameters 29

# List of Abbreviations

| | |
|---|---|
| 5-HT | 5-Hydroxytryptamine, Serotonin |
| AP | Anterior Posterior |
| ATP/GTP | Adenosine Triphosphate / Guanosine-Triphosphate |
| AVT | Allied Vision Technology |
| BSN | Brainstem Nuclei |
| BW | Black and White |
| C57BL/6 | C57 Black 6 |
| ChR2 | Channelrhodopsin-2 |
| CHX10 | Ceh-10 homeodomain containing homolog (*C.elegans*) |
| CPG | Central Pattern Generator |
| CV | Coefficients of Variation |
| DAPI | 4',6-diamidino-2-phenylindole |
| DCN | Deep Cerebellar Nuclei |
| *Dll1/4* | Delta ligands 1/4 |
| DRN | Dorsal Raphe Nucleus |
| EMG | Electromyography |
| FL | Front Left paw |
| FR | Front Right paw |
| HL | Hind Left paw |
| HR | Hind Right paw |
| INS | Interneurons |
| IP | Intraperitoneal |
| IR | Infra Red |
| ML | Medial Lateral |
| MLR | Mesencephalic Locomotor Region |
| NA | Numerical Aperture |
| NMS | Non-Maximum Suppression |
| PBS | Phosphate Buffered Saline |
| PCD | Purkinje Cell Degeneration |
| PCR | Polymerase Chain Reaction |
| PKJ | Purkinje |
| RF | Reticular Formation |
| RT | Room Temperature |
| SVM | Support Vector Machine |
| TTL | Transistor-Transistor Logic |
| YFP | Yellow Fluorescent Protein |
| LED | Light Emitting Diode |
| WT | Wild Type |
| LIBSVM | Library Support Vector Machines |
| CCD | Charge-Coupled Device |

# 1

# General introduction

- **1.1 Circuits involved in locomotion: An overview**
- **1.2 Role of the cerebellum in motor coordination**
  - **1.2.1 Cerebellum circuit: Its inputs and outputs**
  - **1.2.2 Cerebellar function: Lesions of Cerebellar Nuclei**
  - **1.2.3 Mutant ataxic mice, as an animal model, to study cerebellum function**
- **1.3 Assessing motor coordination: Motor behavioral tasks**
- **1.4 Thesis outline and main goals**

## 1.1 Circuits involved in locomotion: An overview

Locomotion, by definition, is the ability to move from one place to another and to interact with the surroundings. It uses rhythmic and coordinated movements across different parts of the body (Grillner 1975, Orlovsky, Deliagina et al. 1999, Dickinson 2000, Kandel, Schwartz et al. 2000, Goulding 2009). One example is walking (which involves the repetition of step cycles). During walking, the arms, trunk and head movements are coordinated with leg movements in order to maintain a stable and smooth gait. Locomotion also requires continuous modification of stereotyped movements to adapt to new surroundings (Grillner 1975, Orlovsky, Deliagina et al. 1999, Mendes, Bartos et al. 2013, Kiehn 2016). Therefore, locomotion circuits in the brain need to generate rhythmic motor patterns and adjusting them to new environments.

Most of what is known on neural circuits of walking has come from studies in cats (Shik, Severin et al. 1966, Shik and Orlovsky 1976). However, other animals and other rhythmic behaviors such as swimming (in fish) and flying (in insects) have contributed to understanding of the neural circuits in locomotion (Dale and Kuenzi 1997, Marder and Bucher 2001, Grillner 2003, Kiehn 2006, Mendes, Bartos et al. 2013). Studies in decerebrate animals (where cerebral hemispheres were removed) showed that animals were still able to walk spontaneously, producing a rhythmic movement (Shik, Severin et al. 1966, Shik and Orlovsky 1976). Those and more recent studies have demonstrated that the rhythmic motor pattern comprises a distributed network of interneurons and motor neurons located in the spinal cord. These networks are called central pattern generators (CPGs), which upon appropriate stimulation generate an organized motor rhythm that replicates the patterns of motor activity seen during repetitive locomotor tasks such as walking and swimming. (Brown 1911, Wilson and Wyman 1965, Grillner 1975, Grillner and Jessell 2009, Arber 2012.)

Motoneurons in the spinal cord are located topographically according to function (Crosby 1962). Medial motoneurons project to axial muscles of the trunk and proximal limb muscles. They play a fundamental role in maintaining posture and equilibrium during ongoing movements (Kasper, Schor et al. 1988). Lateral motoneurons serve the distal limb musculature and they are concerned with complex and fine limb movement (Lawrence and Kuypers 1968). Descending projections onto motoneurons rise from brainstem and/or cerebral cortex. Brown’s studies also revealed several important insights regarding locomotion circuits. The initiation and modulation of central pattern generators are performed by signals descending from brain (Armstrong 1986, Jordan 1998, Drew, Prentice et al. 2004, Rossignol, Dubuc et al. 2005, Kiehn 2016). Moreover, the proprioceptors also played an important role in modulating the activity of the spinal neuronal circuits (Pearson 2004).

In order to interact with surroundings, a more complex movement is required. The rhythmic motor patterns must be continuously adjusted. For this fine motor control, many regions of the brain and brainstem are involved (Armstrong 1986, Jordan 1998, Drew, Prentice et al. 2004, Rossignol, Dubuc et al. 2005, Kiehn 2016). Each region plays a different role in regulating locomotion. Motor cortex has a role in planning and refining motor action. It uses visual cues from visuomotor cortex to correct locomotion (Drew and Marigold 2015). The initiation and speed of locomotion seems to be mediated by the neurons in the mesencephalic locomotor region (MLR), which has inputs from the basal ganglia and thalamus (Dubuc 2008, Jordan, Liu et al. 2008). MLR neurons then projects to reticular formation (RF) located in the brain stem. Neurons from RF projects onto motoneurons in spinal cord and carry the information to execute locomotion (Pearson 2004, Dubuc 2008, Jordan, Liu et al. 2008). Vestibular and rubrospinal pathways (brainstem nuclei (BSN)) convey modulatory signals to maintain posture and to regulate ongoing movement. Proprioceptive signals through afferent inputs also regulates the spinal motor centers (Pearson 2004).

Finally, the cerebellum is critical for coordinated movement (Morton and Bastian 2007). It receives proprioceptive and somatosensory information from the periphery and information from a wide area of cerebellar cortex (Mauk and Thach 2008, Lisberger and Thach 2013). Cerebellum modulates the motor patterns and mediates sensory and internal feedback (**Figure 1.1**) (Ito 1972, Lisberger and Thach 2013).

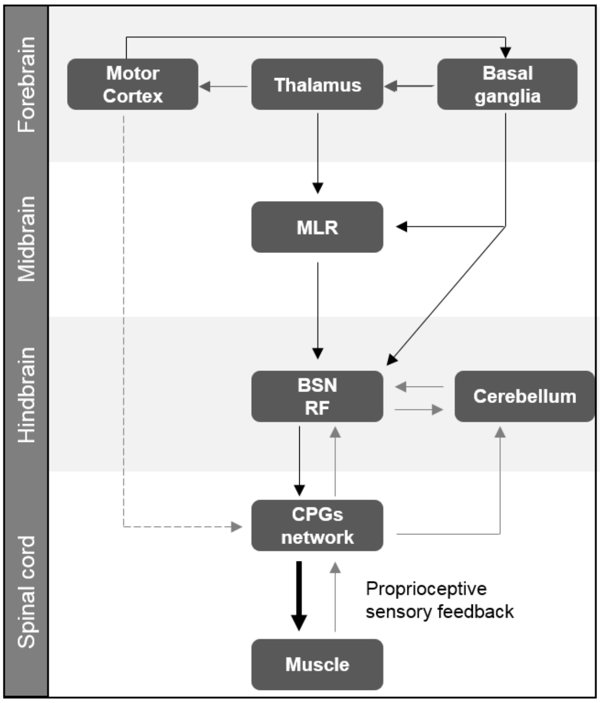

**Figure 1.1. Circuits involved in Locomotion.**

Schematic representation of the neuronal structures and respective pathways involved in simple rhythmic behaviors such as locomotion. The supraspinal areas (Hind Mid and Forebrain) are involved in the initiation, planning and modulation of locomotion. In the spinal cord, the CPGs are responsible for the rhythmic movement. Connections from the motor cortex refine and initiate motor actions (dotted arrow). The black arrows indicate direct command pathways, the grey arrows feedback pathways. MLR: mesencephalic locomotor region; BSN: brainstem nuclei; RF: reticular formation; CPGs: central pattern generators. (adapted from Gouding 2009).

Although it is clear that the cerebellum plays an important role during locomotion, the mechanisms of cerebellar contributions to gait coordination remain nuclear. The goal of this thesis is to develop tools to understand the role of the cerebellum in gait coordination.

## 1.2 Role of the cerebellum in motor coordination

One of the most characteristic and sensitive signs of cerebellar damage is gait ataxia (Palliyath, Hallett et al. 1998, Morton and Bastian 2007). This disorder is characterized, in general, by the occurrence of uncoordinated movements both in space (across the different body parts) and time. In particular, the gait of cerebellar lesion patients or animals is slow, with a widened base of support and erratic limb trajectory (Earhart and Bastian 2001, Stolze, Klebe et al. 2002). These features result in part from impairments in the coordination across multiple joints (Palliyath, Hallett et al. 1998, Earhart and Bastian 2001). However, people and animals that suffer from ataxia can express a variety of disparate symptoms (Morton and Bastian 2007, Cendelin 2014). It is not known how activity and dysfunction of individual neuronal types are related to the variety of ataxic symptoms.

In addition to its role in gait coordination, the cerebellum is also required for motor learning (Raymond, Lisberger et al. 1996). Simple forms of cerebellum-dependent learning, such as eye movements and eyelid conditioning, have been studied in mice (De Zeeuw and Yeo 2005, Lisberger 2009). The combination of these simple behaviors with genetic tools and careful quantification, has strengthened our understanding of how activity and plasticity in identified neural populations contributes to motor learning (De Zeeuw, Hansel et al. 1998, Nguyen-Vu, Kimpo et al. 2013). In contrast, a similar dissection of the cerebellar circuit in a more complex behavior, such as gait, has not been performed (Morton and Bastian 2006). For decades, people have assumed that understanding the cerebellar mechanisms underlying these simple behaviors would enlighten our knowledge in more complex behavior (Ito 1972, Lisberger 1988). However, the precise role of the cerebellum in coordinating gait is still not well understood (Morton and Bastian 2007).

To understand how coordination is controlled we first need to quantify it. Therefore, during this project we built a novel behavior paradigm to specifically quantify motor coordination (**Chapter 2**). We then combined it with genetic tools to dissect the cerebellar circuit and identify cerebellum-dependent locomotor parameters (**Chapter 3** - **5**).

### 1.2.1 Cerebellum circuit: Its inputs and outputs

The cerebellar circuit is one of the simplest and well known circuits in the brain. It has a basic microcircuit that is repeated across the medial to lateral regions (**Figure 1.2 A**) (Purves, Augustine et al. , Mauk and Thach 2008, Lisberger and Thach 2013) . The cerebellar cortex is subdivided into three distinct layers: granule cell layer, Purkinje cell layer and molecular layer. The granule cell layer is packed with granule cells. Granule cells send axons to the molecular layer to form parallel fibers. Golgi cells are also present in this layer. The Purkinje cell layer is occupied by Purkinje cell bodies, whose axons are the sole output of cerebellar cortex. Purkinje cell dendrites extend into the molecular layer and are oriented at right angles to the parallel fibers. They make synaptic contacts with parallel fibers and each dendrite can receive inputs from more than 200,000 parallel fibers. Each parallel fiber contacts several Purkinje cell dendrites that are extended along the folium. They may span to several joints in a somatotopic region. This arrangement could provide a possible mechanism for motor coordination. In addition, parallel fibers can also extent and connect Purkinje cells projecting to adjacent deep nuclei, providing a possible mechanism for internuclear coordination. The molecular layer also contains stellate and basket cells that provide inhibitory inputs to Purkinje cells (Itō 1984, Thach, Goodkin et al. 1992).

The two major inputs of the cerebellum are the mossy fibers and climbing fibers. They have two major projections: One is directly connected to the deep cerebellar nuclei (DCN) and the other terminates in different cerebellar cortical layers (Eccles 2013). Mossy fibers excite the granule and Golgi cells and they arise in the spinal cord and brainstem nuclei. Climbing fibers ascend in the inferior olive and excite directly Purkinje cell dendrites. The output of the cerebellar cortex is delivered by inhibitory Purkinje cells to DCN (**Figure 1.2 A in black**).

Purkinje cells in cerebellar cortex project to three main deep cerebellar nuclei: medial (fastigial), interposed and lateral (dentate) nuclei (Jansen and Brodal 1940, Voogd and Glickstein 1998). They are located in three distinct longitudinal regions: medial, intermediate and lateral region. These regions receive information from different inputs and project to different brain areas (Jansen and Brodal 1940, Voogd and Glickstein 1998). Purkinje cells axons are orderly organized. In the medial zone, Purkinje cells project to medial nucleus and receive mossy fibers inputs from vestibular afferents, reticular pontine nuclei, and the ventral and dorsal spinocerebellar tracts (Clendenin, Ekerot et al. 1974, Kotchabhakdi and Walberg 1978). The medial nucleus, then projects to ipsilateral vestibular and reticular nuclei. A small number of projections also goes to motor cortex via thalamus (Asanuma, Thach et al. 1983, Asanuma, Thach et al. 1983). The intermediate zone receives mossy fiber input from the

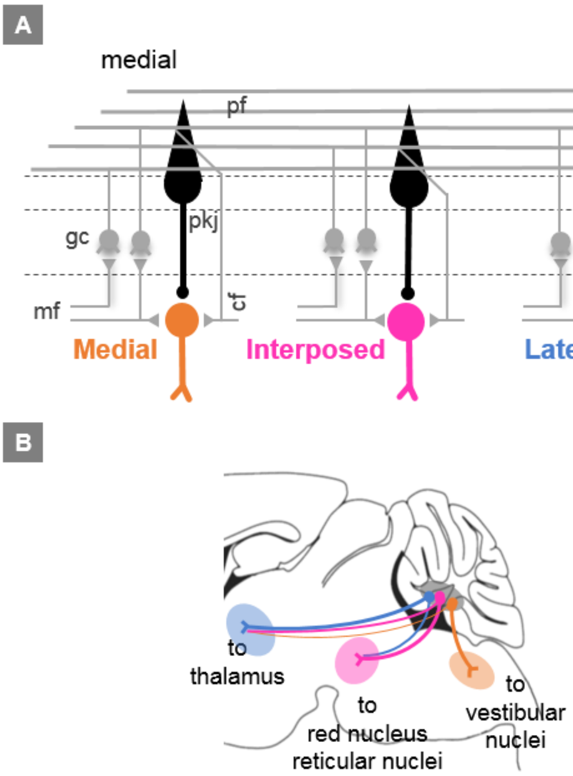
A
medial
lateral
pf
Molecular layer
Pkj cell layer
pkj
gc
Granule cell layer
Deep cerebellar nuceli
mf
cf
Medial
Interposed
Lateral
B
to thalamus
to red nucleus
reticular nuclei
to vestibular nuclei

**Figure 1.2. Cerebellum circuit: From medial to lateral. Its inputs and outputs.**

**(A)** Medial to lateral inputs and outputs of the cerebellum. Purkinje cells output of the cerebellum circuit (black). The cerebellum circuit is repeated across medial to lateral region and it's composed by mf: mossy fibers; gc: granule cells; pf: parallel fibers; pkj: purkinje cells; cf: climbing fibers. **(B)** Schematic illustration of deep cerebellar nuclei projections

spinocerebellar tracts, reticular nuclei, and cerebral cortical areas (Matsushita, Okado et al. 1981). Purkinje cells, in this region, connect to interposed nucleus. Outputs from the interposed nucleus projects to red nucleus and a small subset goes to motor cortex via thalamus (Asanuma, Thach et al. 1983). Finally, most outputs from the lateral nucleus are projected to cerebral cortex (mainly motor, somatosensory, and posterior parietal areas) via thalamus (Asanuma, Thach et al. 1983). A small number of projections onto red nucleus is also observed. Lateral nucleus receives inputs from Purkinje cells located in the most lateral region of the cerebellum (**Figure 1.2** B).

This mediolateral organization of the deep cerebellar nuclei is reflected in their projections to the medial and lateral descending motor pathways. Both interposed and lateral nuclei project to the lateral motor system, while medial nucleus projects to the medial motor system. In summary, the regular arrangement of cells and parallel fibers in the cerebellar cortex suggest a mechanism to modulate and coordinate movement (Morton and Bastian 2007).

### 1.2.2 Cerebellar function: Lesions of Cerebellar Nuclei

Most of what we know about cerebellar function has been largely driven by the studies on lesions together with physiology and anatomy. Lesion studies of the deep cerebellar nuclei, in cats and monkeys, provided important information about the cerebellum's functional organization (Morton and Bastian 2007, Mauk and Thach 2008). A medial to lateral functional organization was observed where the different outputs are responsible for different aspects of motor control (Chambers and Sprague 1955),.

Lesions in the medial nucleus resulted in dramatic impairments during locomotion. A low posture and a lack of balance was observed. An unsupported gait and wrong foot placement was also visible (Sprague and Chambers 1953, Chambers and Sprague 1955). Motor impairments caused by lesions in the interposed nucleus were more restricted to the limbs. Erratic limb trajectory during walking, altered paw placements and limb tremor were detected (Chambers and Sprague 1955, Udo, Matsukawa et al. 1979, Udo, Matsukawa et al. 1980, Yu and Eidelberg 1983). No Motor impairments were observed when the lateral nucleus was lesioned, particularly during overground locomotion. However, when the behavioral task required the execution of highly complex movements with visual cue and initiation of planned movements, impairments were noticed (Chambers and Sprague 1955, Thach, Goodkin et al. 1992, Marple-Horvat, Criado et al. 1998).

In summary, lesions in the different deep cerebellar nuclei suggest that posture and balance control are mediated by the medial nucleus, while the interposed nucleus is more concerned with fine tuning of limb movements, particularly in keeping oscillations under control. Finally, the organization and execution of planned movements are mediated by lateral nucleus (Morton and Bastian 2007).

Although lesion studies provide useful information on medial-to-lateral functional organization, they are often poorly spatial defined. Therefore, they lack specificity and compensatory mechanisms are unavoidable. In **chapter 5** I will combine the LocoMouse system with optogenetics (acute and precise manipulation) to ask how different output regions of the cerebellum differentially contribute to locomotor coordination.

### 1.2.3 Mutant ataxic mice, as an animal model, to study cerebellum

Besides the lesion studies, several mouse models have been developed to mimic symptoms of human cerebellar disease (Manto and Marmolino 2009). A variety of cerebellar degenerative mouse models exists and they are either spontaneous mutants or transgenic animals (Lalonde and Strazielle 2007, Cendelin 2014). The cerebellum projects to a huge variety of areas in the central nervous system. Therefore, the majority of neuronal degeneration in these mouse models are not restricted to the cerebellum (Cendelin 2014). Thus, it is extremely important to know the features of each cerebellar ataxic mouse and compare them to each other in order to have the most appropriate conclusions (Cendelin 2014). A list of cerebellar ataxic mouse can be used. In this project, I used the classic cerebellar mutant mice Purkinje cell degeneration mice (pcd) and reeler mice to specifically quantify the role of cerebellum in motor coordination (**chapter 3**).

The Purkinje (Pkj) cell degeneration (pcd) mouse is a recessive mutant characterized by complete post-natal degeneration of cerebellar Purkinje cells and subsequent partial loss of cerebellar granule cells (Chen, Bao et al. 1996, Le Marec and Lalonde 1997, Lalonde and Strazielle 2007, Cendelin 2014). The gene affected encodes ATP/GTP binding protein 1 (Fernandez-Gonzalez, La Spada et al. 2002). Pcd mice can be easily identified by eye based on their ataxic, uncoordinated movements (Mullen, Eicher et al. 1976, Le Marec and Lalonde 1997). Reeler mice have an autosomal recessive mutation (Relnrl). This gene is involved in neural cell migration (Beckers, Bar et al. 1994). Thus, the lack of it in the mutant mice can cause several defects, abnormal localization of neurons and failure of neuronal layer formation (Beckers, Bar et al. 1994). Several brain regions, including the cerebellum are affected (Hamburgh 1963, Terashima, Inoue et al. 1983). Homozygous reeler mice are characterized by an ataxic and reeling gait, with difficulties in maintaining their hindquarters upright (Cendelin 2014).

These mouse lines have been identified based on their visible gait ataxia, or uncoordinated walking (Mullen, Eicher et al. 1976, Walter, Alvina et al. 2006, Lalonde and Strazielle 2007, Cendelin 2014). As was previous described, they exhibit abnormal cell patterning within the cerebellum, with different spatiotemporal patterns of neural degeneration (Lalonde and Strazielle 2007, Brooks and Dunnett 2009, Sheets, Lai et al. 2013, Cendelin 2014). Thus, understanding the relationship between circuit dysfunction and motor impairment could provide clues about the cerebellum neural circuit mechanisms into motor coordination.

Although lesion studies and cerebellar ataxic mice provide us useful insights about the cerebellum function and organization, several questions remain. What are the contribution of each cell type in the cerebellum circuit to locomotion activity? How and where cerebellum integrates the information of different body parts to produce a smooth and coordinated movement? Which gait parameters are controlled by the cerebellum during locomotion?

## 1.3 Assessing motor coordination: Motor behavioral tasks

Tools to manipulate the activity of selective neural subtypes have been growing tremendously (Luo, Callaway et al. 2008). The emerging field of optogenetics offers exciting neuroengineering tools that combine genetics and optical methods to selectively stimulate or silence neural subtypes with a high temporal precision and reversibility (Zhang, Aravanis et al. 2007). However, behavior quantification has not grown at the same pace (Anderson and Perona 2014). There is a general lack of precise quantification and detailed information in the study of mouse locomotor behavior (Kale, Amende et al. 2004, Brooks and Dunnett 2009), in particular, motor parameters that are cerebellum dependent.

During locomotion, the motor pattern of the stepping limb can be described through kinetics (forces), kinematics (movements) and EMG activity (Orlovsky, Deliagina et al. 1999). This project focus on kinematic parameters. The step cycle during walk consists in two distinct phases: stance (or support) phase and swing (or transfer) phase. In swing phase, the limb is lifted above the round and moves forward in relation to the body, while in stance phase the limb remains on the ground and the body moves forward (Orlovsky, Deliagina et al. 1999). During the step cycle all the joint of the limb perform flexion-extension movements. These joints movements must be preserved and coordinated over the whole range of locomotor speeds. Coordination across limbs (interlimb coordination) is also crucial to maintain a stable and smooth movement. During locomotion and in vertebrates there is a highly stereotyped pattern of limb movements, with a defined phase relationship between limbs. Walking, trotting and galloping are examples of the different gait patterns and they are speed dependent (Gorska, Zmysłowski et al. 1998, Orlovsky, Deliagina et al. 1999).

Currently, the most common tests for assessing mouse motor phenotypes rely on global and indirect measures of coordination and are limited in their quantification of specific aspects of gait impairment (Brooks and Dunnett 2009). These parameters are time to fall from a rotarod (Walter, Alvina et al. 2006, Lalonde and Strazielle 2007), the time taken to cross a fixed bar (Kim, Cook et al. 2009, Cendelin 2014), or stride length through paw print analysis (Wang, Parris et al. 2006, Lalonde and Strazielle 2007). Analyses of mouse gait have typically lacked quantification of whole-body movements (across space and time), in an automated way, with high spatial and temporal resolution (Brooks and Dunnett 2009, Mendes, Bartos et al. 2015). Even the most recent systems that use overground locomotion and motorized treadmill to quantify gait have tended to either emphasize throughput (Hamers, Lankhorst et al. 2001) or the collection of more detailed trajectories of a particular limb (Leblond, L'Espérance et al. 2003, Kale, Amende et al. 2004, Garnier, Falempin et al. 2008, Zörner, Filli et al. 2010).

Because the architecture of the cerebellum is conserved across vertebrates, improved understanding of the mechanisms of gait coordination in mice would be helpful for identifying therapeutic targets in cerebellar patients (Morton and Bastian 2007). Moreover, the ability to specifically manipulate activity within individual cell types in the cerebellum, if combined with appropriate behavioral analysis, could make mouse locomotion a powerful system in which to establish relationships between activity in individual cell types and particular aspects of behavior.

## 1.4 Thesis outline and main goals

The cerebellum plays an important role in gait coordination. However, how this is controlled by neurons within the cerebellar circuit is still not well understood. The aim of my PhD project is to investigate the consequences of specific perturbations of cerebellar function in order to understand how the cerebellar circuit work as a unit to coordinate movement. This thesis had three main aims: **(I)** building a novel behavioral paradigm that uses high-speed videography to track whole-body mouse locomotion (Machado et al., 2015); **(II)** establishing a quantitative frame work to identify cerebellum-dependent gait parameters, by using cerebellar ataxic mice (Machado et al., 2015); **(III)** Using genetic tools to manipulate the deep cerebellar nuclei in order to understand a medial-to-lateral functional organization of cerebellar outputs (manuscript in preparation).

In **Chapter 2** I described the LocoMouse system. The custom built apparatus: hardware and software tracking. The implementation of linear mixed effects models to describe and predict basic stride parameters of wild type mice.

In **Chapter 3** I used the LocoMouse system to establish a quantitative framework for whole-body coordination. Specific deficits in freely walking ataxic mice (*pcd* and *reeler* mice) were revealed.

In **Chapter 4** I describe a medial to lateral functional organization of the Cerebellum output, by using optogenetic tools to precisely manipulate the deep cerebellar nuclei.

In **Chapter 5** I showed that the quantitative framework provided by the LocoMouse system can differentiate and identify specific locomotor parameters that are associated to other locomotion circuits. Spinal cord mutant mice were used.

Finally, in **Chapter 6** I will discuss the implications of our approach and experimental findings.

# 2

# LocoMouse: A high throughput system to quantify locomotion in freely walking mice

- **2.1. Introduction**
- **2.2. Methods**
- **2.3. Results**
    - **2.3.1. Custom built behavior apparatus**
        - 2.3.1.1. Hardware and data acquisition
        - 2.3.1.2. Tracking whole body movement in 3D: Computer vision algorithm and machine learning
    - **2.3.2. Wild-type data analysis: Individual limbs in wild-type mice vary consistently with walking speed and body-size**
        - 2.3.2.1. Using linear mixed effects models to predict basic stride parameters
- **2.4. Discussion**

**Results published:**

Ana S. Machado, Dana M. Darmohray, João Fayad, Hugo G. Marques, Megan R. Carey, A quantitative framework for whole-body coordination reveals specific deficits in freely walking ataxic mice. **eLife** (2015) DOI**:** http://dx.doi.org/10.7554/eLife.07892

Author contributions:

ASM, Conception and design of setup. Developed acquisition software. Developed first version of tracking system. Data acquisition. Applied linear mixed effects model in WT mice. JF, Developed current tracking algorithm with machine learning techniques. MRC wrote the manuscript. ASM, DMD and MRC Analysis and interpretation of data.

## 2.1 Introduction

Mice provide a unique opportunity for understanding the neural control of whole-body coordination. In addition to their amenability to genetic circuit dissection, their small size makes it possible to analyze even unrestrained, relatively complex whole-body actions within a laboratory setting.

Because of the significant challenges associated with quantifying whole-body coordination in freely walking animals, assessments of mouse motor coordination phenotypes often rely on indirect measures (Mullen, Eicher et al. 1976, Lalonde and Strazielle 2007, Brooks and Dunnett 2009, Sheets, Lai et al. 2013), such as time to fall from a rotarod (Walter, Alvina et al. 2006, Lalonde and Strazielle 2007) or a fixed bar (Kim, Cook et al. 2009, Cendelin 2014). While these can be sensitive markers for global motor dysfunction, they lack specificity. Moreover, performance on coordination tasks, or even on a motorized treadmill, does not necessarily correspond to the degree of gait ataxia during overground locomotion (Herbin, Hackert et al. 2007, Guillot, Asress et al. 2008, Cendelín, Voller et al. 2010, Stroobants, Gantois et al. 2013, Suidan, Duerschmied et al. 2013, Camera, Boase et al. 2014). Meanwhile, gait analysis in freely walking mice typically focuses on parameters of individual limbs, such as stride length or duration. While ataxia is often associated with changes in these parameters, they are also not specific markers for ataxia and may simply reflect the slower walking speeds of ataxic mice (Cendelín, Voller et al. 2010, Batka, Brown et al. 2014). Thus, traditional measures have failed to quantify the key features of gait ataxia in mice.

This chapter describes LocoMouse, a high-throughput, automated, markerless system for tracking and analyzing 3D, whole-body coordination in freely walking mice.

## 2.2 Methods

### Animals

All procedures were reviewed and performed in accordance with the Champalimaud Centre for the Unknown Ethics Committee guidelines, and approved by the Portuguese Direcção Geral de Veterinária (Ref. No. 0421/000/000/2015). C57BL/6 mice were housed in institutional standard cages (3 animals per cage) on a reversed 12-hr light/12-hr dark cycle with *ad libitum* access to water and food. Experiments were conducted with wildtype controls (n = 9602; N = 34 mice; 23 male; 11 female; 7-33g, 30–114 days old) (**Figure 2.7**).

### LocoMouse setup

A custom-designed setup was developed to assess whole body coordination during overground locomotion in mice (**Figure 2.1**). The LocoMouse apparatus consists of a clear glass corridor, 66.5 cm long, 4.5 cm wide and 20 cm high. Mice were filmed crossing the corridor with a high-resolution, high-speed camera (Bonito CL-400B, Allied Vision Technologies, https://www.alliedvision.com). A mirror (66 cm × 16 cm) was placed below the corridor at an angle of ∼45° to allow simultaneous collection of side and bottom views in order to generate three-dimensional tracking data. Lighting consisted of a matrix of LEDs that emitted cool white light positioned to maximize contrast and reduce reflection. Infrared sensors positioned along the runway automatically triggered the camera and acquisition software once the mouse entered the corridor and stopped the acquisition once the mouse reached the other end of the corridor or after 25 s.

### Data collection

Mice were handled by the experimenter and allowed to acclimate in the LocoMouse setup for several minutes on multiple occasions before data collection. Animals were weighed before each session. Mice walked freely between two dark boxes on either end of the glass corridor. The automatic triggering system was critical for allowing mice to self-initiate trials, which reduced animal stress without compromising the quantity of data collected. No food or water restriction or reward was used.

10-15 corridor passages (trials) were collected in each of five daily sessions. A total of 36,369 strides were collected from wildtype controls, which corresponds to 1069 ± 266 strides per mouse and 267 ± 66 strides per paw. Animals were not required to walk continuously throughout a trial; if the animal stopped mid-trial, the data before and after the halt were still analyzed.

### Data acquisition

Movies were collected at 400 frames per second with a spatial resolution of 1440x250 pixels. Acquisition software was written in Labview and uses 2 National Instruments boards (PCIe 1433 and BNC 2120) to record and save the movies, in real time. The tracking algorithm and data analysis software were written in Matlab (Mathworks) and performed offline. The LocoMouse Tracker code used in this paper can be downloaded from GitHub (https://github.com/careylab/LocoMouse).

### Tracking algorithm

### Overview

To maximize throughput, we used a computer vision algorithm to allow automatic, markerless tracking of features of interest (without the need for surface markers or manual initialization of feature tracks) (**Figure 2.3**). The algorithm's output was the set of 3D coordinates of the features of interest, which were: the center of each of the four paws, the snout, and the tail divided into 15 points, for each frame of the movies. The output of the tracking system was visually inspected for each trial. Further validation of the automated tracking performance is shown in **Figure 2.5**.

We used hand labeled data to train linear Support Vector Machine (SVM) classifiers for each feature and each view (side and bottom) independently. Positive examples were hand labeled on a set of 81 images from a single training video while 10 negative examples for each feature were randomly picked from the same images. Training the 6 SVM classifiers took approximately 1 hr on a machine with an Intel Core i7-3770 CPU and 16 GB or RAM. All experiments were performed with these SVM classifiers with no need to retrain on additional data. For each trial, the candidate locations for each feature were obtained by filtering the input images with the trained detectors. For the paws and snout, the resulting image regions were clustered into a small number of point locations using a standard non-maxima suppression algorithm. Once the candidate features were identified by the SVM, we considered the temporal trajectories and selected the candidate tracks that maximized per image detection scores while minimizing frame-by-frame displacement with a method based on existing multi-target tracking frameworks (Russell, de Agapito et al. 2011) that formulate tracking as the maximum a posteriori probability estimation over a Bayesian network of candidate locations on each image. Best bottom view tracks (x and y) were computed first and then the best side view track (z, accounting for image distortion from the optics) that matched the bottom view track was selected. For the tail, the interest regions were matched across views and the largest resulting 3D region was picked as the final detection. The tail was detected independently for every image. Following computation of feature tracks, pixel values were converted to millimeters for further analysis.

### Detailed description

The LocoMouse Tracker code developed and used in this paper has been deposited at GitHub (https://github.com/careylab/LocoMouse) and updated versions are available through our website. The LocoMouse tracker was developed in MATLAB R2013b (The MathWorks). Some auxiliary packages can be found at the Matlab Central File Exchange (http://www.mathworks.com/matlabcentral/fileexchange/). The method also relies on the LIBSVM library (http://www.csie.ntu.edu.tw/~cjlin/libsvm/) for Support Vector Machines and the code from (Russell, de Agapito et al. 2011) for Multi-target tracking.

### Removing background and correcting camera/mirror distortion

An image of the corridor was recorded before every session. To remove the background, we subtracted this image from every frame recorded by the system. To correct for image distortion, we recorded a video of a white spherical object moving along the full volume of the glass corridor. The two projections of the object were detected by thresholding the (gray-scale) image at 80% (after removing the background). The horizontal line splitting the image into the bottom and side views was defined manually at this point. The corrective image transformation makes the bottom and side projections of the object match along the vertical line and was computed via least squares. The corrective transformation depends on the position of the camera relative to the setup and was performed once for every configuration. Unless stated otherwise, all steps of the algorithm are performed on corrected images.

### Computing bounding box around mouse

We further isolated the mouse by computing a tight bounding box around it. We started by thresholding every input image at 10% and using a median filter to remove noise. For every image, the edges of the box are defined as the first and last rows and columns to have white pixels. To account for occlusions and noise, the final size of the bounding box was defined as the smaller of the mean size plus three standard deviations, and the maximum observed size. The final trajectory of the bounding box over the video was determined by filtering the box position calculated for each image with a moving average filter of width 5. All further steps in detecting the interest features were performed within the bounding box.

### Training the detectors

Feature detectors for the paws, snout and tail were trained using the LIBSVM library. Positive examples were manually annotated on a set of 81 training images from a single movie. The size of the detectors was chosen manually such that the feature lied within the detector box. Each view was treated independently, unless otherwise stated. The sizes of the different feature detectors can be found in **Table 1.**

**Table 1**: Image Feature Size

| Feature | Bottom view size (in pixels) | Side view size (in pixels) |
|---|---|---|
| Paw | 30 x 30 | 20 x 30 |
| Snout | 40 x 40 | 20 x 40 |
| Tail segments | 30 x 30 | 25 x 30 |

The system assumes mice move from left to right. Images were flipped horizontally when otherwise. For every feature, 10 negative examples were randomly extracted from within the bounding box of the mice for each of the 81 training images (excluding the positively labelled regions).

### Detecting paw and snout candidates

The outputs of LIBSVM were used to filter the pre-processed input images. These filters provided a score representing the likelihood of a pixel being part of each feature (paw or snout). These per-pixel scores were reduced into a small number of candidate locations with a standard Non-Maximum Suppression (NMS) algorithm (http://vision.ucsd.edu/~pdollar/toolbox/doc/) which clusters positively classified pixels into local maxima. Since on the side view there is considerable overlap between the features, we used a more conservative version of the NMS algorithm, which results in more candidate locations.

### Combining bottom and side view candidates

The 2D candidate locations from each view were combined into 3D candidates by matching their coordinates on the shared axis (horizontal axis). As exact matches do not occur, we used a tolerance of 30% of the feature's detector size along the horizontal axis for matching.

We allowed each bottom view candidate to be matched to many side view candidates, but each side view candidate was only (generally) matched to a single bottom view candidate. In ambiguous configurations, additional information about the velocity of the candidates was used to find the best match. Candidates were classified as moving/not moving according to the pixel count within the feature box size after subtracting the previous input image to the current image. When candidates could not be disambiguated, both options were allowed to remain.

## Computing feature tracks

We used location priors to distinguish between instances of the same class (e.g., to identify which paw was which). Based on the configuration of the corridor, the priors were defined as the inverse of the distance to the closest corner (i.e.on the bottom view, the front right paw is closer to the bottom right corner while the hind left paw is closer to the top left corner). The prior was defined on a normalized box which allows it to be fit to a bounding box of any size. Locations on the normalized box with a distance greater than 0.6 had their prior score set to zero.

## Multi-target tracking

After processing the candidate locations at each image, tracking on the bottom view was performed using the multi-target tracking algorithm of (Russell et al., 2011). This algorithm finds the tracks over all the images which maximizes the per image detection score (weighted by the location prior) while minimizing the in-between image distance. In practice the inverse distance was considered and the problem is formulated as:

$$\max_{\boldsymbol{x} \in L^{N.F}} C(\boldsymbol{x}) = \sum_{o=1}^{N} \left[ \sum_{t=1}^{F} U(x_{o,t}) + \alpha \sum_{t=1}^{F-1} P(x_{o,t}, x_{o,t+1}) \right],$$

where $\boldsymbol{x}$ is a possible (multi-target) track, $L$ is the number of possible locations, $N$ is the number of objects to track, $F$ the number of images in the video, $x_{o,t}$ a candidate location for object $o$ at time $t$,$U(.)$ the image detection score weighted by the location prior, $P(. , .)$ the inverse of the image distance between two points, and α the relative weight between image detection scores and image transitions (set empirically to 0.1). In practice we discarded all transitions that exceeded v pixels between two images, where v is the sum of the (variable) displacement of the bounding box and a fixed value of 15 pixels. An additional constraint was added such that only one object could occupy the same candidate location at the same instance in time.

For the side view, we used the same approach to find the most likely Z trajectory given the already computed X and Y tracks.

## Data analysis

The stride cycles of individual paws were automatically broken down into swing and stance phases based on the first derivative of the paw position trajectories. Individual strides were defined from stance onset to subsequent stance onset. For each stride, average *walking speed* was calculated by dividing the forward motion of the body center during that stride by the stride duration. All data was sorted into speed bins (0.05 m/s bin width) in a stridewise manner, with a minimum stride count criterion of 5 strides per bin, per animal. Individual limb movements and interlimb coordination were calculated as follows:

**Table 2**: **Individual limb parameters**

| **Limb parameters** | **Definitions** |
|---|---|
| Cadence | Inverse of stride duration |
| Swing velocity | Displacement of single limb during swing phase divided by swing duration |
| Stride length | Displacement from touchdown to touchdown of single limb |
| Stance duration | Time in milliseconds that foot is on the ground during stride |

**Modeling stride parameters across control mice**

We used linear mixed effects models (Bates, Maechler et al. 2014) to analyze our data and quantify the relationship between fixed (speed, gender, weight, length, age) and random (subject) effects and values for each stride parameter.

To linearize data for inclusion in the model, we first plotted the values of each stride parameter vs walking speed and generated fits to the data. Different fitting curves (linear, quadratic, cubic, inverse, logarithmic, exponential, power) were tested and selected based on the distribution of residuals and $R^2$ values. The curves that provided the best fits to each parameter are given in **Table 2.1**.

After transforming the data according to these best fit curves, we next asked to what extent the fixed and random effects contributed to remaining variability in the values of each parameter. For the fixed terms, we tested different equations, using additive and interaction properties. Random terms took into consideration differences in both slopes and intercepts. The equations were selected based on the following criteria: $R^2$ values (marginal and conditional (Nakagawa and Schielzeth 2013), likelihood ratio tests (comparing goodness of fit across equations) and collinearity of effects (**Table 2.1 A**). Due to collinearity, in many cases body length (measured directly from the movies) and weight provided good fits to the data. We chose to use weight throughout because it provided a platform-independent metric for body size that should be more reproducible.

## 2.3 Results

### 2.3.1 Custom built behavior apparatus

The noninvasive, markerless LocoMouse system uses high speed cameras and machine learning algorithms to automatically detect and track the position of paws, nose, and tail in 3D with high (2.5 ms) temporal resolution. It’s composed by 3 main parts: the data acquisition system, the tracking algorithm and the data analysis.

#### 2.3.1.1 Hardware and data acquisition

Mice walked across a glass corridor, 66.5 cm long and 4.5 cm wide (**Figure 2.1**). A mirror was placed at 45 degrees under the mouse, so that a single high-speed camera (AVT Bonito BW color, 1440x250 pixels @400 frames per second,) recorded both bottom and side views. Individual trials consisted of single crossings of the corridor. Infrared (IR) sensors were placed along the corridor to detect mice movement. Mice freely initiated trials by walking back and forth between two dark 'home' boxes on each end of the corridor. Mice ran one session per day, during one week. Each session consisted in 10-15 trials. Data collection was performed through a developed acquisition software.

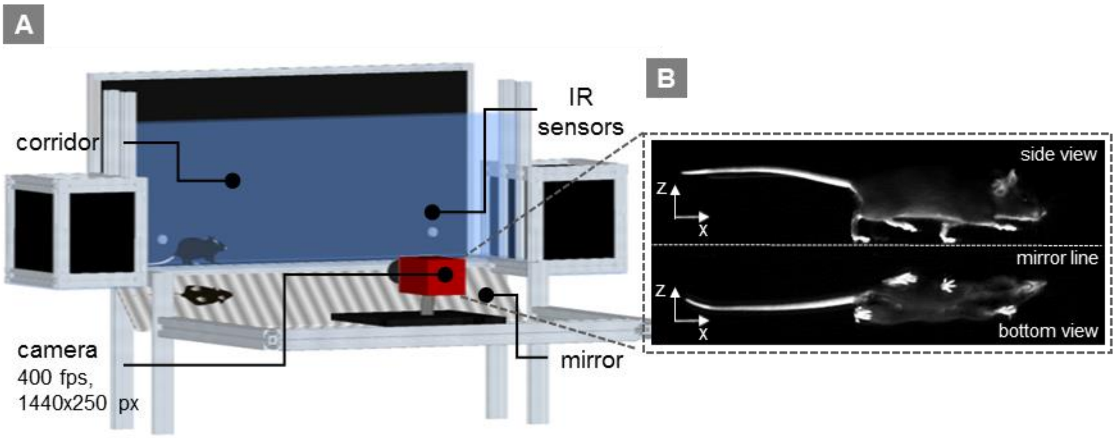

**Figure 2.1. LocoMouse system for analyzing mouse locomotor coordination.**

**(A)** LocoMouse apparatus. The mouse walks freely across a glass corridor with mirror below at a 45° angle. A high-speed camera captures at 400 fps. Infrared (IR) sensors trigger data collection. **(B)** An example of a single frame. Side and bottom (via mirror reflection) views of the mouse are captured in a single camera.

The acquisition software was written in LabVIEW and uses image (PCIe 1433) and digital acquisition (BNC 2120) boards, both from National Instruments. Before starting the acquisition software, mouse specific properties (mouse ID, weight, sex and age) where introduced in the control panel (**Figure 2.2A**). Then the experimenter placed the mouse inside the 'home' box. IR sensors were triggered when the mouse entered or exited the corridor, initiating automatically data collection. The acquisition software was based on a state machine design pattern, where distinguishable states exist and each state can lead to one or multiple states. In order to complete a trial, the software had to execute sequentially the following states: 1- collecting mouse specific parameters; 2- background image acquisition; 3- initialization trials by triggering IR; 4- video acquisition; 5-saving video. This sequence was repeated until the desire number of trials was reached (**Figure 2.2B**). With this design pattern, several states ran in parallel, which allowed to acquired videos, in real time, at a high speed-resolution minimizing the number of frame that were lost.

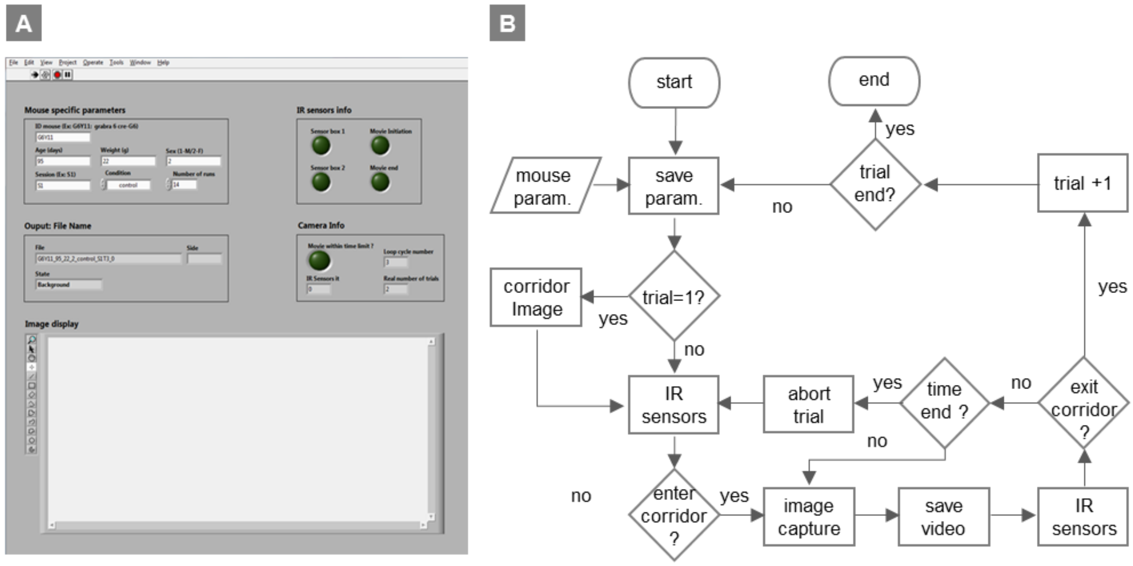

Mouse specific parameters
ID mouse (Ex: G6Y11: grabra 6 cre-G6): G6Y11
Age (days): 95
Weight (g): 22
Sex (1-M/2-F): 2
Session (Ex: S1): S1
Condition: control
Number of runs: 14

IR sensors info
Sensor box 1
Movie Initiation
Sensor box 2
Movie end

Ouput: File Name
File: G6Y11_95_22_2_control_S1T3_0
Side:
State: Background

Camera Info
Movie within time limit ?
Loop cycle number: 3
IR Sensors it: 0
Real number of trials: 2

Image display

**Figure 2.2. Front panel and flowchart of the data acquisition software.**

**(A)** Mouse specific parameters: mouse ID, age, weight, sex and number of trials are introduced in the front panel before starting the acquisition program. **(B)** Flowchart of the data acquisition software with the sequential steps. It has 5 main processes: saving parameters, capturing background image, reading IR sensors, capture and save video.

### 2.3.1.2 Tracking whole body movement in 3D: Computer vision algorithms and machine learning techniques

Besides the acquisition software, a tracking code was also developed in the Lab to maximize the throughput. I developed a first version of the tracking that used image processing and clustering techniques. It automatically tracked the different mouse body parts (without the need for surface markers or manual initialization of feature tracks). However, side view tracks weren't as robust as bottom view tracks due to paw occlusions. To solve this problem, a new version of the tracking software using machine learning was developed. The new tracking code was developed in MATLAB R2013b (The MathWorks) and can be downloaded from GitHub (https://github.com/careylab/LocoMouse). The data shown here were collected from the new tracking code.

Tracking, by definition, is the identification of the same object over time (**Figure. 2.3A**). The locoMouse tracker was based on computer vision algorithms and machine learning techniques. The first step was to subtract the background image in every single frame of the movie. The background image it's the corridor picture acquired before every session. Then, every image was corrected for lens and mirror distortions. Once the frames were cleaned and distorted, a Support Vector Machine (SVM) (**Figure. 2.3B**) was applied to identify several potential candidates for the different mouse body parts. Hand labeled data of each feature was used to train the Support Vector Machine (SVM) classifiers. After processing the candidates in each image, a multi-target tracking algorithm (Russell, de Agapito et al. 2011) was applied to select the final candidates. It's based on temporal information and the frame-by-frame displacement (**Figure 2.3**). For a more detail description of the different steps of the tracking code see Methods section.

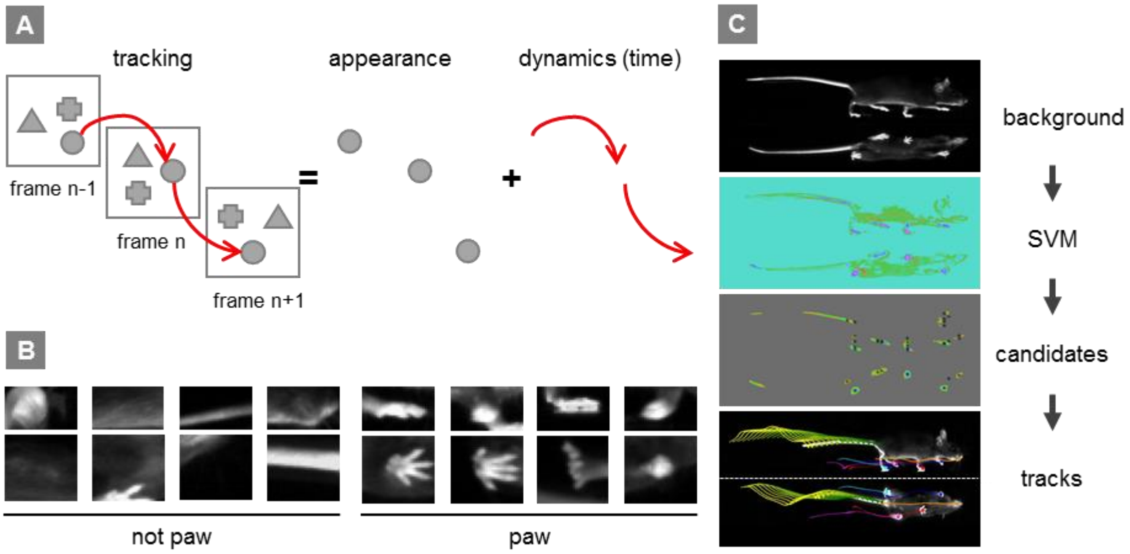

**Figure 2.3. Computer vision algorithms and machine learning techniques to track whole-body movements.**

**(A)** Schematic representation of the tracking definition. It's a combination of object recognition (appearance) with temporal information (dynamics). **(B)** Machine learning algorithms identify paws, nose, tail segments and track their movements in 3D. Example 'paw' and 'not paw' training images for SVM (Support Vector Machine) feature detectors are shown for side and bottom views. **(C)** Different steps of the software tracking. First a background subtraction is applied, then each frame is filtered with SVM detectors that will lead to propose candidates. Final, a multi-target tracking algorithm is used to select the final tracks.

The algorithm identifies and tracks all four paws, snout, and 15 tail segments in both bottom and side views for each trial. The left and right side of the mouse was also tracked depending on when the mouse crossed the corridor from left or right. As a final output the time, forward (x), side-to-side (y) and vertical (z) trajectory of each feature were collected for each trial (**Figure 2.4A, B**). Fewer than 10% of the trials were excluded due to tracking failure (typically due to exploration or grooming behavior that resulted in erroneous swing and stance detection).

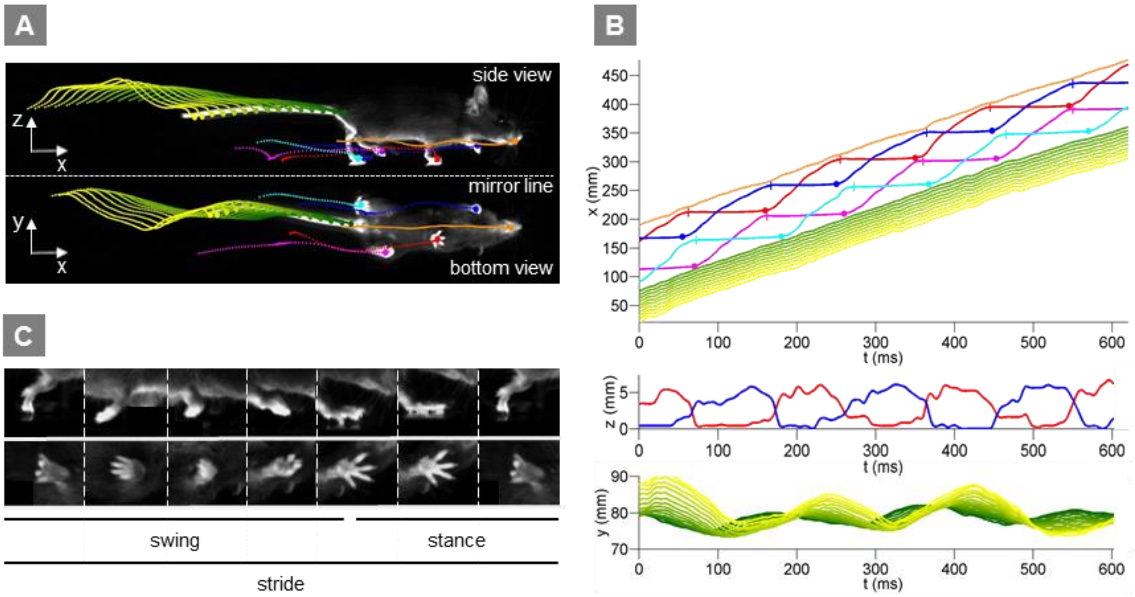

**Figure 2.4. Trajectories of whole-body in 3D.**

**(A)** Continuous tracks are obtained by post-processing the feature detections with a Multi-Target Tracking algorithm. **(B)** Top plot: Continuous forward trajectories (x position vs time) for paws, nose, and tail. The inset illustrates the color code used throughout the thesis to identify individual features. Medial plot: Continuous vertical (z) trajectories of the two front paws. Final plot: Side-to-side (y) position of proximal (green) to distal (yellow) tail segments vs time. **(C)** Individual strides were divided into swing and stance phases for further analysis.

For posterior data analysis, the paw trajectories were automatically divide into stride cycles. The stride cycle consists in two phases, the swing (transfer) and stance (support) phases. In the swing phase, the limb is moving relative to the body. It initiates when the paw leaves the floor and reaches the anterior extreme position. During the stance phase the paw is in contact with the floor (**Figure 2.4 C**). For the validation of the system, hand label trajectories (x,y,z position) were used to compare the trajectories resulted from the automated tracking. Validation of the tracking is provided in (**Figure 2.5**).

Finally, with this high throughput system it was possible to ran 34 wildtype mice in approximately one week and collect in total 36,369 strides, which corresponds to 1069 ± 266 strides per mouse and 267 ± 66 strides per paw.

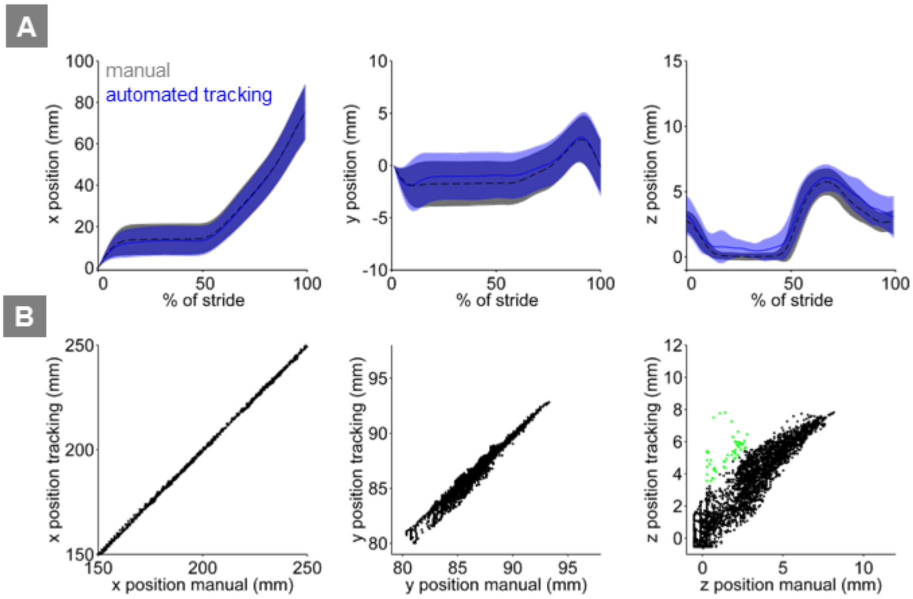

**Figure 2.5. LocoMouse tracking validation.**

**(A)** Comparison of manual (gray) and automated tracking (blue) for front left paw across 3 dimensions. From left to right, plots show normalized x, y, and z paw position aligned to stance onset (n = 43 strides from 9 movies of 3 mice). **(B)** Scatterplots of manual vs automated tracking positions (x, y, and z) for all frames (n = 4194) of the same 9 movies. Values where the difference between manual and automated tracking are larger than average paw size are color-coded in green. Correlation coefficients are Pearson's r.

## 2.3.2 Wild-type data analysis: Individual limbs in wild-type mice vary consistently with walking speed and body-size

### 2.3.2.1 Using linear mixed effects models to predict basic stride parameters

We first analyzed basic stride parameters for individual limbs of wildtype control mice (**Figure 2.6**). Parameters such as stride length (mm), cadence (strides/s), swing velocity (m/s), and stance duration (ms), along with the mouse's walking speed, were measured for each stride. The data were highly variable (**Figure 2.6 A**). The walking speed of the mice was similarly variable (**Figure 2.6 B**). We therefore sorted all strides for individual mice into speed bins in a stridewise manner and analyzed them with respect to the mouse's walking speed.

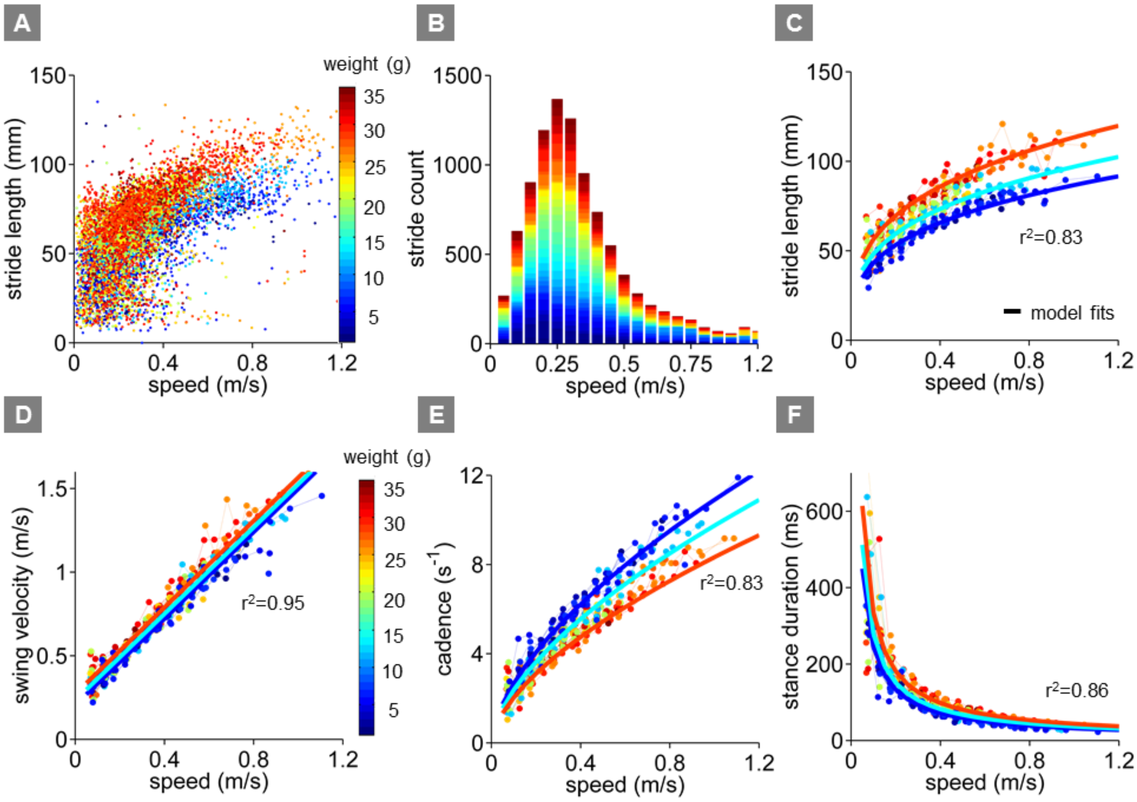

**Figure 2.6. Basic stride parameters can be predicted using only walking speed and body size.**

**(A)** Stride length vs walking speed for 9602 individual strides of the front right paws of 34 wildtype mice are color-coded by weight for each individual animal. **(B)** Histogram of average walking speeds for each stride from (**A**). Strides are divided into speed bins of 0.05 m/s. (**C**–**F**) Stride length, cadence (1/stride duration), swing velocity, and stance duration vs walking speed, respectively. For each parameter, speed-binned median values are shown for each animal (solid circles, color coded by weight). Data for each animal are connected across speeds with a thin dotted line. Thick lines are the output of the linear mixed-effects model, for 3 example weights across walking speeds (blue: 9g, cyan:19g, red: 33g). Marginal R-squared values for each linear mixed model are shown for each parameter.

The median values of stride parameters for each mouse across speed bins are shown in **Figure 2.6 C–F** (dots connected by dashed lines). Each parameter measured, including stride length, cadence, swing velocity, and stance duration (**Figure 2.6 C–F**), varied consistently with the walking speed of the mouse. Cadence and stride length increased with walking speed, indicating that faster walking in mice is associated with longer, more frequent strides (Clarke and Still 1999, Lalonde and Strazielle 2007, Batka, Brown et al. 2014). These changes, in turn, resulted from linear increases in swing velocity and steep decreases in stance duration with increasing walking speed. Further subdividing the data by the body weight of each animal (**Figure 2.7**) revealed that much of the remaining variability in each parameter could be accounted for by the mouse's body size (**Figure 2.6**, color-coded by weight).

To quantify the influence of walking speed, body size, and other potential factors on these basic stride parameters, 36,369 strides from an average of 1069 ± 266 strides in 34 mice were analyzed (**Figure 2.6**). For each parameter, we first linearized the data by fitting appropriate functions (e.g., linear, power) to the data with respect to walking speed.

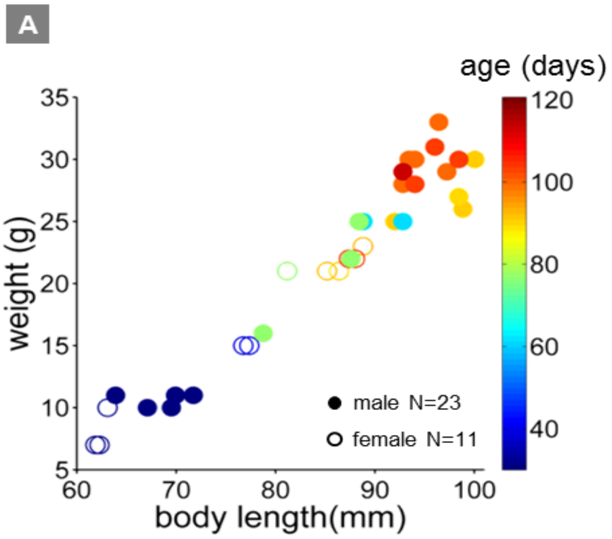

**Figure 2.7. Properties of wildtype mice used for linear mixed-effects model**

**(A)** Properties of wildtype mice used for linear mixed-effects model. A total of 34 wild-type C57BL/6 mice were used for the linear mixed-effects model in Figure 2.6. Each individual WT animal is plotted as a circle (open circles, females, N = 11; closed circles, males, N = 23). Symbols are color-coded by age. The diverse group included a variety of ages (30–114 days), body lengths (61–100 mm), and weights (7–33g).

Then we generated a multilevel linear mixed-effects model that included potential predictor variables speed, weight, body length, age, and gender either alone or in combination and asked to what extent they accurately predicted the measured parameter. This analysis revealed that the value of each stride parameter was readily predicted based solely on walking speed and body weight (**Table 2.1A**). While basic stride parameters also varied with gender and age, these effects were related to differences in body size (**Table 2.1B**); adding neither age nor gender improved the predictions once body size was taken into account. The resulting best-fit models are plotted as thick lines in **Figure 2.6 C–F**. These results indicate that the equations in **Table 2.1A** provide quantitative predictions of paw stride parameters for mice of a given size, walking at a particular speed. For a more detail description of the linear mixed effects model please see Methods section.

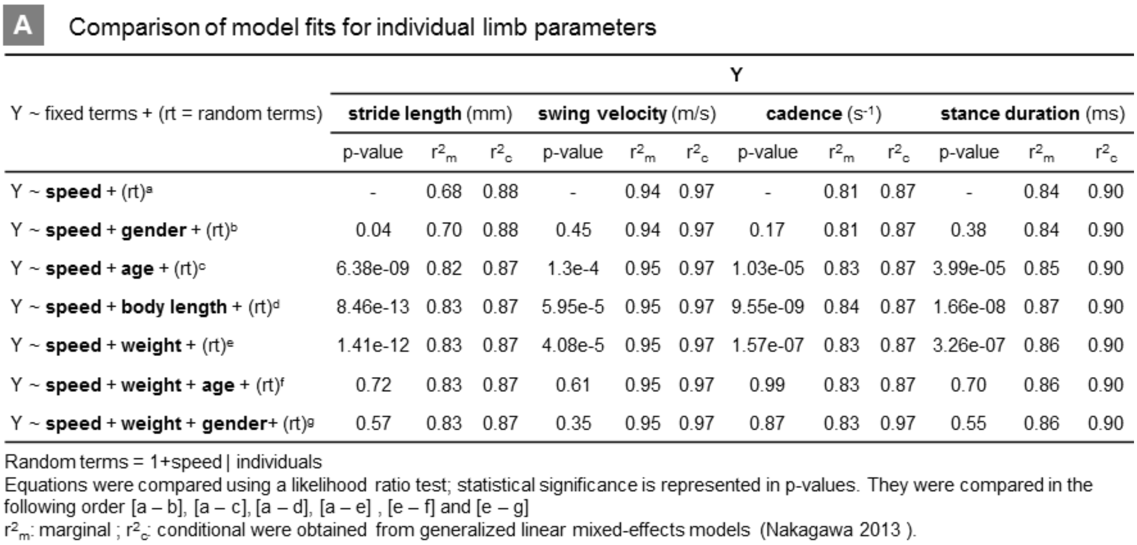

**A** Comparison of model fits for individual limb parameters

| Y ~ fixed terms + (rt = random terms) | Y | | | | | | | | | | | |
|---|---|---|---|---|---|---|---|---|---|---|---|---|
| | **stride length** (mm) | | | **swing velocity** (m/s) | | | **cadence** ($s^{-1}$) | | | **stance duration** (ms) | | |
| | p-value | $r^2_m$ | $r^2_c$ | p-value | $r^2_m$ | $r^2_c$ | p-value | $r^2_m$ | $r^2_c$ | p-value | $r^2_m$ | $r^2_c$ |
| Y ~ **speed** + (rt)[a] | - | 0.68 | 0.88 | - | 0.94 | 0.97 | - | 0.81 | 0.87 | - | 0.84 | 0.90 |
| Y ~ **speed** + **gender** + (rt)[b] | 0.04 | 0.70 | 0.88 | 0.45 | 0.94 | 0.97 | 0.17 | 0.81 | 0.87 | 0.38 | 0.84 | 0.90 |
| Y ~ **speed** + **age** + (rt)[c] | 6.38e-09 | 0.82 | 0.87 | 1.3e-4 | 0.95 | 0.97 | 1.03e-05 | 0.83 | 0.87 | 3.99e-05 | 0.85 | 0.90 |
| Y ~ **speed** + **body length** + (rt)[d] | 8.46e-13 | 0.83 | 0.87 | 5.95e-5 | 0.95 | 0.97 | 9.55e-09 | 0.84 | 0.87 | 1.66e-08 | 0.87 | 0.90 |
| Y ~ **speed** + **weight** + (rt)[e] | 1.41e-12 | 0.83 | 0.87 | 4.08e-5 | 0.95 | 0.97 | 1.57e-07 | 0.83 | 0.87 | 3.26e-07 | 0.86 | 0.90 |
| Y ~ **speed** + **weight** + **age** + (rt)[f] | 0.72 | 0.83 | 0.87 | 0.61 | 0.95 | 0.97 | 0.99 | 0.83 | 0.87 | 0.70 | 0.86 | 0.90 |
| Y ~ **speed** + **weight** + **gender**+ (rt)[g] | 0.57 | 0.83 | 0.87 | 0.35 | 0.95 | 0.97 | 0.87 | 0.83 | 0.97 | 0.55 | 0.86 | 0.90 |

Random terms = 1+speed | individuals
Equations were compared using a likelihood ratio test; statistical significance is represented in p-values. They were compared in the following order [a – b], [a – c], [a – d], [a – e] , [e – f] and [e – g]
$r^2_m$: marginal ; $r^2_c$: conditional were obtained from generalized linear mixed-effects models (Nakagawa 2013 ).

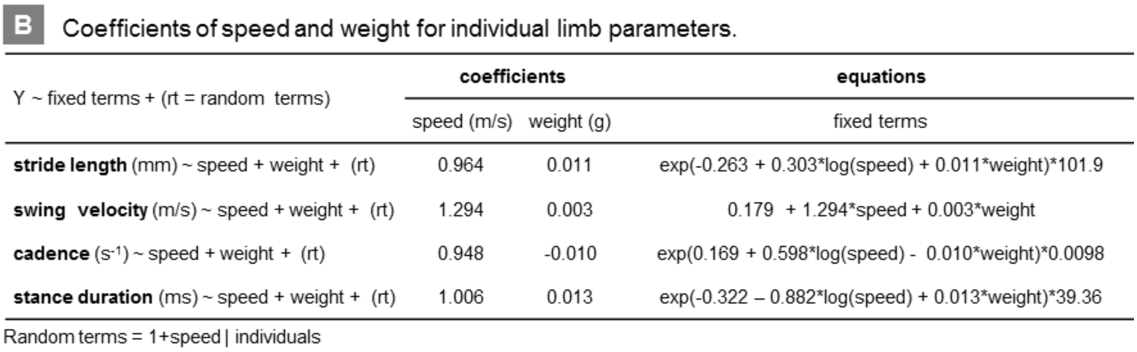

**B** Coefficients of speed and weight for individual limb parameters.

| Y ~ fixed terms + (rt = random terms) | coefficients | | equations |
|---|---|---|---|
| | speed (m/s) | weight (g) | fixed terms |
| **stride length** (mm) ~ speed + weight + (rt) | 0.964 | 0.011 | exp(-0.263 + 0.303*log(speed) + 0.011*weight)*101.9 |
| **swing velocity** (m/s) ~ speed + weight + (rt) | 1.294 | 0.003 | 0.179 + 1.294*speed + 0.003*weight |
| **cadence** ($s^{-1}$) ~ speed + weight + (rt) | 0.948 | -0.010 | exp(0.169 + 0.598*log(speed) - 0.010*weight)*0.0098 |
| **stance duration** (ms) ~ speed + weight + (rt) | 1.006 | 0.013 | exp(-0.322 – 0.882*log(speed) + 0.013*weight)*39.36 |

Random terms = 1+speed | individuals

**Table 2.1 –Using linear mixed effects models to predict individual limb parameters**

**(A)** Comparison of model fits for basic stride parameters. Speed, gender, age, body length, weight (fixed terms) and subject (random term) were used as predictor variables in the linear mixed-effects model. Table rows show tested equations for predicting stride parameters and values used for selection criteria of the resulting predictive model. p-values reported for each term are the outcome of a likelihood ratio test comparing indicated equations (superscripts). The last two lines (f, g) indicate that age and gender did not improve the predictions beyond the inclusion of speed and body weight. **(B)** Coefficients of speed and weight for basic stride parameters. The final equations for each stride parameter included speed and weight as fixed-term predictor variables; subject was included as a random-term. Coefficient values for fixed terms are represented. These equations can be used to predict stride parameters for a given mouse walking at a particular speed**.**

## 2.4 Discussion

The LocoMouse system is an automated, markerless 3D tracking and analysis system for mouse locomotion. It provides detailed trajectory information in 3D for all four paws, the nose, and tail. We used LocoMouse to analyze locomotor coordination in freely walking mice. A multilevel mixed effects linear modeling approach accurately predicted the value of gait parameters for individual limbs across trials and across mice, based solely on body size and walking speed.

The LocoMouse system presents a number of technical advantages over existing systems for analyzing mouse locomotion. Available systems have tended to either emphasize throughput (Hamers, Lankhorst et al. 2001), or the collection of more detailed trajectories (Leblond, L'Espérance et al. 2003, Kale, Amende et al. 2004, Garnier, Falempin et al. 2008, Zörner, Filli et al. 2010).

LocoMouse is unique in that it combines these features, allowing mice to walk as naturally as possible through the corridor while increasing throughput with fully automated data collection and analysis (Anderson and Perona 2014). The high spatiotemporal resolution of the tracking system itself provides high sensitivity, as evidenced by our ability to distinguish between gait parameters of animals of different sizes and subtle changes in limb trajectories across speeds.

The LocoMouse system has several limitations:

- Joints cannot be tracked and analyzed in an automatic way.
- The tracking system is restricted to the training conditions of the support vector machine:
    - Mice must cross a linear corridor,
    - Movies must be in black and white color with a high spatial and temporal resolution and light source
    - Finally, the system can only track black 6 mice.

Beyond the technical advantages, establishing a comprehensive framework for analyzing the large, multidimensional dataset generated by LocoMouse was essential. The multilevel linear mixed effects modeling approach and the quantitative analysis of interlimb and whole-body coordination were crucial for identifying specific, core features of ataxia (a more detail analysis will be presented in chapter 3).

We found that the motion of individual limbs was highly predictable based on walking speed and body weight across wildtype mice, even down to the level of 3D trajectories. Nearly all previous studies have failed to account for differences in walking speed and body size when comparing gait parameters across mice, though this is clearly critical (Koopmans, Deumens et al. 2007, Cendelín, Voller et al. 2010, Wuehr, Schniepp et al. 2013, Batka, Brown et al. 2014). Moreover, taking account of walking speed and body size allowed us to account quantitatively for variability across mice, which can reduce the number of animals and trials needed for experiments.

# 3

# Quantifying specific impairments in cerebellar ataxic mice (*pcd* and *reeler* mice)

**3.1. Introduction**

**3.2. Methods**

**3.3. Results**

  **3.3.1. Single limb:** Differences in forward trajectories of the paw can be accounted for by walking speed and body size; impairments are restricted to off-axis movement

  **3.3.2. Interlimb:** Front-hind coordination is specifically impaired, while left-right coordination is preserved

  **3.3.3. Whole-body:** In *pcd* and *reeler* the side-to-side (y) tail movement can be predicted by a passive model

**3.4. Discussion**

**Results published:**
Ana S. Machado, Dana M. Darmohray, João Fayad, Hugo G. Marques, Megan R. Carey, A quantitative framework for whole-body coordination reveals specific deficits in freely walking ataxic mice. **eLife** (2015) DOI**:** http://dx.doi.org/10.7554/eLife.07892

**Manuscript in preparation:**
Ana S. Machado and Megan R. Carey, Assessing specific locomotor impairments in *reeler* mice.

Author contributions in this chapter for pcd mice:
ASM and DMD equal contribution. ASM, DMD and MRC, Conception and design, Analysis and interpretation of data. ASM, Acquisition of data and Analysis of individual limb and tail. DMD, Analysis of limb trajectories, interlimb coordination and support pattern. MRC wrote the manuscript

## 3.1 Introduction

The systematic analysis of gait parameters across mice presented in the chapter 2 provided a starting point for quantifying locomotor deficits of ataxic mice. Several spontaneous mouse mutants have been identified based on their visible gait ataxia (Mullen, Eicher et al. 1976, Lalonde and Strazielle 2007, Cendelin 2014). Many of these mouse lines exhibit abnormal cell patterning within the cerebellum, with different spatiotemporal patterns of neural degeneration. Interestingly, the specifics of the motor deficits exhibited by these mice are also variable (Lalonde and Strazielle 2007, Brooks and Dunnett 2009, Sheets, Lai et al. 2013, Cendelin 2014). Thus, understanding the relationship between circuit dysfunction and motor impairment could provide clues into neural circuit mechanisms of motor coordination. Here I will quantify and analyze two visibly ataxic cerebellum mutant mice. The Purkinje cell degeneration (*pcd*) and *reeler* mice.

### Purkinje cell degeneration (*pcd*) mice

The Purkinje (Pkj) cell degeneration (*pcd*) mouse is a recessive mutant characterized by complete post-natal degeneration of cerebellar Purkinje cells (**Figure 3.1 B, E**) and subsequent partial loss of cerebellar granule cells (Chen, Bao et al. 1996, Le Marec and Lalonde 1997, Lalonde and Strazielle 2007, Cendelin 2014); The gene affected encodes ATP/GTP binding protein 1 (Fernandez-Gonzalez, La Spada et al. 2002). *Pcd* mice can be easily identified by eye based on their ataxic, uncoordinated movements (Mullen, Eicher et al. 1976, Le Marec and Lalonde 1997). *Pcd* mice exhibit impaired rotarod performance and deficits in eyelid conditioning that have been attributed to their cerebellar abnormalities (Chen, Bao et al. 1996, Le Marec and Lalonde 1997). Perhaps surprisingly, given the severity of their anatomical phenotype, the motor deficits of *pcd* mice are relatively mild compared to other spontaneous ataxic mutants (Le Marec and Lalonde 1997, Lalonde and Strazielle 2007).

### *Reeler* mice

The homozygous *reeler* mice are a classic mutant ataxic mice discovered in 1951 (Falconer 1951, Cendelin 2014). *Reeler* mice have an autosomal recessive mutation ($Reln^{rl}$). This gene is involved in neural cell migration (Beckers, Bar et al. 1994). Thus, the lack of it in the mutant mice can cause several defects, in particular abnormal localization of neurons and failure of neuronal layer formation. Several brain regions are affected such as: cerebellum (Hamburgh 1963, Terashima, Inoue et al. 1983), hippocampus (Stanfield and Cowan 1979), neocortex (Mikoshiba, Kohsaka et al. 1980), inferior olive (Blatt and Eisenman 1988) and substantia nigra (Kang, Kim et al. 2010). Abnormal cerebellum foliation and reduce size is observed in *reeler* mice (**Figure 3.1 C**). Besides having lower density of Pkj cells and granule cells, the neurons also have abnormal locations (Goffinet, So et al. 1984, Castagna, Aimar et al. 2014). Homozygous *reeler* mice are characterized by an ataxic and reeling gait, with difficulties in maintaining their hindquarters upright (Cendelin 2014). Reeler mice also exhibit a poor performance in rotarod, stationary beam and water maze tests (Cendelin 2014).

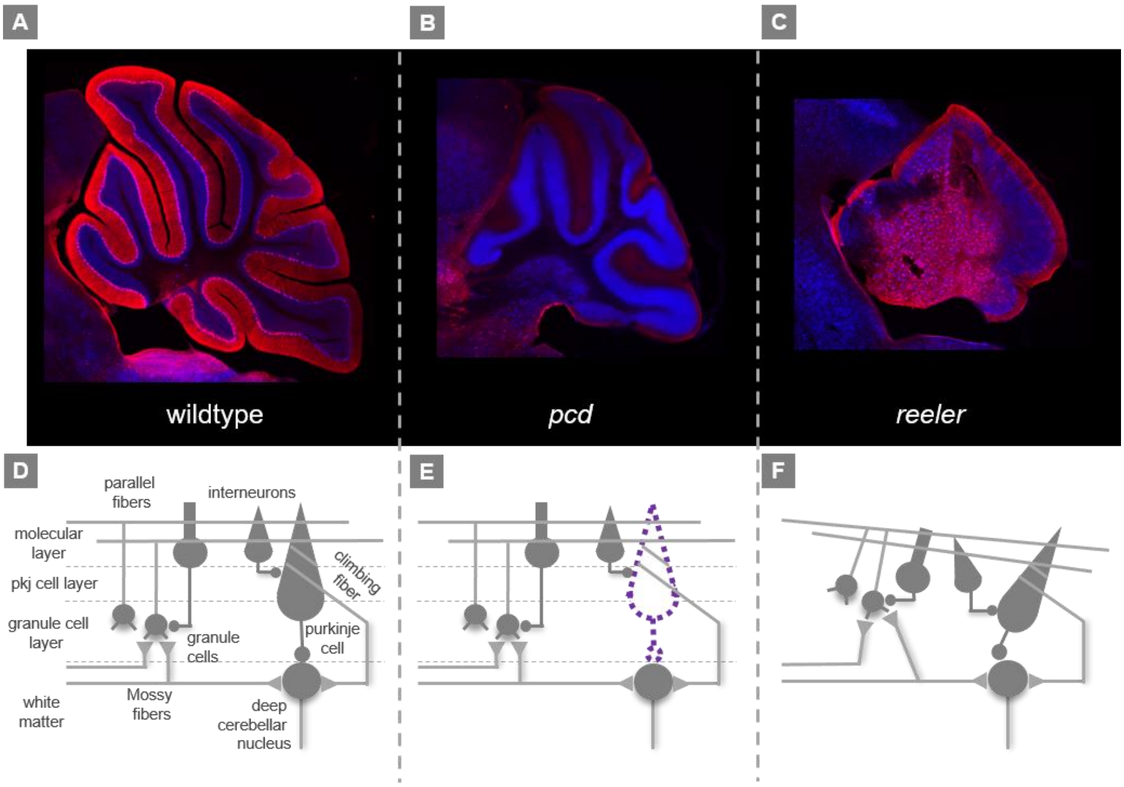
A
B
C
wildtype
pcd
reeler
D
E
F
parallel fibers
interneurons
molecular layer
climbing fiber
pkj cell layer
granule cell layer
granule cells
purkinje cell
white matter
Mossy fibers
deep cerebellar nucleus

**Figure 3.1. Sagittal sections of the mouse brain to compare cerebellar morphology between wildtype, *pcd* and *reeler* mice.**

Sagittal sections of the mouse brain, with a focus on the cerebellum region, for **(A)** wildtype, **(B)** *pcd* and **(C)** *reeler* mice. Each section was stained with Nissl for neurons visualization and anti-calbindin to reveal purkinje cells. **(B)** In *pcd* mice the cerebellum morphology is maintained, when compared to (A) wildtype, however the amount of anti-calbindin staining is clearly reduce. This is a consequence of purkinje cell degeneration. The size of the cerebellum **(C)** in *reeler* mice is much smaller than **(A)** wildtype mice. Besides that, *reeler* mice also have an abnormal morphology and neurons localization. **(D-F)** Diagrams of the cerebellar neuronal circuit for each mouse, **(D)** wildtype, **(E)** *pcd* mice (purple – lack of pkj cell), **(F)** *reeler* mice (abnormal neurons localization).

In the previous chapter, a detailed analysis of individual limbs was performed. Now I will extend this analysis to quantify limb trajectories in 3D and whole body coordination. Thus, the final goal on this chapter is to use LocoMouse to establish a quantitative framework for locomotor coordination in mice and analyze the deficits of visibly ataxic cerebellum mutant mice.

## 3.2 Methods

**Animals**

All procedures were reviewed and performed in accordance with the Champalimaud Centre for the Unknown Ethics Committee guidelines, and approved by the Portuguese Direcção Geral de Veterinária (Ref. No. 0421/000/000/2015).

Heterozygous Purkinje cell degeneration mice on a C57BL/6 background were obtained from Jackson labs (#0537 B6.BR-Agtpbp1*pcd*/J). Heterozygous *reeler* ($Reln^{rl}$) mice on a C57BL7/6 were obtained from Jackson labs (#000235 B6C3Fe al a- $Reln^{rl}$ /J).

Experiments were conducted in two groups: A) homozygous *pcd* mice (n=3052; N=3 mice; 2 females, 1 male; 10-16 g; run at several ages each between 41-154 days old) and their littermates (n=2256; N=7 mice; 3 females, 4 males; 15-40 g; 34-190 days old). Size-matched controls for *pcd* animals (n=3400; N=11 mice) were taken from the wildtype data set. B) homozygous *reeler* mice (n=1965; N=7 mice; 2 females; 5 males; 8-18g; 35-52 days old) and their wild type littermates (n=1892; N=12 mice; 8 females, 4 males; 12-25 g; 36-52 days old).

**Data collection**

Mice were handled by the experimenter and allowed to acclimate in the LocoMouse setup for several minutes on multiple occasions before data collection. Animals were weighed before each session. Mice walked freely between two dark boxes on either end of the glass corridor. The automatic triggering system was critical for allowing mice to self-initiate trials, which reduced animal stress without compromising the quantity of data collected. No food or water restriction or reward was used.

10-25 corridor passages (trials) were collected in each of five daily sessions. For *pcd* and littermates we collected an average of 4252 ± 778 strides per *pcd* mouse (1063 ± 32 strides per animal per paw) and 1310 ± 934 strides per littermate mouse (328 ± 11 strides per animal per paw). For *reeler* and littermates we collected an average of 1079 ± 568 strides per *reeler* mouse (208 ± 147strides per animal per paw) and 622 ± 346 strides per littermate mouse (157 ± 87 strides per animal per paw).

Animals were not required to walk continuously throughout a trial; if the animal stopped mid-trial, the data before and after the halt were still analyzed.

**Data analysis**

The stride cycles of individual paws were automatically broken down into swing and stance phases based on the first derivative of the paw position trajectories. Individual strides were defined from stance onset to subsequent stance onset. For each stride, average *walking speed* was calculated by dividing the forward motion of the body center during that stride by the stride duration. All data was sorted into speed bins (0.05 m/s bin width) in a stridewise manner, with a minimum stride count criterion of 5 strides per bin, per animal. Individual limb movements and interlimb coordination were calculated as follows:

**Table 1**: Gait parameters

| **Limb parameters** | **Definitions** |
|---|---|
| Cadence | Inverse of stride duration |
| Swing velocity | Displacement of single limb during swing phase divided by swing duration |
| Stride length | Displacement from touchdown to touchdown of single limb |
| Stance duration | Time in milliseconds that foot is on the ground during stride |
| Trajectories | Trajectories were aligned to swing onset and resampled to 100 equidistant points using linear interpolation. Interpolated trajectories were then binned by speed and the average trajectory was computed for each individual animal and smoothed with a Savitzky-Golay first-order filter with a 3-point window size |
| Stance phase | Relative timing of limb touchdowns to stride cycle of reference paw. Calculated as: (stance time−stance time$_{\text{reference paw}}$)/stride duration |
| Supports | Support types were categorized by number of paws on ground expressed as a percentage of the total stride duration for each stride. Paw support categories are four, three, two diagonals, two other (homolateral and homologous), one, and zero. |
| Paw distance | The x,y distance from where the front paw lifted off to where the ipsilateral hind paw touched down on the subsequent stride. |
| Double support: | Double support for each limb is defined as the percentage of the stride cycle between the touch down of a reference paw to lift-off of the contralateral paw. Because at higher speeds (running), the opposing limb lifts off before the reference paw touches down, we included negative double support by looking backwards in time by 25% of the stride cycle duration. Positive values of double support indicate that contralateral lift-off occurred after reference paw touch down, and negative values indicate that contralateral lift-off occurred before reference paw touch down. |

### Tail and nose phases

For each speed bin we correlate the stridewise tail and nose trajectories with the trajectory given by the difference between the forward position of the hind right paw and the forward position of the hind left paw (also normalized to the stride). The phase is then calculated by the delay in which this correlation is maximized.

**Correlation matrices**

Correlation coefficients were computed for average z trajectories normalized to 100% of the FR stride cycle.

**Multi-level linear mixed-effects models and statistical analysis**

Because of the complex nature of the data set, including nested data with varying number of trials per animal and data points per speed bin, data analysis and statistical comparisons were performed with linear mixed effects models.

**Statistical analyses**

Statistical analyses were done in Matlab and R. For all comparisons, models were selected by comparing equations specifying additive fixed-effects terms with those specifying n-way interaction terms using a likelihood-ratio test and inspection of statistical significance of included terms. Depending on the comparison, fixed-effects terms included a subset of the following variables: speed, genotype and paw. All models were random-intercepts models with subject as a random covariate. Unless otherwise indicated, results are reported as conditional F tests with Satterthwaite degrees of freedom correction. All variability analyses were based on coefficients of variation (CV).

## 3.3 Results

### 3.3.1 Single limb: Differences in forward trajectories of the paw can be accounted for by walking speed and body size; impairments are restricted to off-axis movement

#### Changes in stride parameters are predicted by changes in walking speed and body size

*Pcd* and *reeler* mice were visibly ataxic when walking on the LocoMouse setup. Consistent with previous studies of cerebellar ataxia in mice (Fortier, Smith et al. 1987, Wang, Parris et al. 2006, Cendelín, Voller et al. 2010, Veloz, Zhou et al. 2015), comparing the basic stride parameters of visibly ataxic mice, in particularly *pcd* mice, with littermate control mice revealed that the strides, overall, were quite different (**Figure 3.2 C–E**). Stride lengths were shorter (**Figure 3.2 C,** purple shadows), even when changes in walking speed (**Figure 3.2 A**) were taken into account. Cadence and stance durations were also altered (**Figure 3.2 D,E** purple shadows).

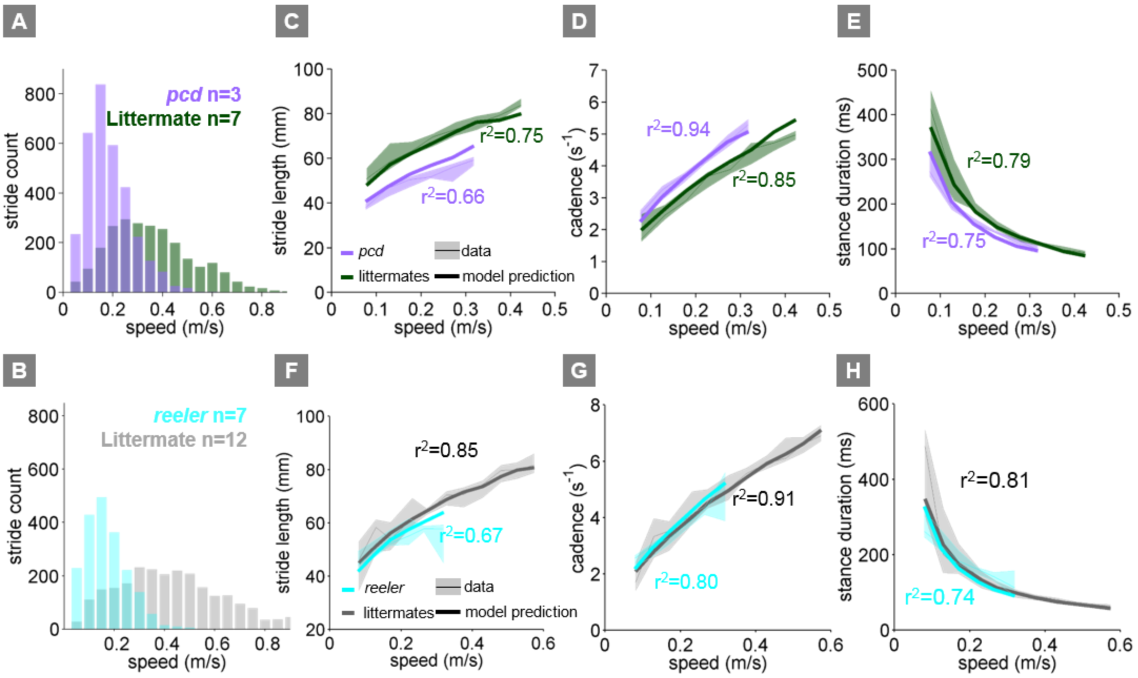

**Figure 3.2. Differences in forward paw trajectories in *pcd* can be accounted for by walking speed and body size. *Reeler* mice and littermate controls have similar body size.**

**(A-B)** Histogram of walking speeds, divided into 0.05 m/s speed bins for *pcd* (purple N=3), *pcd* littermate controls (green, N=7), *reeler* (cyan N=7) and *reeler* littermate controls (grey, N=12). **(C-H)** Stride length **(C, F)**, cadence **(D**,**G**, 1/ stride duration**)** and stance duration **(E-H)** vs walking speed for *pcd* mice (purple), *reeler* mice (cyan), *pcd* littermate controls (green) and *reeler* littermate controls (grey). For each parameter, the thin lines with shadows represent median values ± 25th, 75th percentiles. Thick lines represent the predictions calculated using the mixed-effect models described in Figure 2.6 and Table 2.1

Since *pcd* and *reeler* mice, like many ataxic animals, are smaller than controls (**Figure 3.3**), and given that they walk more slowly (**Figure 3.2 A**), we asked to what extent the altered stride parameters in these mutant mice could be accounted for simply by changes in body size and walking speed. To do this we used the equations derived from the linear mixed-effects models in **Figure 2.6** to predict stride parameters across walking speeds for mice the size of the *pcd*, *reeler* mice and their littermates. The models accurately predicted stride parameters for the littermates, which were not visibly ataxic (**Figure 3.2 C–H**, green and grey: thick lines represent model predictions). Surprisingly, we also found that the models accurately predicted stride parameters for *pcd* and *reeler* mice (**Figure 3.2 C–H**, purple and cyan). Thus, although stride parameters of *pcd* mice were different overall from controls (**Figure 3.2 C–E**, purple vs green shadows), they were comparable to those predicted for control mice of similar body size walking at similar speeds (**Figure 3.2 C–E**, the purple thick lines representing the model predictions fall on top of the data in the shadows).

No differences across *reeler* mice and littermate controls was observed for the front right paw (**Figure 3.2 B, F-H**). This could be explained by the small differences between their body size (**Figure 3.3 A**) which reinforce the idea that differences observed in *pcd* and respective littermates are accounted by changes in body size.

Moreover, a direct comparison between stride parameters for *pcd* mice and size-matched controls walking at the same speeds revealed no difference between the two groups (**Figure 3.3**) (stride length $F_{(14,1)}$ = 0.70, p = 0.42; cadence $F_{(14,1)}$ = 0.004, p = 0.95; stance duration $F_{(14,1)}$ = 1.89, p = 0.17).

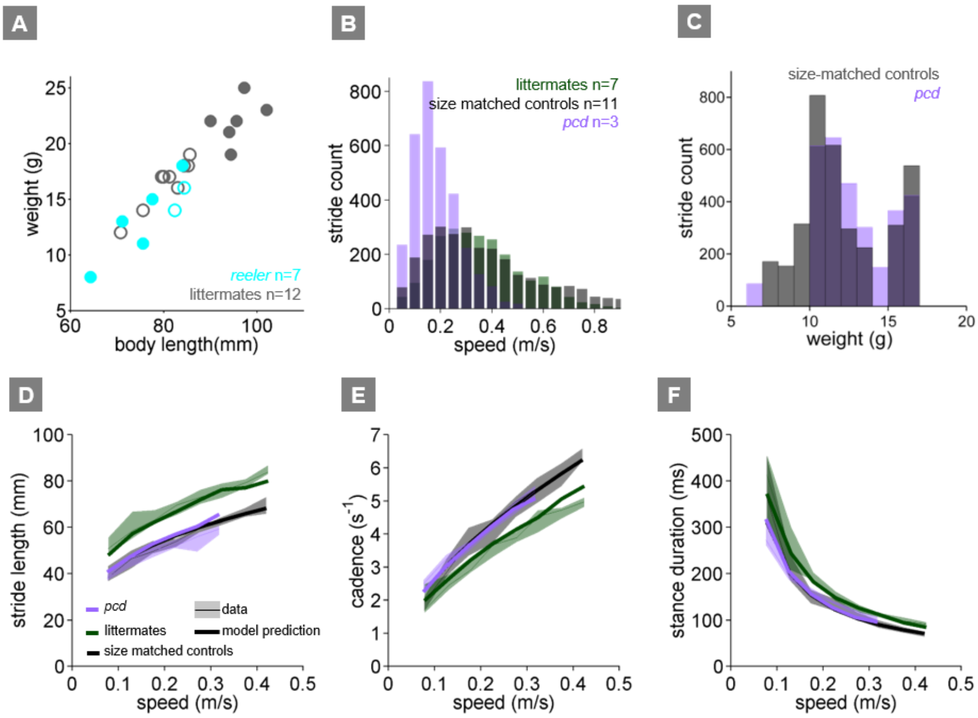

**Figure 3.3. Basic stride parameters for *pcd* are not different from their size-matched controls. *Reeler* mice and littermates control have comparable body size.**

**(A)** Properties of homozygous *reeler* mice (cyan n=7) and littermates controls (grey n=12). **(B)** Histogram of walking speeds, divided in 0.05 m/s speed bins for *pcd* (purple, N=3 mice, n=3052 strides), littermate controls (green, N=7 mice, n=2256 strides) and size matched controls (black, N=11 mice, n=3400 strides). **(C)** Histogram of stride counts by weight for size-matched controls and *pcd*. **(D-F)** Basic stride parameters. For each parameter, thick lines represent the prediction, from the mixed-effects models derived from wildtype data in Figure 2.6 (including speed and weight as predictor variables), for each group. *Pcd* (average weight=12g; purple line), control littermates (average weight=26g; blue line) and size-match controls (average weight=12g; black line). **(D)** Stride length values vs walking speed for *pcd*, littermate controls and size-matched controls (median ± 25th,75th percentile). Data are represented by thin lines and shadows, thick lines are model predictions. **(E** and **F)** Temporal measures of the step cycle; cadence (inverse of stride duration) and stance duration, respectively (median ± 25th,75th percentile).

Although, in *reeler* mice basic stride parameters of the front right paw was not altered (**Figure 3.2 B, F-H**) the same was not true for the hind paws. While stride length, cadence and stance duration were maintained, differences in swing duration between *reeler* mice and littermate control were observed (**Figure 3.4**).

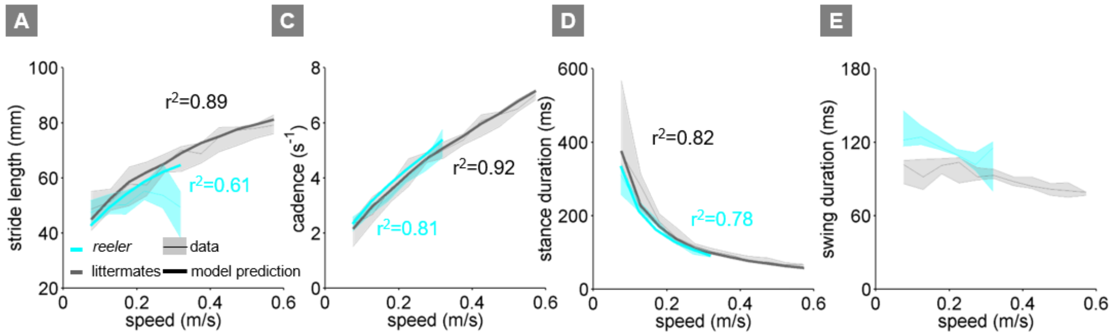

**Figure 3.4 Basic stride parameters for hind right paw. Differences in swing duration**. **(A-E)**

Basic stride parameters. **(A)** Stride length (mm) **(C)** cadence ($s^{-1}$) **(D)** stance duration (ms) and **(E)** swing duration (ms) vs walking speed for *reeler* mice (cyan) and *reeler* littermate controls (grey), relative to hind right paw. For each parameter, the thin lines with shadows represent median values ± 25th, 75th percentiles. Thick lines represent the predictions calculated using the mixed-effect models described in Figure 2.6 and Table 2.1. Since we were not able to predict accurately the swing duration parameter, no model prediction was plotted in **E**.

Next we investigated the possibility that there could be changes in variability of stride parameters in *pcd* and *reeler* mice that were not apparent in the averaged data. Analysis of the coefficient of variation revealed that swing length variability was unchanged in *pcd* compared to size matched controls ($F_{(81,1)=}$0.14, p = 0.0.71). Surprisingly, both cadence and stance duration were less variable in *pcd* (cadence:$F_{(80,1)=}$6.90, p < 0.05; stance duration: $F_{(80,1)=}$6.90, p < 0.05) .

Taken together, these results demonstrate that basic stride parameters do not capture the ataxic symptoms of *pcd* and *reeler* mice, and highlight the importance of accounting for walking speed (Koopmans, Deumens et al. 2007, Cendelín, Voller et al. 2010, Batka, Brown et al. 2014) and using size-matched control animals when analyzing locomotor parameters. For this reason, *pcd* and *reeler* animals are compared with size-matched controls from here on (**Figure 3.3**).

### Strides of *pcd* and *reeler* mice show specific impairments in off-axis paw trajectories

It has been previously hypothesized that detailed analysis of paw trajectories would capture the gait abnormalities of ataxic mice like *pcd* and *reeler*, but detailed 3D paw kinematics have not been described for mice. We analyzed the continuous 3D paw trajectories for both wildtype, *pcd* and *reeler* mice (**Figure 3.5** and **Figure 3.6**). In the wildtype mice, the instantaneous forward paw velocity profile changes with speed, the peak paw velocity increases with faster speeds. In vertical (z) and side-to-side (y) movement there is no significant differences between the different speeds (**Figure 3.5**).

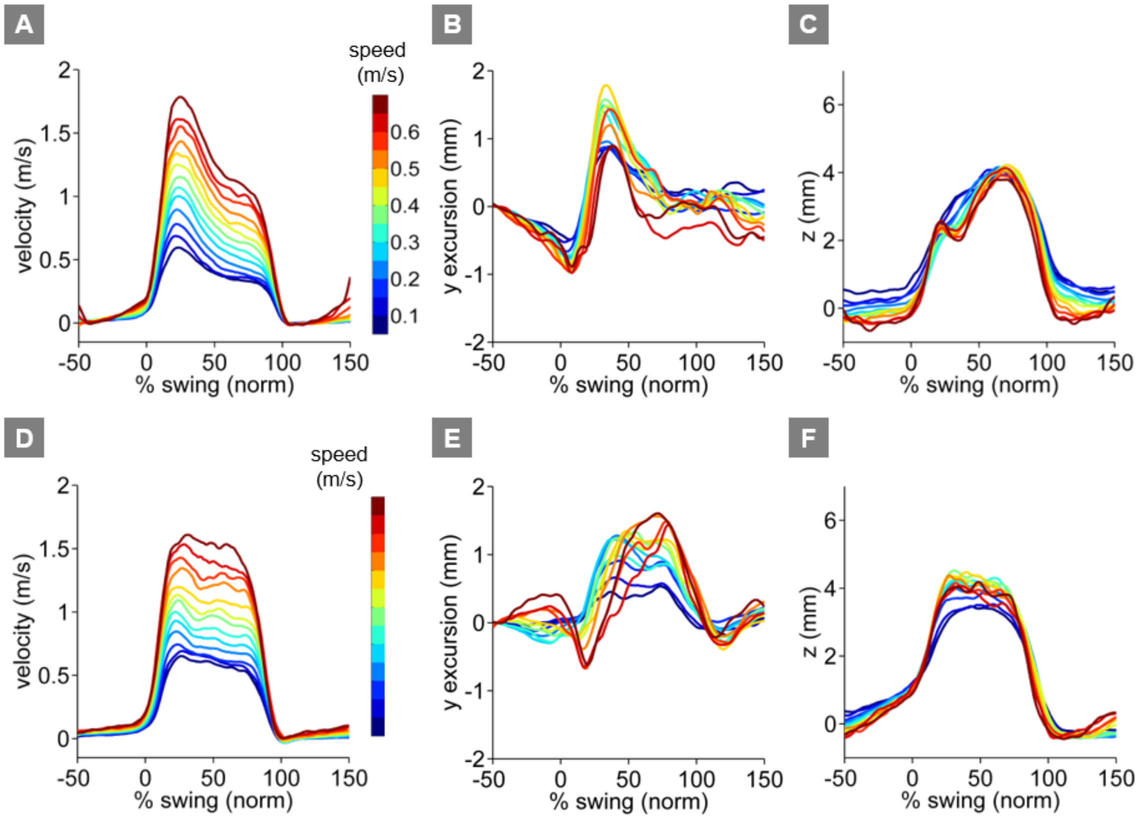

**Figure 3.5. 3D paw trajectories for wildtype controls.**

**(A-C)** Average 3D trajectories for front right paw of wildtype control group (N=34; n=9602 strides) during swing phase. Traces are binned and color coded by walking speed. **(A)** Instantaneous forward (x) velocity. **(B)** side-to-side (y) excursion **(C)** vertical (z) position relative to ground. **(D-F)** Same as above but for hind right paw of wildtype control group.

Surprisingly, we found that the instantaneous forward paw velocity profiles for all paws in *pcd* and for front paws in *reeler* mice were not distinguishable from those of size-matched controls, across speeds (**Figure 3.6 A, E; Figure 3.7 A**). However, hind paws forward velocity (**Figure 3.7 C**) in *reeler* mice were much slower than size-matched controls ($F_{(82.9,1)=}$27.3, p<0 0.001). Paw velocity peaked early during swing and decelerated before stance onset across walking speeds in both control, *pcd* and *reeler* mice (**Figure 3.6 A, E; Figure 3.7 A**). Peak swing velocities increased with faster walking speeds but did not vary by genotype (*pcd:* $F_{(10.97,1)=}$.092, p = 0.77, *reeler*: $F_{(138.1,1)=}$.032, p = 0.86). There was also no difference in variability of peak swing velocity between genotypes in *pcd* mice ($F_{(81,1)=}$0.27, p = 0.60). This surprising result reveals that even detailed forward paw trajectories are normal in *pcd* and *reeler* mice, once changes in walking speed and body size are taken into account.

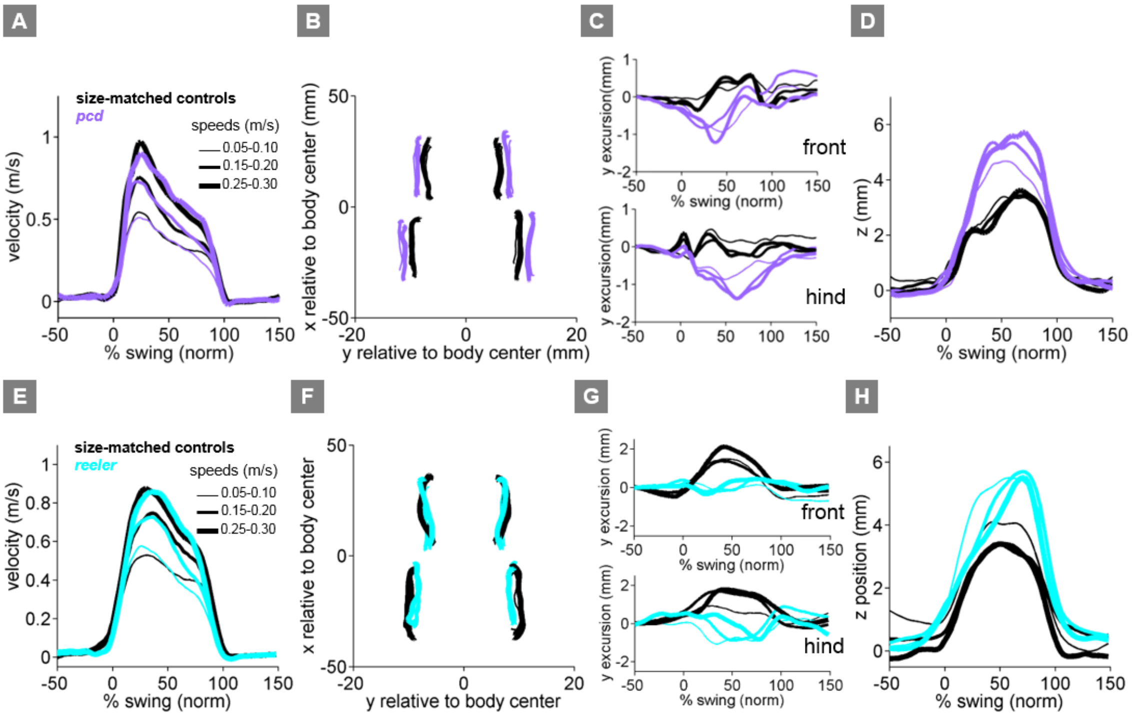

**Figure 3.6. Impairments are restricted to off-axis movement for *pcd* and *reeler* mice.**

**(A-E)** Average instantaneous forward (x) velocity of FR paw during swing phase for *pcd* mice (purple), *reeler* mice (cyan) and size-matched controls (black). Line thickness represents increasing speed. **(B-F)** x-y position of four paws relative to the body center during swing. **(C-G)** y-excursion for front and hind paws, relative to body midline. **(D-H)** Average vertical (z) position of FR paw relative to ground during swing.

We next examined the horizontal (y) and vertical (z) movements of the paws (**Figure 3.6 B-D; F-H)**. *Pcd* mice exhibited a wider base of support than size-matched control mice ($F_{(15.51,1)}$=42.87, p<0 0.001, **Figure 3.6 B**), while in *reeler* mice that was not observed ($F_{(32.1,1)}$=0.03, p=0.87, **Figure 3.6 F**). However, there were subtle changes in side-to-side (y) paw trajectories for both *reeler* and *pcd* mice (*pcd*: $F_{(13.88,1)}$=20.64, p <0.001 and *reeler*: $F_{(28.3,1)}$=4.3, p < 0.05; **Figure 3.6 C-G**).

Further, analysis of the vertical (z) trajectories revealed significantly larger vertical displacement of both front and hind paws of *pcd* and *reeler* mice, across speeds (*pcd*:$F_{(66.84,1)}$=17.16, p <0 0.001 and *reeler*: $F_{(137.7,1)}$=13.1, p <0 0.001, **Figure 3.6 D-H; Figure 3.7 C-D**). The variability of this vertical displacement was not different in *pcd* mice ($F_{(81,1)}$=2.47, p = 0.12).

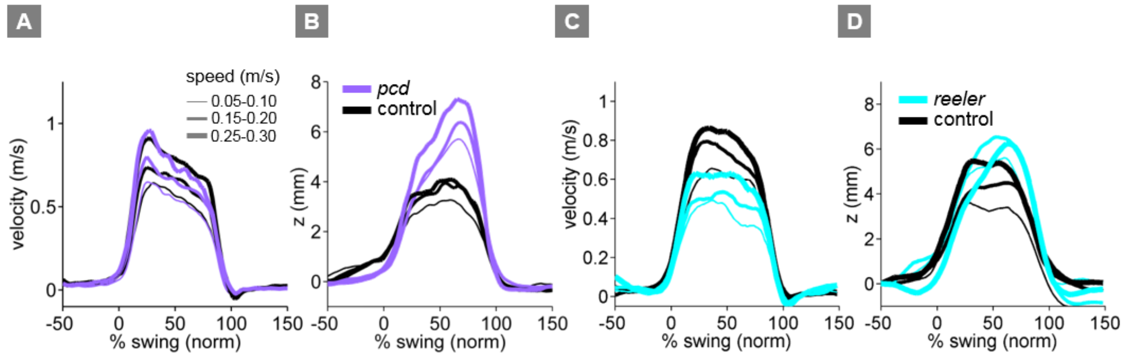

**Figure 3.7. 3D paw trajectories for *pcd* and *reeler* mice.**

**(A-C)** Hind right paw x-trajectories. **(B-D)** Hind right paw vertical (z) position relative to ground during swing. In *pcd* **(B)**, hind paws were lifted higher than forepaws, and their peak positions varied more steeply with speed in *pcd* mice($F_{(153.02,1)}$ = 5.64,p<.05).

Although, forward velocity of front paws in *reeler* mice was preserved, alteration in hind paws across all dimensions was observed. Lower peak velocity (**Figure 3.7 C**) and slight hyper-flexion (**Figure 3.7 D**) was revealed. In addition, *reeler* mice has been described with incapability in maintaining their hindquarters upright (Cendelin 2014).This observation is consistent with our data.  As it was previous described several brain regions are affected in *reeler* mice, while in *pcd* mice neurodegeneration was more specific to cerebellum and post-natal. Differences across *pcd* and *reeler* mice could be explained by the differences in the neurodegeneration process

Thus, despite the visibly ataxic walking pattern of *pcd* and *reeler* mice, the results of the mixed-effects linear models and the trajectory analyses indicate that the forward motion of the paws was remarkably preserved in *pcd* and *reeler* mice. Alterations in individual limb movements were restricted to off-axis (horizontal and vertical) trajectories.

### 3.3.2 Interlimb: Front-hind coordination is specifically impaired, while left-right coordination is preserved

Analyses of mouse locomotion that have focused on quantifying the kinds of basic stride parameters presented in **Figure 2.6** have previously failed to quantitatively capture gait ataxia in visibly ataxic mice (Cendelín, Voller et al. 2010). We reasoned that this could be because human observers are more sensitive to the patterns of movement across different parts of the body (Basso, Fisher et al. 2006). Therefore, we analyzed patterns of interlimb and whole body coordination in both control, *pcd* and *reeler* mice.

In our experiments, wildtype mice walked in a symmetrical trot pattern across speeds – each diagonal pair of limbs moved together and alternated with the other pair (**Figure 3.8 A**). According to the terminology of Hildebrand (1989), at slower speeds there was a tendency toward a ‘walking trot’ (front paws in a diagonal pair touch down just before hind paws and the paws are on the ground more than 50% of the time), while at faster speeds a ‘running trot’ was observed (diagonal paw pairs strike the ground near-simultaneously and paws are on the ground less than 50% of the time). There was no abrupt shift between these gait patterns – stance phases varied smoothly with walking speed and duty cycle (**Figure 3.8 A - C**) (Bellardita and Kiehn 2015) .We did not observe galloping or bounding even at the highest speeds (Bellardita and Kiehn 2015), probably because the mice freely initiated trials in our experiments, rather than being placed in the corridor by the experimenter at the start of each trial. For ease of quantification, and because of a lack of categorical gait boundaries in our data, we analyzed interlimb coordination in terms of phase values and support patterns rather than gait patterns.

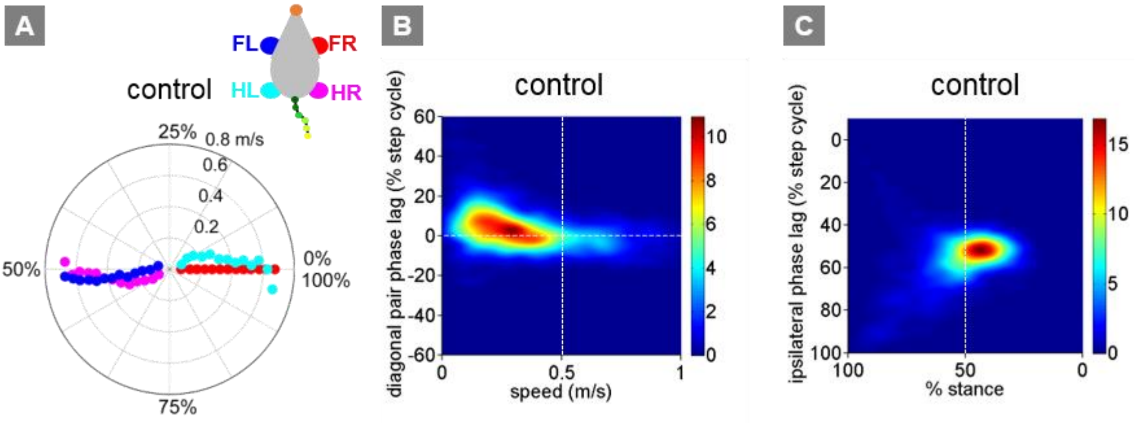

**Figure 3.8. Wildtype mice walked in a symmetrical trot pattern across speeds.**

**(A)** Polar plot indicating the phase of the step cycle in which each limb enters stance, aligned to stance onset of FR paw (red). Distance from the origin represents walking speed. Polar plot for size-matched control mice (N=11). **(B)** Smoothed probability density of diagonal (FL-HR) pair stance phase lags and speed obtained by kernel density estimation for all strides of size-matched controls (n = 3400, N = 11). Color code is estimated stride density. **(B)** Smoothed probability density of ipsilateral pair (FL-HL) stance phase lags and % stance duration for all strides of size-matched controls. Color code is estimated stride density.

The normal pattern of interlimb coordination was markedly disrupted in *pcd* and *reeler* mice, due to specific and consistent changes in the phase relationship between front and hind limbs (*pcd*: $F_{(77.07,1)}$=4.11, p<.05 and *reeler*: $F_{(142.6,1)}$=20.4, p<.001; **Figure 3.9 B,C ; Figure 3.9 D, E right**). Importantly, in marked contrast to the front-hind limb coupling, left-right alternation was maintained in *pcd* and *reeler* (*pcd:* $F_{(159,1)}$ =0.018, p=0.89 and *reeler:* $F_{(325.1,1)}$ =0.32, p=0.57; **Figure 3.9 B,C:** red vs. blue and cyan vs. magenta; **Figure 3.9 D,E left**). Thus, as a result of the de-synchronization of front and hind paw movements, the diagonal limbs no longer moved in phase with each other.

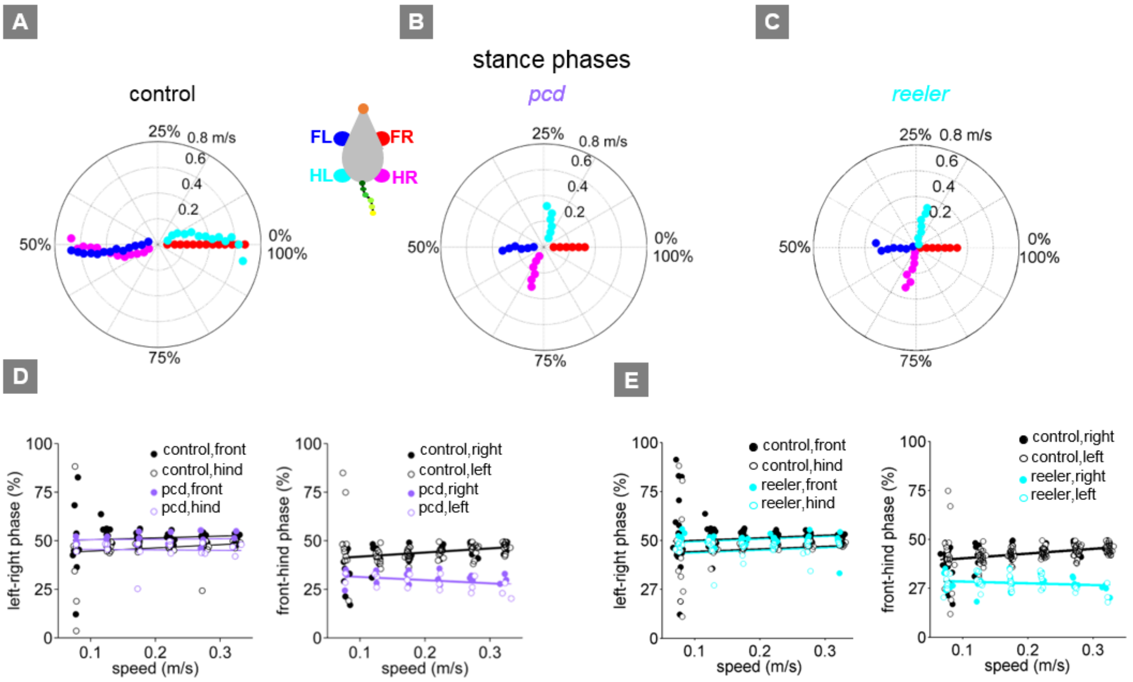

**Figure 3.9. Front-hind limb coordination is specifically impaired in *pcd* and *reeler* mice.**

**(A-C)** Polar plots indicating the phase of the step cycle in which each limb enters stance, aligned to stance onset of FR paw (red). Distance from the origin represents walking speed. **(A)** size-matched control mice (N=11). **(B)** *pcd* mice (N=3) and **(C)** *reeler* mice (N=7). **(D)** Left-right phase (left) and front-hind (right) phase for individual animals of *pcd* and size-matched controls. **(E)** Left-right phase (left) and front-hind (right) phase for individual animals of *reeler* and size-matched controls. Circles show average values for each animal. Lines show fit of linear-mixed effects model for each variable.

Support patterns, or the configuration of paws on the ground at any given time, vary systematically with walking speed (Gorska, Zmysłowski et al. 1998). Typically, wildtype mice had two diagonal paws on the ground at any given time (2-paw diagonal support, **Figure 3.10 A**), but this ranged from 3 paws on the ground during slow walking to 0 paw supports, or brief periods of flight, during running at higher speeds, due to changes in stance to swing phasing (**Figure 3.10 G**). *Pcd* and *reeler* mice spent more time with more paws on the ground (**Figure 3.10 B C**) (3-paw support *pcd*: $F_{(82,1)}$ =83.57, p<0.001 and *reeler*: $F_{(13.5,1)}$ =42,8, p<0.001; **Figure 3.10 D**). Moreover, while % double paw support was the same for *pcd* and size-matched control mice walking at comparable speeds (*pcd*: $F_{(167,1)=}$1.06, p=0.31 and *reeler*: $F_{(167,1)=}$3.27, p>0.05), the upper limit of *pcd* walking speeds coincided with the transition from positive to negative % double hind limb supports (**Figure 3.10 F**, see Materials and methods). Thus it appears that the walking speed of *pcd* mice is limited by the need to have at least one hind paw on the ground, for postural stability (Stolze, Klebe et al. 2002).

Despite their slower walking speeds and increased percent of time spent with more paws on the ground, *pcd* and *reeler* mice also showed an increase in unstable support configurations such as non-diagonal 2-paw support (**Figure 3.10 E**) (*pcd*:$F_{(46.78,1)}$ =7.76,p=0.01 and *reeler*: $F_{(74.1,1)}$=21.01,p<0.001), particularly at higher walking speeds (*pcd:* $F_{(67.62,1)}$ =115.82, p<0.001 and *reeler:* $F_{(72.3,1)}=39.4$, p<0.001). This increased instability indicates that *pcd* and *reeler* mice are not simply switching to a more stable gait pattern as a compensatory mechanism, but rather, are unable to properly time their front-hind limb movements to generate a stable, efficient gait. Further, the changes in interlimb phasing for *pcd* mice were consistent – front-hind phasing was not more variable in *pcd* ($F_{(164,1)}=2.88$, p=.091), and in fact left-right phasing was even less variable ($F_{(166,1)}=9.70$, p=.0021).

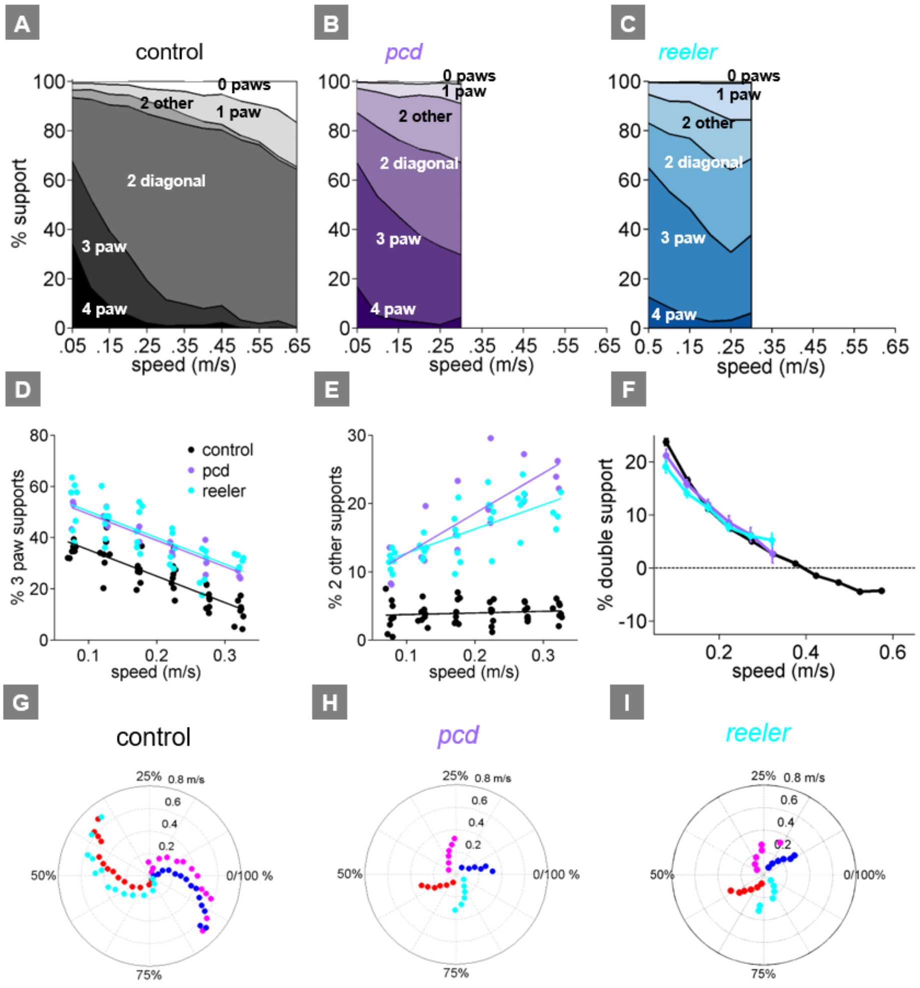

**Figure 3.10. *Pcd* and *reeler* mice spent more time with more paws on the ground.**

**(A-C)** Support patterns: Area plot of average paw support types as % of stride cycle, across speeds for **(A)** size-matched controls, **(B)** *pcd* mice and **(C)** *reeler* mice. **(D)** 3 paw and **(E)** 2-paw other supports for each animal (circles). Lines show fit of linear-mixed effects model. **(F)** Average ± sem percent double support for hind paws of *pcd*, *reeler* and size-matched controls. **(G-H)** Stance to swing phases: Polar plots of stance to swing phasing aligned to front right paw for **(G)** controls, **(H)** *pcd* mice and **(I)** *reeler* mice**.**

Taken together, these results reveal that temporal measures of interlimb coordination during overground locomotion were altered both in *pcd* and *reeler* mice.

### 3.3.3 Whole-body movement: *Pcd* and *reeler* the side-to-side (y) tail and nose movement

Movements not just of the limbs, but of the entire body need to be coordinated during locomotion. In order to characterize whole-body locomotor coordination in both control, *pcd* and *reeler* mice, we analyzed their head and tail movements while they walked freely across the corridor (**Figure 3.11**).

In control mice, lateral movements of the nose and tail were small (**Figure 3.11 A-H in black**). In striking contrast, the tail of *pcd* and *reeler* mice exhibited large side-to-side oscillations during the locomotor cycle (**Figure 3.11 A-H** in purple and cyan) (compared to size-matched controls: tail in *pcd* $F_{(401.02,1)}$ = 5.55,p < 0.05 and *reeler* $F_{(136,1)}$=15.01, p<0.05). While the nose side-to-side oscillation was also larger for *pcd* mice, the *reeler* showed less amplitude (nose: *pcd* $F_{(53.61,1)}$ = 4.89,p <0.05 and *reeler* $F_{(139.48,1)}$=0.35, p=0.82, **Figure 3.11 D, H**).

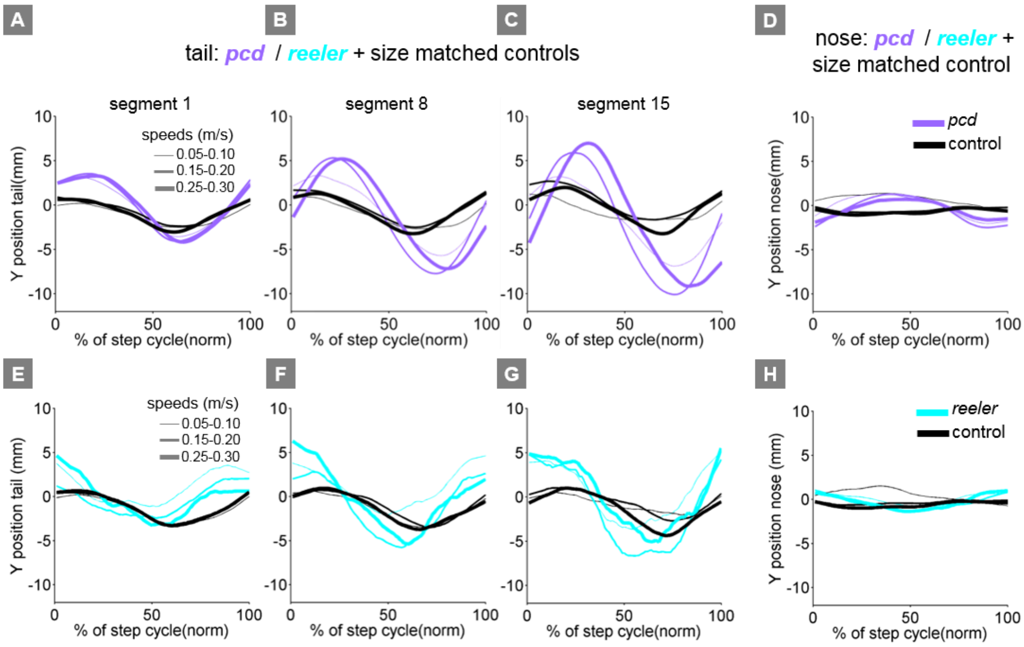

**Figure 3.11. Nose and tail movements across speed bins for controls, *pcd* and *reeler* mice.**

**(A-C)** Average interpolated (y) trajectory of tail segment 1, 8, 15, respectively for wild type mice aligned with stance onset of the hind right paw. **(D)** Average interpolated (y) trajectory of nose for wild type mice aligned with stance onset of the front right paw. **(E-H)** Same as **(A-D)** but for *reeler* mice.

To visualize and quantify impairments in whole-body coordination, we compared vertical (z) trajectories for each body part, normalized to 100% of the stride cycle. **Figure 3.12** summarizes the trajectories of individual body parts as well as interlimb and whole body coordination of speed- and size-matched control, *pcd* and *reeler* mice. During locomotion in control mice, the movement of different parts of the body is synchronized, and vertical nose and tail movements are relatively small (**Figure 3.11 A**). In *pcd* and *reeler*, however, spatial and temporal coordination across the body is dramatically impaired (**Figure 3.11 B, C**). This lack of correlational structure reflects the failure of *pcd* and *reeler* mice to synchronize the movements of different parts of the body.

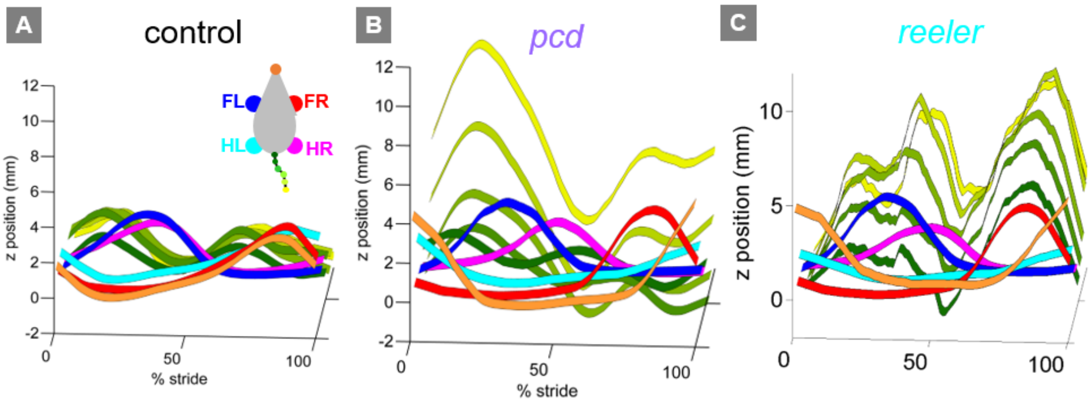

**Figure 3.12. Visualization of impaired whole-body coordination in *pcd* and *reeler* mice.**

**(A)** Ribbon plots showing average vertical (z) trajectories for nose, paw and select tail (2, 5, 8, 11, 14) segments for **(A)** size-matched control (N=11), **(B)** *pcd* (N=3) and **(C)** *reeler* (N=11) mice walking at 0.20 - 0.25 m/s. Data are presented relative to 100% of the stride cycle of the FR paw (x-axis). Nose and paw trajectories are z position relative to floor; tail is z relative to floor with mean vertical position of the of base of the tail subtracted for clarity.

Taken together, these results suggest that while the forward motion of individual paws is largely spared, ataxic *pcd* and *reeler* mice have specific deficits in coordinating movement in three dimensions across joints, limbs, and body.

## 3.4 Discussion

Establishing appropriate, sensitive, and specific behavioral measures is an essential first step for investigating relationships between brain and behavior (Clark, Freifeld et al. 2013, Anderson and Perona 2014). Although deficits in locomotor coordination are readily visible to the human eye, identifying the specific, quantitative features of gait ataxia has been more difficult (Leblond, L'Espérance et al. 2003, Cendelín, Voller et al. 2010, Dorman, Krug et al. 2014). Here we used the custom-built LocoMouse system to analyze locomotor kinematics and coordination in freely walking mice. The high spatiotemporal resolution and throughput of this system provides the most comprehensive description of locomotor kinematics in freely walking mice to-date and allowed us to develop a novel analysis framework for mouse locomotion that revealed fundamental features of gait ataxia. Our main findings are (1) Basic paw stride parameters can be predicted solely based on walking speed and body size. (2) This relationship holds in visibly ataxic *pcd* and *reeler* (particular front paws) mutants, indicating that changes in these stride parameters in ataxic mice do not reflect fundamental features of ataxia. (3) While the forward motion of the paws is spared in *pcd* and *reeler*, coordination across joints, limbs, and the body is selectively impaired. (4) The nose and tail of *pcd* mice and the tail in *reeler* oscillate as a passive consequence of forward hind limb motion. Taken together, this pattern of deficits reveals that gait ataxia in *pcd* and *reeler* mice involves specific impairments in locomotor coordination across joints, limbs, and body parts.

### A quantitative framework for locomotor coordination reveals fundamental features of mouse gait ataxia

The statistical models we developed based on a library of data from wildtype mice (**Figure 2.6, Table 1**) accurately predicted the forward paw motion of ataxic *pcd* mice and front paw motion of *reeler* mice (**Figure 3.5**). This indicates that observed differences in basic stride parameters were a secondary consequence of differences in body size and walking speed. Further, the forward motion of individual paws was indistinguishable from that of size- and speed-matched controls, down to the level of detailed paw trajectories. This important result highlights that failure to account for differences in walking speed and body size when comparing data across mice and strides can lead to nonspecific effects being misinterpreted as symptoms of ataxia (Koopmans, Deumens et al. 2007, Cendelín, Voller et al. 2010, Batka, Brown et al. 2014). Moreover, it is likely that by focusing primarily on the forward movement of individual paws, many existing analyses fail to capture the fundamental features of ataxia.

While differences in forward paw motion could be fully accounted for by differences in walking speed and body size, in contrast, off-axis paw trajectories, interlimb, and whole-body coordination revealed specific patterns of impairment in *pcd* and *reeler* (**Figure 3.8 – 3.12**). Differences in off-axis movements (**Figure 3.5**) suggest that *pcd* and *reeler* mice, like human cerebellar patients, are unable to coordinate movements across joints within the limb to perform normal strides in 3D (Bastian, Martin et al. 1996, Earhart and Bastian 2001). Further, *pcd* and *reeler* mice exhibited impaired spatial and temporal coordination of movements across the four limbs, nose, and tail. Interestingly, while front-hind paw coupling was dramatically altered in *pcd* and *reeler*, left-right alternation was preserved entirely, consistent with the idea that such alternation is generated within the spinal cord itself (Crone, Zhong et al. 2009, Kiehn 2011, Dougherty, Zagoraiou et al. 2013). Finally, the large, oscillatory nose and tail movements observed in *pcd* and large amplitude in *reeler* were not just random, but were successfully modeled as a failure to predict and compensate for the passive consequences of forward motion of the hind limbs.

Given the diversity of cerebellar phenotypes, it is expected that the specific features of gait ataxia will vary across mouse models (Lalonde and Strazielle, 2007). Strikingly, that was not the case when quantification on locomotor deficits in *reeler* mice was made. The neurodegeneration in *reeler* mice was not specific to the cerebellum region as it was in *pcd* mice. In addition, *pcd* mice neurodegeneration was pot-natal. Although *reeler* mice were visibly more ataxic than *pcd* mice, they share similar and specific core features. In *reeler* mice hind paws were completely altered at the level of the individual limb parameters. However, front paws are remarkably preserved, the rest of impairments are restricted to multi-joint, interlimb, and whole-body coordination like in *pcd* mice*.* The consistency of this features across cerebellar mutant mice strength our idea on cerebellar contributions to coordinated movement.

# 4

# Optogenetic manipulation of distinct deep cerebellar nuclei differentially effects coordinated locomotion in mice

**4.1. Introduction**
**4.2. Methods**
**4.3. Results**
  **4.3.1. Targeting the deep cerebellar nuclei with spatial and temporal precision: from medial to lateral region**
  **4.3.2. Only medial and interposed nucleus show perturbation in overground during optogenetic manipulation. Lateral nucleus shows no effects**
    4.3.2.1. Using LocoMouse system to quantify specifically motor impairments during deep cerebellar nuclei manipulation. Speed and stance onset by trial
    4.3.2.2. Distinguishing and quantifying locomotor parameters that are specific to each deep cerebellar nucleus
**4.4. Discussion**

**Manuscript in preparation:**
Ana S. Machado, Dominique Pritchett, and Megan R. Carey, Optogenetic manipulation of distinct deep cerebellar nuclei differentially effects coordinated locomotion in mice

Author contributions
ASM, and MRC, Conception and design, Analysis and interpretation of behavioral data, ASM, Data acquisition. DP and ASM, Electrophysiological recordings and Analysis of recordings.

## 4.1 Introduction

Smooth and efficient walking requires the coordination of movement across different parts of the body (Orlovsky, Deliagina et al. 1999, Morton and Bastian 2007, Veloz, Zhou et al. 2015). The cerebellum plays an important role in this process. It's well established that cerebellum has a medial-to-lateral functional organization (Jansen and Brodal 1940, Voogd and Glickstein 1998). Cerebellum can be divided into distinct functional zones (medial, intermediate and lateral) based on its afferent and efferent projections (Jansen and Brodal 1940, Voogd and Glickstein 1998). However, it is still not well understood how the specific neural circuit within this zones contributes to whole-body coordination during walk (Morton and Bastian 2007).

Lesion studies of the deep cerebellar nuclei, in cats and monkeys, provided an important information about the cerebellum functional organization (Chambers and Sprague 1955, Udo, Matsukawa et al. 1979, Morton and Bastian 2007). The different outputs are responsible for different aspects of motor control (Chambers and Sprague 1955). Lesions in the different deep cerebellar nuclei showed that the most basic function; such as posture and balance, are controlled by the medial nucleus, while the fine-tuning of limbs movement and motor planning is progressively controlled by the interposed and lateral nuclei (Sprague and Chambers 1953, Chambers and Sprague 1955, Udo, Matsukawa et al. 1979, Thach, Goodkin et al. 1992, Morton and Bastian 2007).

Most of what we know from cerebellum functional organization comes from these lesions studies. However, they are poorly spatial defined and lack of specificity(Morton and Bastian 2007). Tools to manipulate the activity of selective neural subtypes have been growing tremendously (Luo, Callaway et al. 2008). Optogenetic tools combine genetics and optical methods to selectively stimulate or silence neural subtypes with a high temporal precision and reversibility (Zhang, Aravanis et al. 2007). However, analyses of mouse gait have typically lacked detail about the precision and timing of limb movements. These parameters are required to perform a complete analysis of motor coordination. Therefore, a quantitative behavior analysis with high temporal resolution and precision is crucial (Brooks and Dunnett 2009, Anderson and Perona 2014).

Here I combine the Locomouse system with optogenic tools to perform acute manipulation across the three different nuclei. Our goal is to understand how different output regions of the cerebellum differentially contribute to locomotor coordination.

## 4.2 Methods

### Animals

Experiments were conducted with homozygous L7-Cre mice crossed with an animal homozygous for ChR2-eYFP. A total of 19 L7CreChR2YFP mice (11 males; 8 females; 19-28g, 12–18 weeks old) were housed in institutional standard cages (3 animals per cage) on a reversed 12-hr light/12-hr dark cycle with *ad libitum* access to water and food. All procedures were reviewed and performed in accordance with the Champalimaud Centre for the Unknown Ethics Committee guidelines, and approved by the Portuguese Direcção Geral de Veterinária (Ref. No. 0421/000/000/2015).

### Surgical procedure

Animals are anesthetized with isoflurane/O2/N2O (1.5%/30%/68.5%) and secured in the stereotaxic frame for surgery. A circular craniotomy was performed with a dental drill with the following coordinates for each group: Medial: AP=-6,24 ML=0,72; Interposed A: AP=-6,00 ML=1,56; Lateral: AP=5,80 ML=2,00. Fiber optic cannulas (MFC_100/125-0.22_3.75mm_SM3_FLT) were fixed with dental cement and were positioned vertically. Following surgery, we administer Dolorex analgesia through IP injection, and the mice are checked at least daily for the entire experiment. The mice rest in their cage for 3 days before the experiments.

### *In vivo* electrophysiology

Optrodes were built with a fiber optic cannula (MFC_100/125-0.22_3.00mm_ZF1.25_FLT) glued at ~300um up to the electrode (Quartz-insulated tungsten tetrodes from Thomas Recording -tip type A, impedances between 1-3 MOhm) and vertically inserted into craniotomies. L7CreChR2YFP were head-fixed and allowed to move in place freely on a spinning disk. Recordings were performed with an Intan digital amplifier/head stage with the Open Epys digital acquisition board. A TTL pulse was generated to delivered brief pulses of light through a patch cord coupled to the optrode. The blue Light came from a 473 nm laser (473 nm DPSS Laser System; Output: > 200mW; Stability < 1%) and TTL pulse was controlled with custom written software using LabView. Recordings were monitored online using a custom Bonsai software interface.  All recordings were digitized from the wideband signal (0.1 Hz - 10kHz, sampled at 30kHz), and sorted offline using the KlustaKwik suite for unit clustering and custom Matlab code for unit analysis.

## Histology

Subsets of animals at the end of behavioral experiments were perfused to confirm ChR2-YFP expression and optical fiber placement. Mice were anesthetized with ketamine/xylazine and perfused with 4% paraformaldehyde (P6148, Sigma-Aldrich) and brain removed. Brain was stored in 4% paraformaldehyde overnight and kept in cryoprotectant solution (PBS in 30% sucrose). Coronal sections (50 µm) were cut in a cryostat (CM3050S, Leica, Germany), mounted on glass slides with mowiol mounting medium (81381, Sigma-Aldrich, St. Louis, MO). Each section was stained with nissl and anti-calbindin. Scanning images for YFP and transmitted light were acquired with an upright fluorescence microscope (Axio Imager M2, Zeiss, Oberkochen, Germany) equipped with a digital CCD camera (AxioCam MRm, Zeiss) with a 10X objective.

## Data collection on LocoMouse

Data collection was performed in three groups of animals: **(a)** medial nucleus (N=6 $n_{total}$=6162 $n_{non\text{-}stim}$=5416, $n_{stim}$=746 n: #strides); **(b)** interposed A nucleus (N=7 $n_{total}$=6921 $n_{non\text{-}stim}$=5880, $n_{stim}$=1041); **(c)** lateral nucleus (N=6 $n_{total}$=4404 $n_{non\text{-}stim}$=3681, $n_{stim}$=723).

Mice were handled by the experimenter and allowed to acclimate in the LocoMouse setup before data collection. Animals were weighed before each session. Mice walked freely between two dark boxes on either end of the glass corridor.  No food or water restriction or reward was used. For a more detail description of the LocoMouse setup please read (Methods Chapter 2).

*Optogenetics experiments.*

Two days before stimulation protocol the mice make several passages on the LocoMouse corridor with a Mono Fiberoptic Patchcord implanted to get used to it. After the habituation, we perform one session per mouse for 7 consecutive days. Each session consists of 20 – 30 corridor passages. We used a blue laser (473 nm DPSS Laser System; Output: > 200mW; Stability < 1%) and a Mono Fiberoptic Patchcord (MFP_100/110/900-0.22_1.5m_FC-CM3) to delivery brief pulses of light. The stimulation protocol consisted of 30% trials with light stimulation and 70% no Light stimulation, randomly interleaved during the session. TTL pulse was controlled with custom written software using LabView. Light stimulation consisted in 50Hz (frequency) with intensities 2 – 5 mW during 300 – 900 ms. An infrared LED was synchronized with the stimulation protocol and detection time was collected. The Laser power was calibrated using a powermeter (PM130D, Thorlabs) before and after each animal session. The optical fiber patchord was screwed to the M3 implanted connector with the animal freely moving, in the beginning of each experiment.

### Data acquisition

Movies were collected at 400 frames per second with a spatial resolution of 1440x250 pixels. Acquisition software was written in Labview and uses 2 National Instruments boards (PCIe 1433 and BNC 2120) to record and save the movies, in real time. The tracking algorithm and data analysis software were written in Matlab (Mathworks) and performed offline. The LocoMouse Tracker code used in this paper can be downloaded from GitHub (https://github.com/careylab/LocoMouse).

### Data analysis

The stride cycles of individual paws were automatically broken down into swing and stance phases based on the first derivative of the paw position trajectories. Individual strides were defined from stance onset to subsequent stance onset. For each stride, average *walking speed* was calculated by dividing the forward motion of the body center during that stride by the stride duration. All data was sorted into speed bins (0.05 m/s bin width) in a stridewise manner, with a minimum stride count criterion of 5 strides per bin, per animal. Individual limb movements and interlimb coordination were calculated as follows:

### Trial analysis

Velocity (x,y): Instantaneous trail velocity relative to nose by trial (m/s)
Trial duration: Total trial duration (s)
Stance onset: All the stance onset in time of FR paw during trial (s)

### Individual limb parameter

Cadence: Inverse of stride duration (s-1)
Swing velocity: x displacement of single limb during swing phase divided by swing duration (m/a).
Stride length: x displacement from touchdown to touchdown of single limb (mm).
Stance duration: Time in milliseconds that foot is on the ground during stride (ms).
Trajectories: Trajectories were aligned to swing onset and resampled to 100 equidistant points using linear interpolation. Interpolated trajectories were then binned by speed and the average trajectory was computed for each individual animal and smoothed with a Savitzky-Golay first-order filter with a 3-point window size (% norm).
Interlimb and whole-body coordination parameters
Stance phase: relative timing of limb touchdowns to stride cycle of reference paw. Calculated as: (stance time−stance timereference paw)/stride duration (%).

Supports: support types were categorized by number of paws on ground expressed as a percentage of the total stride duration for each stride. Paw support categories are four, three, two diagonals, two other (homolateral and homologous), one, and zero (%).

**Statistical analyses**

Statistical analyses were done in Matlab and R. For all comparisons, models were selected by comparing equations specifying additive fixed-effects terms with those specifying n-way interaction terms using a likelihood-ratio test and inspection of statistical significance of included terms. Depending on the comparison, fixed-effects terms included a subset of the following variables: speed, genotype and paw. All models were random-intercepts models with subject as a random covariate. Unless otherwise indicated, results are reported as conditional F tests with Satterthwaite degrees of freedom correction.

## 4.3 Results

### 4.3.1 Targeting the deep cerebellar nuclei with spatial and temporal precision: from medial to lateral region

To examine the medial to lateral functional organization of the cerebellum (**Figure 4.1 A**) in freely walking mice, we used L7-Cre mice crossed with ChR2-eYFP mice to express the light-sensitive ion channel channelrhodorpsin-2 (ChR2) in Purkinje cells. An optical fiber was implanted above each nucleus and closed to the Purkinje cell terminals. The fibers were placed only in the right side of the cerebellum. The careful selection of coordinates, the lower power intensity from fiber tip and the cannula small numeric aperture (NA=0.22), allowed to minimize light dispersion to nearby regions (light wavelength of 473 nm, NA=0.2, light power from fiber tip = ~2mW, depth of 2 mm and Irradiance=0.06 mW/mm$^2$) (**Figure4.1 B**). Each animal had one fiber implanted in one nucleus. Mice received blue light pulses in randomly alternated trials. Light onset was mostly trigged during ongoing movements. (**Figure 4.1 C**). Histological analysis performed at the end of the experimental protocol confirmed the expression of ChR2-YFP and fiber localization. ChR2-YFP was selectively expressed in Purkinje cells (Pkj cells) throughout the cerebellum and was also visible in the axons projecting to the deep cerebellar nuclei (DCN) (**Figure 4.1 D**). In vivo, single-unit optrode recordings from DCN in response to activation of ChR2 in Pkj cells showed that Pkj cells strongly inhibit DCN neurons during laser stimulation. Similar effects were observed across the different cerebellar nuclei (medial, interposed A (intA) and lateral **Figure 4.1 E-G**). Recordings were performed in awake mice.

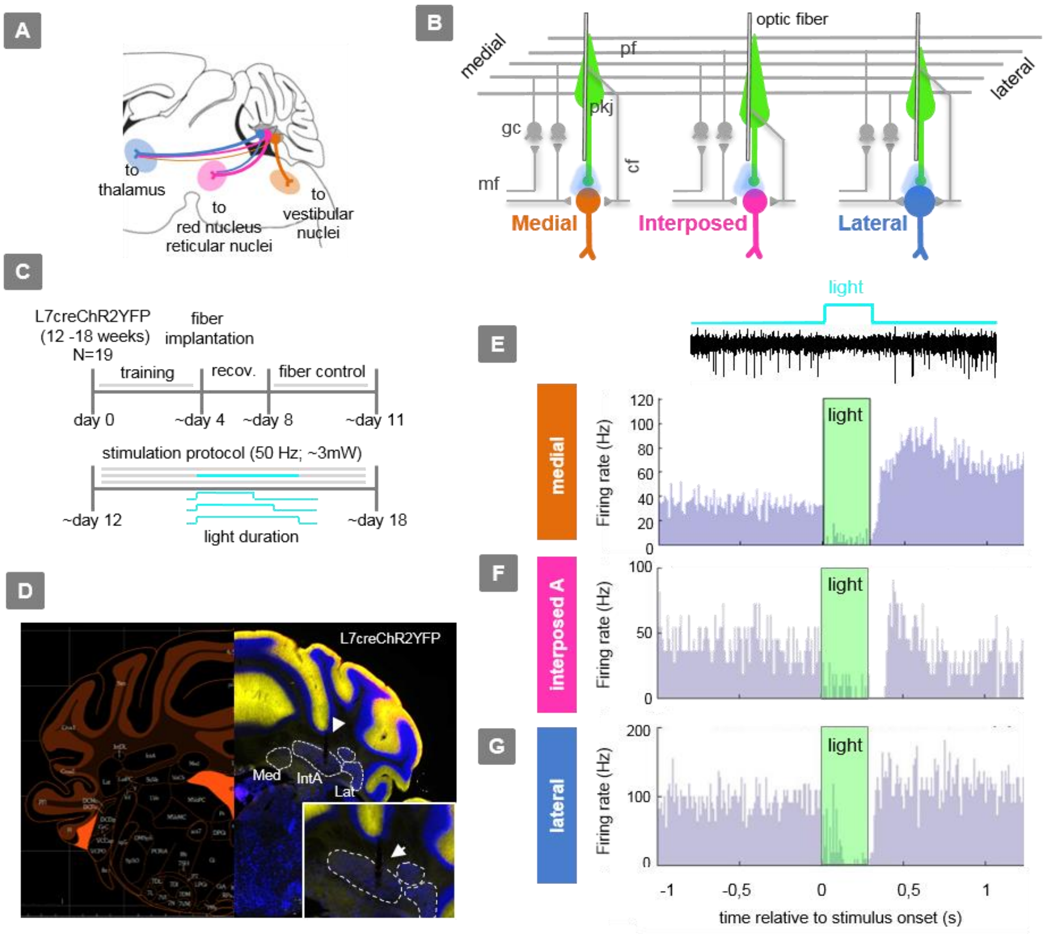

**Figure 4.1 Using L7CreChR2YFP mice to target the deep cerebellar nuclei: from medial to lateral region**

**(A)** Schematic illustration of deep cerebellar nuclei projections. **(B)** Medial to lateral inputs and outputs of cerebellum with the optogenetic approach. Purkinje cells (green), expressing ChR2-YFP through transgenic mice L7CreChR2YFP, were photoactivated with blue light delivered through an implanted optical fiber. The tip of the optical fiber was located above each deep cerebellar nucleus and close to Pkj cells axons. The cerebellum circuit is repeated across medial to lateral region and it's composed by mf: mossy fibers; gc: granule cells; pf: parallel fibers; pkj: purkinje cells; cf: climbing fibers. **(C)** Experimental protocol scheme. A total of 19 transgenic mice (L7creChR2YFP) with 12-18 weeks old were used. The mice were divided into three groups: a) medial nucleus N=6; b) interposed nucleus N=7; c) lateral nucleus N=6. In each group a single optical fiber was implanted on the right side of the cerebellum. The photostimulation protocol consisted of stimulated (stim, blue) and non-stimulated (nostim, grey) trials. Every session started with a block of non-stim trials. Stimulated and non-stimulated trials were randomly alternated with proportion of 3/10. **(D)** Photomicrographs of coronal cerebellar section showing the fiber location and the expression off ChR2eYFP in Pkj cells. The section was stained with Nissl for neurons visualization. The tip of the optical fiber is located above the interposed A nucleus. **(E-G)** *In vivo* recordings from deep cerebellar nuclei cells in response to 300ms light delivered to purkinje cells axons (activation of ChR2) in awake mice. Cyan boxes are the Laser pulse duration. Top row: Single extracellular traces in response to blue laser; bottom row: peri-stimulus time histograms for each nucleus. **(E)** *In vivo* recordings from the medial nucleus, **(F)** interposed A nucleus and **(G)** lateral nucleus.

### 4.3.2 Only medial and interposed nucleus show perturbation in overground during optogenetic manipulation. Lateral nucleus shows no effects

#### 4.3.2.1 Quantifying motor impairments during deep cerebellar nuclei manipulation. Speed and stance onset by trial

To quantify locomotor impairments during optogenetic manipulation in each DCN, we used the LocoMouse system (described in **Chapter 2** and **Chapter 4**). Acute disruption of neural activity in medial and interposed nuclei immediately perturbed ongoing locomotion (p<0.001, paired t-test). In contrast, similar manipulation of Purkinje cell inputs to the lateral nucleus had no observable effect on ongoing locomotor behavior. (**Figure 4.2 A, C**). Differences across deep cerebellar nuclei were revealed when velocity in y axis was analyzed. Mice with medial nucleus manipulation did not exhibited a side-to-side nose oscillation. On the contrary, IntA perturbation showed an increased side-to-side nose (y) oscillation. Mice shifted to the right (ipsi) side immediately after stimulation onset and to the left side after stimulation offset, suggesting a perturbation on the right side of the body (**Figure 4.2 B**). Across animals, the average timing (~100 ms) relative to laser onset and speed perturbation in x indicates that medial and intA optogenetic manipulation led to locomotion perturbation (**Figure 4.2 D**).

The step frequency by trial was also analyzed. Histograms of stance onset (time) across all trials are plotted in **Figure 4.2 G, H** and **I**. Activation of Pkj cells terminals above the medial and intA nucleus led to a drastically reduction of the number of stance onset. Differences across deep cerebellar nuclei were revealed when light duration was increased. Only in the medial nucleus perturbation, the lower number of stance onsets was maintained throughout the light period, suggesting that the mice become nearly immobile during that time (**Figure 4.2 G, H**). These perturbations, both in medial and intA, led to longer trial durations when compared to non-stim trials. No significant differences were observed during activation of Pkj cells axons in the lateral nucleus (**Figure 4.2 I**).

#### 4.3.2.2 Distinguishing and quantifying locomotor parameters that are specific to each deep cerebellar nucleus

To identify the different locomotor aspects that are specifically related to the manipulation of each nucleus, we used the framework analysis for whole-body coordination described in the previous **chapter 2** and **3**. Activation of Pkj cells terminals in the medial and intA nucleus result in visibly locomotor impairments when mice walked on the LocoMouse setup.

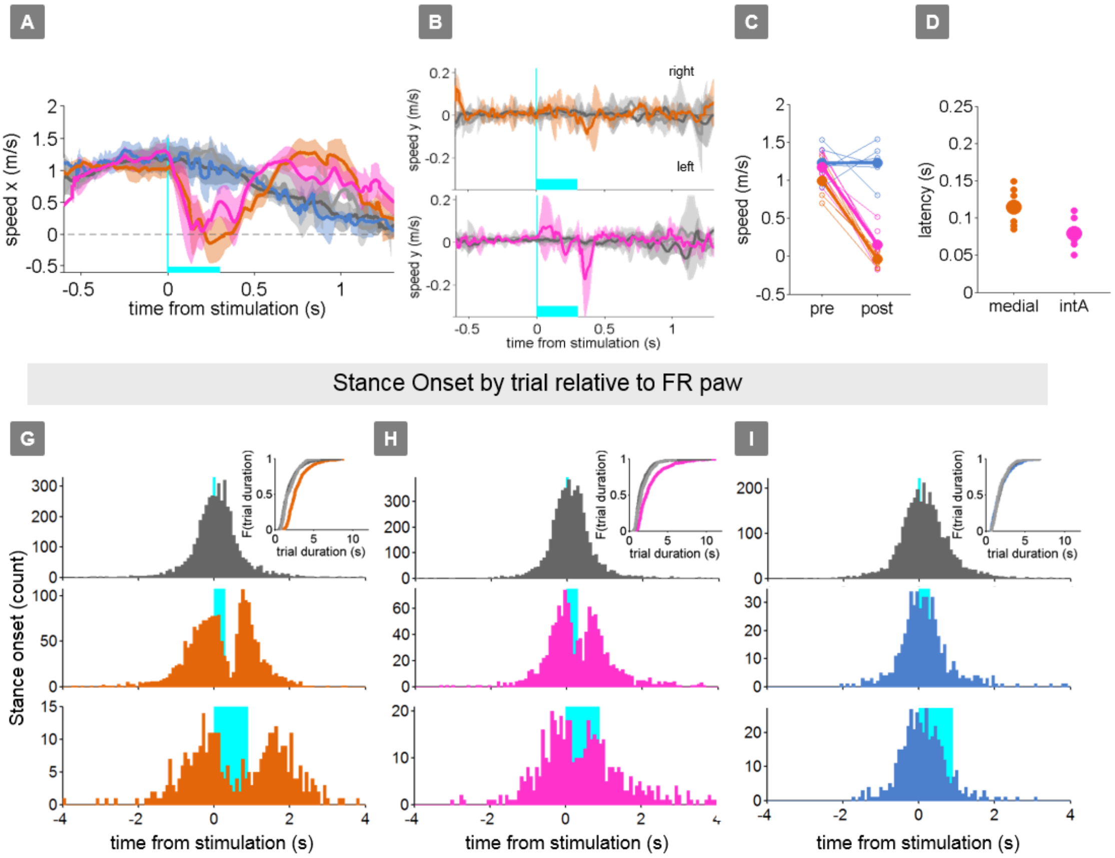

**Figure 4.2. Optogenetic manipulation of medial and interposed nuclei reduce ongoing movement during overground locomotion**

**(A)** Average trial nose speed (in x) relative to stimulation onset for each nucleus and controls. **(B)** Average trial nose speed (in y) relative to stimulation onset for medial (top), intA (bottom) and controls. Cyan boxes are the laser duration (300 ms). The lines with shadows represent the mean ± SEM. Stimulated trials are represented with different colors (medial-orange, intA–magenta; lateral-blue). Control trials with grey (fiber control – light grey; Non-stim trials - dark grey). **(C)** Average speed in pre and post stimulation intervals for individual mice (thin lines are color coded according to each nucleus) and the mean values for each populationn. **(D)** Delay response to speed (in x) perturbation for individual mice and mean population. **(G-I)** Stance onset histograms by trial for each nucleus, relative to FR paw. Top row: non-stimulated trials (dark grey), bottom row: stimulated trials at different laser durations (300ms, 900ms) for each nucleus (colors). All trials were aligned to the stimulation onset. Small plot (top right): cumulative distribution of trial duration for each nucleus. **(G)** Medial nucleus: non-stimulated trials (dark grey), stimulated trials (orange). **(H)** IntA nucleus: non-stimulated trials (dark grey), stimulated trials (magenta). **(I)** lateral nucleus: non-stimulated trials (dark grey), stimulated trials (blue).

Comparing the basic stride parameters of stimulated trials with non-stim trials, relative to front right paw, revealed that the strides, overall, were quite different during photostimulation (**Figure 4.3 D, G, J** and **E, H, L**). Impairments resulting from medial nucleus manipulation were more severe than the interposed A nucleus. Stride lengths were shorter (medial $F_{(63,1)}$ = 31,1, p <0.0001; intA $F_{(74,1)}$ = 12,2, p < 0.01 **Figure 4.3 D, E**, orange and magenta shadows), even when changes in walking speed (**Figure 4.3 A, B**) were taken into account. Swing and stance durations were also altered (medial $F_{(63,1)}$ = 43,1, p <0.0001; intA $F_{(74,1)}$ = 13,2, p < 0.01 **Figure 4.3 J, L, N, M** orange and magenta shadows).

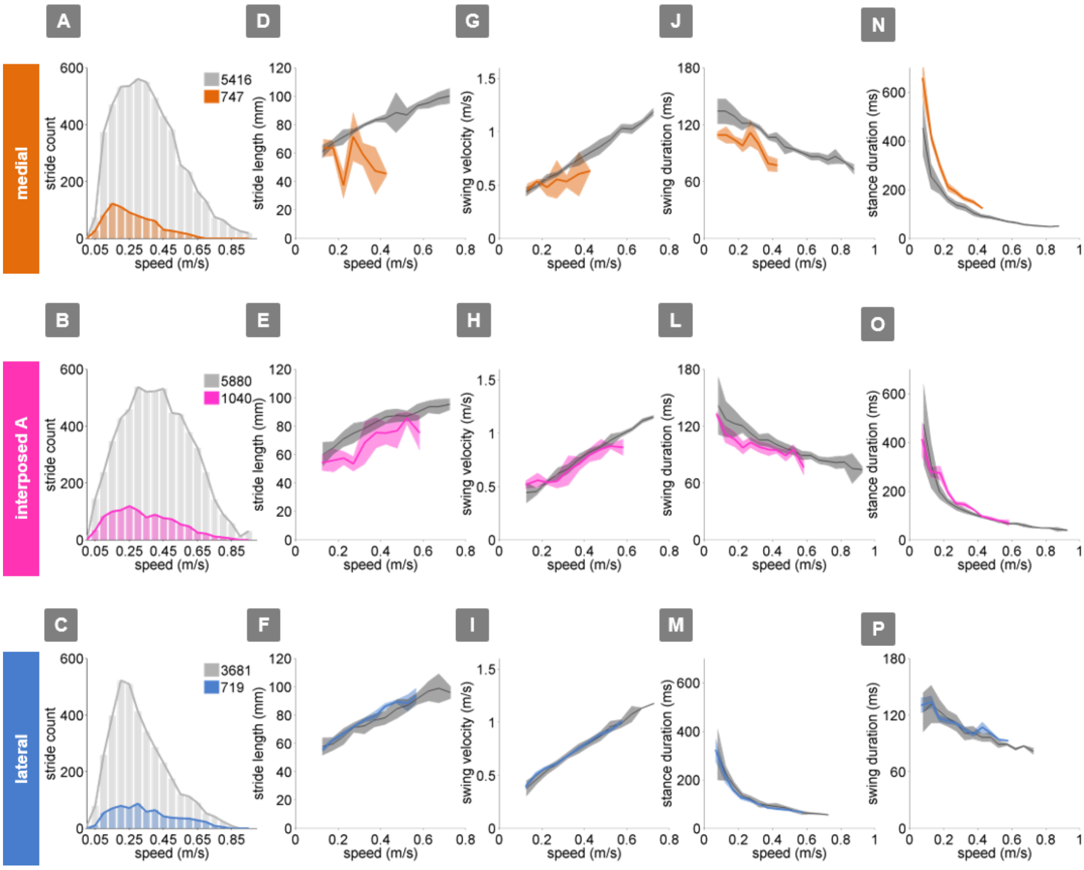

**Figure 4.3. Basic stride parameters are severely impaired during optogenetic manipulation in medial nucleus. Interposed stimulation showed a mild perturbation.**

**(A-B)** Stride count histogram binned by average walking speed for each group. Strides are divided into speed bins of 0.05 m/s. Stimulated strides are plotted with different colors. **(A)** medial- orange, **(B)** intA–magenta; **(C)** lateral-blue). Strides with no stimulation are plotted as grey. **(D-M)** Basic stride parameters: **(D-F)** Stride length (mm), **(G-I)** swing velocity (m/s) and **(J-M)** swing duration (ms) and **(N-P)** stance duration (ms) by walking speed for the FR paw. The median and ± 25th, 75th percentiles are represented for each group of animals.

Impairments on the swing velocity were more visible in the medial nucleus manipulation (medial $F_{(62,1)} = 23,1$, $p < 0.0001$; intA $F_{(74,1)} = 9,2$, $p < 0.05$ **Figure 4.3 G**). No significant differences on basic stride parameters across all four paws were observed during activation of Pkj cells axons in the lateral nucleus (lateral ex: stride length $F_{(72,1)} = 0.03$, $p = 0.9$, **Figure 4.3 F, I, M**).

Since DCN manipulations were performed in the right side of the cerebellum and each side of the cerebellum controls the ipsilateral side of the body, we asked to what extent the altered strides parameters where different across the left and right body side. Basic stride parameters for all paws are plotted in **Figure 4.4 A, B**. Acute disruption of neural activity in medial nucleus led to severe differences in both spatial and temporal parameters across all four paws (medial $F_{(62,4)} = 27,3$, $p < 0.0001$, **Figure 4.4 A, B – orange shadow**). Stride length did not vary across walking speed (**Figure 4.4 A – orange shadow**). In contrast, optogenetic

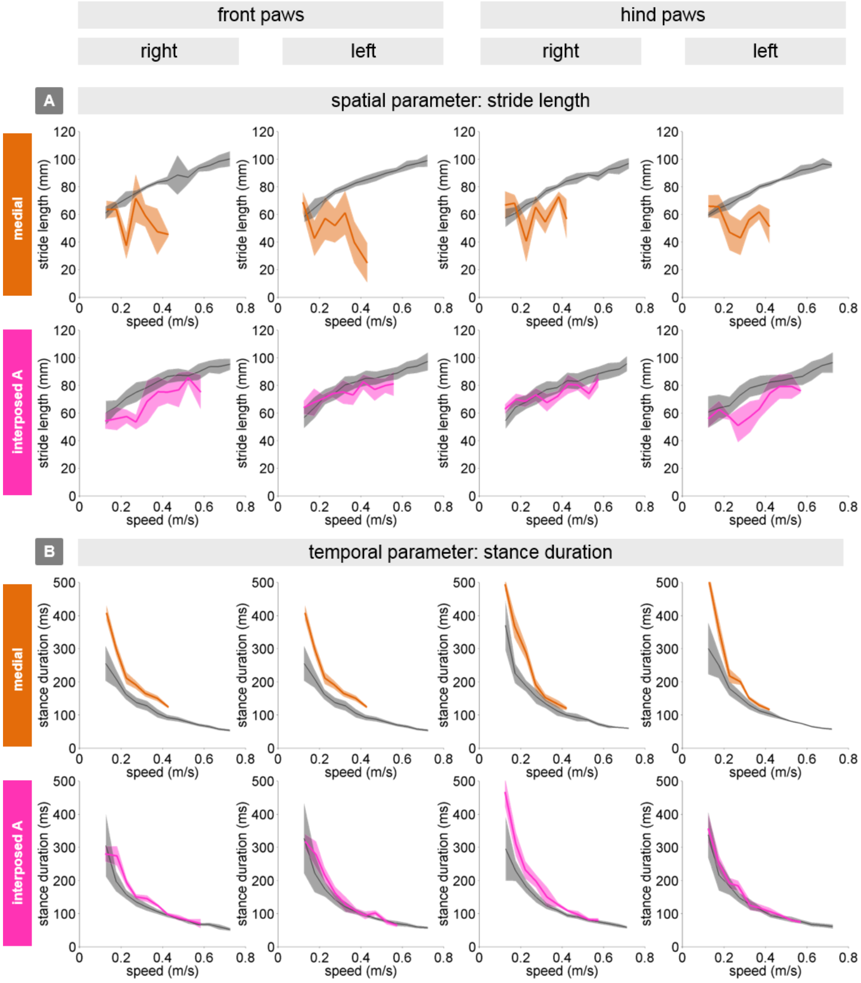

**Figure 4.4. All four paws are severely impaired during optogenetic manipulation in medial nucleus. Only the right side is affected in the Interposed A nucleus.**

**(A)** Basic stride parameters: Stride length (mm) across walking speed for all four paws. Medial nucleus perturbation in orange shadows, interposed A nucleus in magent shadows and non-stim strides in grey shadow. **(B)** Stance duration (ms) across walking speed for all four paws. Medial nucleus perturbation in orange shadows, interposed A nucleus in magent shadows. The median and ± 25th, 75th percentiles are represented for each group of animals.

manipulation of the interposed A nucleus result in shorter stride lengths of front right paw and diagonal pair (hind left paw, due to the symmetrical trot) and shorter stance duration for the right (ipsi) side paws (both front and hind, intA stance duration $F_{(74,2)}$ = 10,3, $p < 0.01$**Figure 4.4 A, B – magenta shadow**). Basic stride parameters, of all four paws, are severely impaired during the medial nucleus manipulation. Interposed nucleus manipulation showed mild differences towards right (ipsi) side paws.

### Optogenetic manipulation of medial and interposed A nuclei induce impairments in 3D paw trajectories

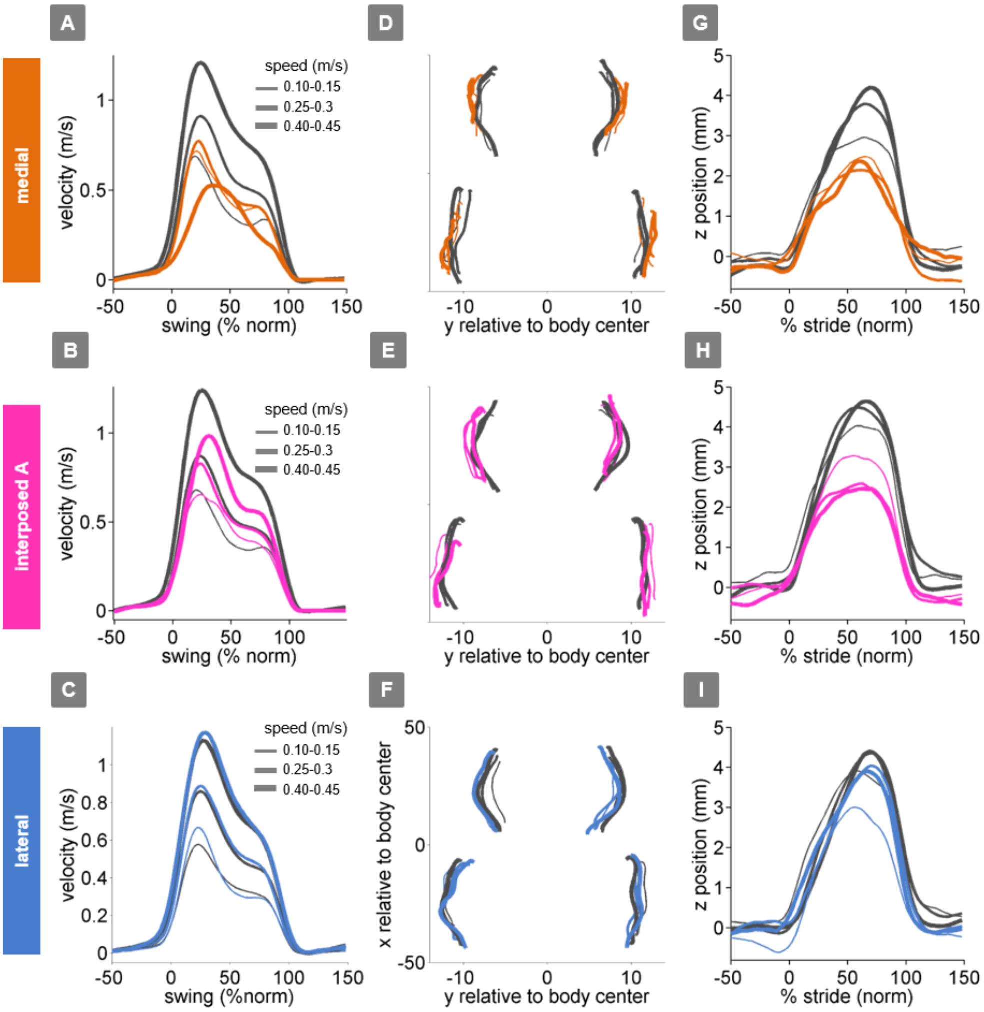

**Figure 4.5. Optogenetic manipulation of medial and interposed A nuclei induce impairments in 3D paw trajectories.**

**(A-C)** Average instantaneous x velocity of FR paw during swing phase for **(A)** Medial nucleus manipulation (orange) **(B)** IntA nucleus manipulation (magenta) **(C)** Lateral nucleus manipulation (blue) and non-stim strides (dark grey). Line thickness represents increasing speed. **(D-F)** Average x-y position of four paws relative to body center during swing. **(J-M)** Average vertical (z) position for FR paw relative to ground during swing.

Next we analysed the continuous 3D paw trajectories for both stimulated and non-stim strides (**Figure 4.5**). In the non-stim stride (grey lines) the instantaneous forward paw velocity profile changes with speed. Paw velocity peaked early during swing and decelerated before stance onset across walking speeds. In vertical (z) and side-to-side (y) movement there is no significant differences between the different speeds (**Figure 4.5 – grey lines**).

Impairments on trajectories across the 3 dimension (x, y and z) where observed for medial and intA nuclei manipulation (**Figure 4.5 – orange and magenta lines**). Instantaneous forward paw velocity profile was clear altered. Paw velocity peak was slower during medial and intA nuclei perturbation. Besides the perturbation on peak flexion, the time to peak was also impaired, suggesting an abnormal interjoint coordination of the limb (medial $F_{(62,1)}$ = 31,3, p <0.0001; intA $F_{(74,1)}$ = 14,3, p <0.01, **Figure 4.5 A, B – orange and magenta lines**). Horizontal (y) movement analysis showed paw trajectory perturbation on side-to-side (y) movement during swing phase, indicating an abnormal direction of the limb movement (medial $F_{(62,1)}$ = 16,3, p <0.01; intA $F_{(74,1)}$ = 8,3, p <0.05, **Figure 4.5 D, F – orange and magenta lines**). Stimulated trials did not exhibit a wider base of support (**Figure 4.5 D, F – orange and magenta lines**). Further, analysis of the vertical (z) trajectories revealed significantly shorter vertical displacement during medial and intA nuclei manipulation across speeds (medial $F_{(62,1)}$ = 28,3, p <0.0001; intA $F_{(73,1)}$ = 21,3, p <0.01; **Figure 4.5 G, H – orange and magenta lines**). No significant differences on 3D paw trajectories were observed during activation of Pkj cells axons in the lateral nucleus (lateral: $F_{(71,1)}$ =0.02, p =0.8; **Figure 4.5 C, F, I**). Impairments on trajectories across the 3 dimension (x, y and z) where observed for medial and intA nuclei manipulation (**Figure 4.5 – orange and magenta lines**). Instantaneous forward paw velocity profile was clear altered. Paw velocity peak was slower during medial and intA nuclei perturbation. Besides the perturbation on peak flexion, the time to peak was also impaired, suggesting an abnormal interjoint coordination of the limb (medial $F_{(62,1)}$ = 31,3, p <0.0001; intA $F_{(74,1)}$ = 14,3, p <0.01, **Figure 4.5 A, B – orange and magenta lines**). Horizontal (y) movement analysis showed paw trajectory perturbation on side-to-side (y) movement during swing phase, indicating an abnormal direction of the limb movement (medial $F_{(62,1)}$ = 16,3, p <0.01; intA $F_{(74,1)}$ = 8,3, p <0.05, **Figure 4.5 D, F – orange and magenta lines**). Stimulated trials did not exhibit a wider base of support (**Figure 4.5 D, F – orange and magenta lines**). Further, analysis of the vertical (z) trajectories revealed significantly shorter vertical displacement during medial and intA nuclei manipulation across speeds (medial $F_{(62,1)}$ = 28,3, p <0.0001; intA $F_{(73,1)}$ = 21,3, p <0.01; **Figure 4.5 G, H – orange and magenta lines**). No significant differences on 3D paw trajectories were observed during activation of Pkj cells axons in the lateral nucleus (lateral: $F_{(71,1)}$ =0.02, p =0.8; **Figure 4.5 C, F, I**).

We next investigate if differences in 3D paw trajectories were present in all four paws. For that, analysis on paw peak velocity were performed across speed, paws and individual animals (**Figure 4.6**). Once again, acute disruption of neural activity in medial nucleus led to strong differences in all four paws, while in the intA nucleus impairments were mainly restricted to the front right paw (medial $F_{(62,4)}$ = 26,7, p <0.001; intA $F_{(74,1)}$ = 15,3, p <0.01; **Figure 4.6 A-B orange, magenta dots**). No significant differences were observed in the lateral nucleus (lateral $F_{(72,4)}$ =1.1, p =0.51, **Figure 4.6 C**).

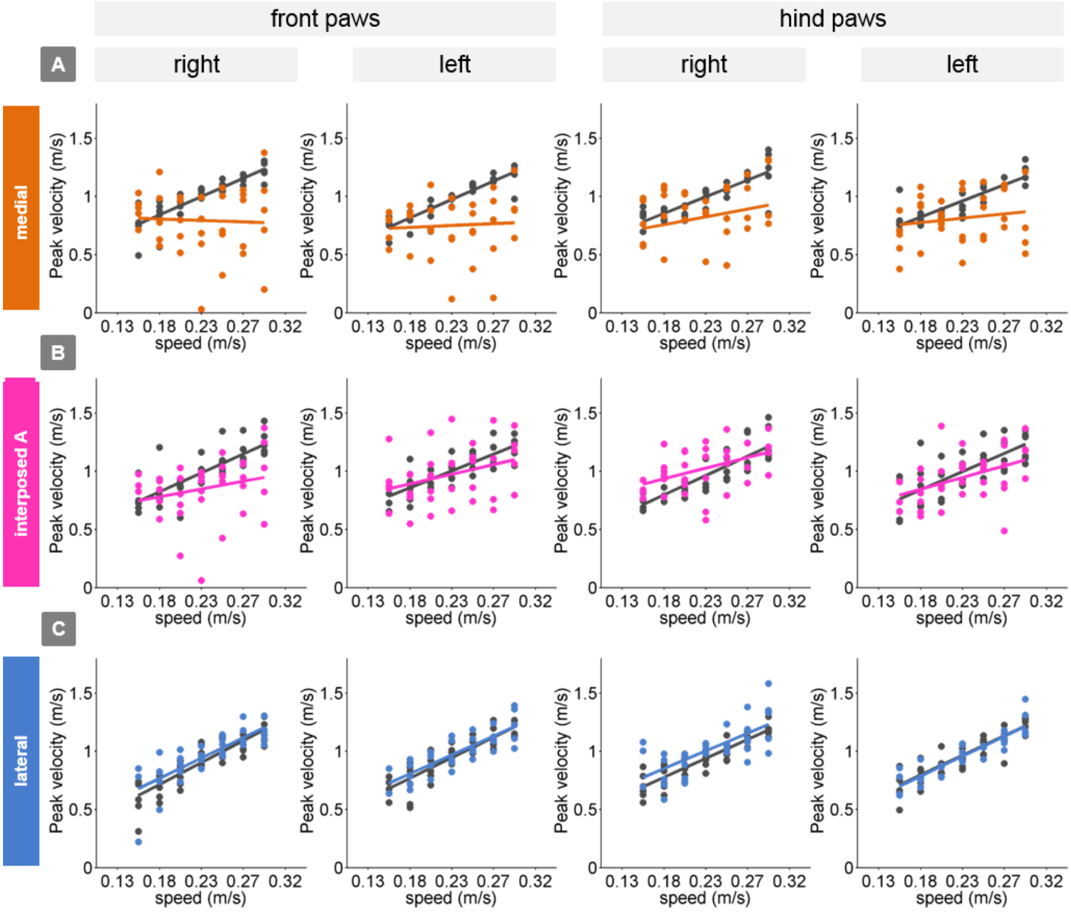

**Figure 4.6 Instantaneous peak velocity reveals specific differences across paws and nucleus, during photostimulation.**

**(A-C)** Peak velocity during swing phase across walking speed for each nucleus and each paw (color stimulated strides, grey non-stim strides). **(A)** Medial nucleus. **(B)** Interposed A nucleus **(C)** Lateral nucleus. Circles show average values for each animal. Thick lines represent linear fits to the data

Taken together, both basic stride parameters and 3D trajectories findings revealed that the medial nucleus perturbation led to the most severe impairments, both in spatial and temporal parameters, across all four paws. Slower walking speed was also observed. In contrast, perturbation on interposed A nucleus, led to middle and restricted differences in the right side of the body. Differences on the temporal parameters (stance duration) were restricted to the right side of the body (front and hind paws), while differences on spatial parameter (stride length) where specific to the front right paw.

### Interlimb coordination

Wildtype mice walked in a symmetrical trot pattern across speeds – each diagonal pair of limbs moved together and alternated with the other pair, represented as a polar plot in **Figure 4.7 A, B, C – grey markers.** In the polar plot the phase of the step cycle in which each limb enters stance were plotted. Each paw is aligned to the onset of FL paw (triangle marker).

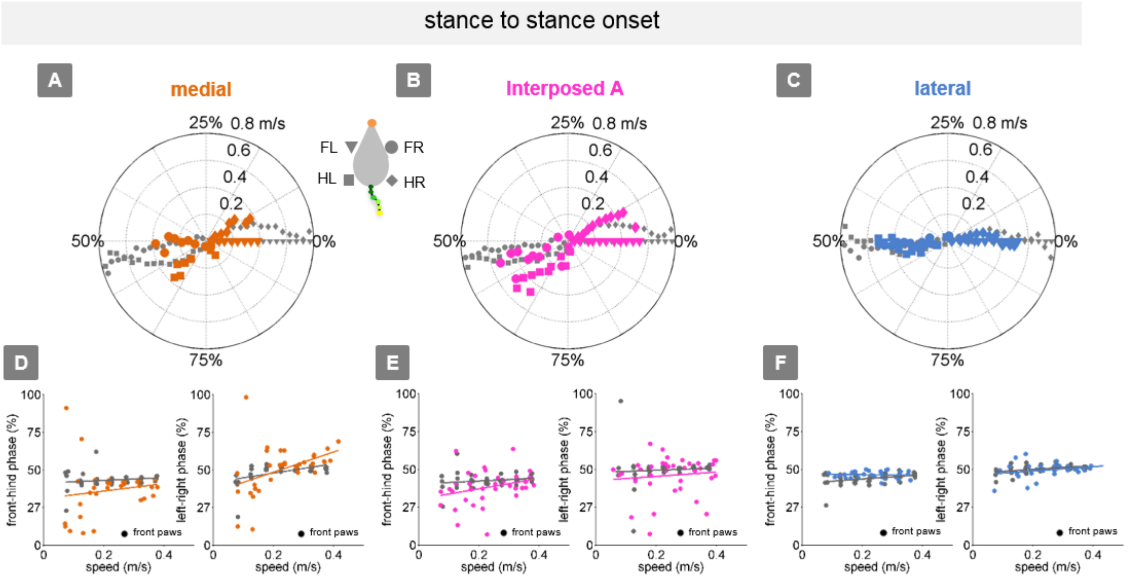

**Figure 4.7 Interlimb coordination between stimulated strides and no stimulated trials.**

**(A-C)** Polar plot indicating the phase of the step cycle in which each limb enters stance, aligned to stance onset of FR paw (circle marker). Distances from the origin represent walking speed, average values are plotted. **(G)** The FR paw is represented as a circle marker, FL- triangle, HR – diamond and HL – square marker. **(A-C)** Polar plots for deep cerebellar manipulation mice (colors) overlaid on top of non-stim strides (grey), respectively. **(D-F)** Left-right phase (right) and Left-right phase (left) for deep cerebellar manipulation mice (colors) non-stim strides (grey), respectively, across speeds. Circles show average values for each animal. Lines show fit of linear-mixed effects model for each variable.

Distances from the origin represent walking speeds. The FR paw was represented as solid circle, the FL paw as triangle, HR paw as diamond marker and HL paw as solid square. In our experiments, no other gait patterns besides the symmetrical trot pattern was observed in the range of speeds analyzed (0.05-0.8 m/s) (**Figure 4.7 A, B, C – grey markers**), as previously described in chapter 3. An increase variability and slightly differences in both left-right phase and front-hind phase were observed across animals in both medial and intA nuclei manipulation when compared with non-stim trials (**Figure 4.7 A, B – orange, magenta markers)**. However, those differences were not statistical significant.  The left-right phases of individual animals are plotted in **Figure 4.7 D, E - right** (medial $F_{(70,1)}$ = 2.09, p = 0.2; intA $F_{(76,1)}$ = 0.06, p = 0.8), while front-hind phases are represented in **Figure 4.7 D, E - left**. (medial $F_{(67,1)}$ = 0.3, p = 0.6; intA $F_{(74,1)}$ = 1.5, p = 0.23) No alteration was observed in the lateral nucleus (LR: lateral $F_{(72,1)}$ = 0.3, p = 0.5; FH: lateral $F_{(74,1)}$ = 0.1, p = 0.73  **Figure 4.7 C, F**).

### Mice with medial and interposed A nucleus optogenetic manipulation spent more time with more paws on the ground

Support patterns, or the configuration of paws on the ground at any given time, vary systematically with walking speed (Górska et al., 1999) (**Figure 4.8 A**). Typically, wildtype mice

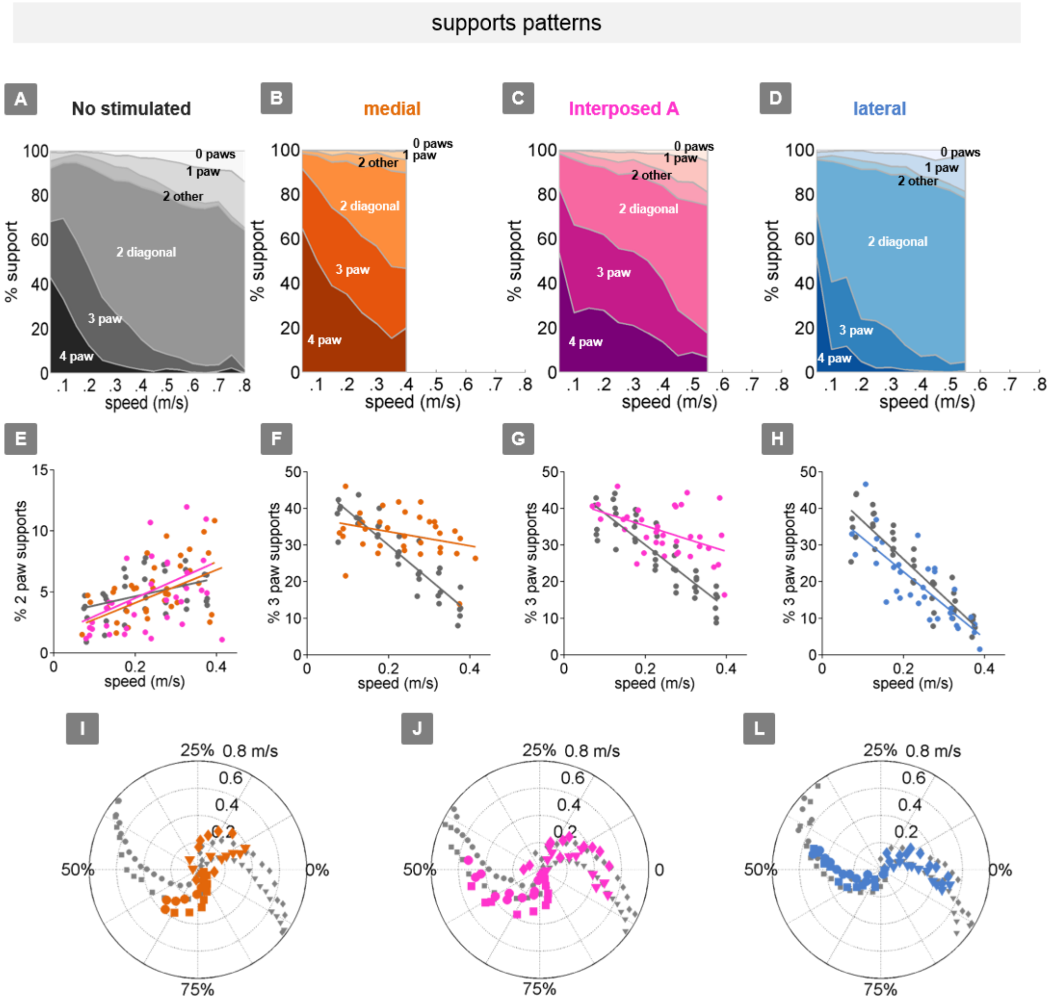

**Figure 4.8 Mice with medial and interposed A nucleus photostimulation spent more time with more paws on the ground. No significant differences were found in interlimb coordination.**

**(A-D)** Support patterns. Area plot of average paw support types as a percentage (%) of stride cycle, across speeds for **(A)** Non-stim strides, **(B)** Medial nucleus manipulation (orange) **(C)** IntA nucleus manipulation (magenta) **(D)** Lateral nucleus manipulation (blue). **(E)** 2-paw other supports for each animal (circles) **(F-G)** Percentage of 3 paws support for each animal (circles) - average values across speeds. Lines show fit of linear-mixed effects model. **(I-J)** Stance to swing phases: Polar plots of stance to swing phasing aligned to front right paw for **(I)** medial nucleus manipulation, **(H)** interposed A nucleus manipulation and **(I)** lateral nucleus manipulation**.**

had two diagonal paws on the ground at any given time, but this ranged from 3 paws on the ground during slow walking to 0 paw supports, or brief periods of flight, during running at higher speeds, due to changes in stance to swing phasing (**Figure 4.8 I-J**). Mice with medial and intA nucleus manipulation spent more time with more paws on the ground (**Figure 4.8 B, F, C, G**). The increase in percentage of 3 and 4 paws support was more drastic during medial nucleus perturbation (medial $F_{(63,1)}$ = 43,7, p <0.0001; intA $F_{(72,1)}$ =21,2, p < 0.0001**, Figure 4.8 B, F**). In addition, the non-diagonal 2-paw support (unstable support configuration) was not altered (medial $F_{(63,1)}$ = 1.9, p = 0.2; intA $F_{(73,1)}$ =1.6, p =0.2**, Figure 4.8 E)**. Thus, it appears that activation of Pkj cells terminals in the medial and intA nucleus led to a

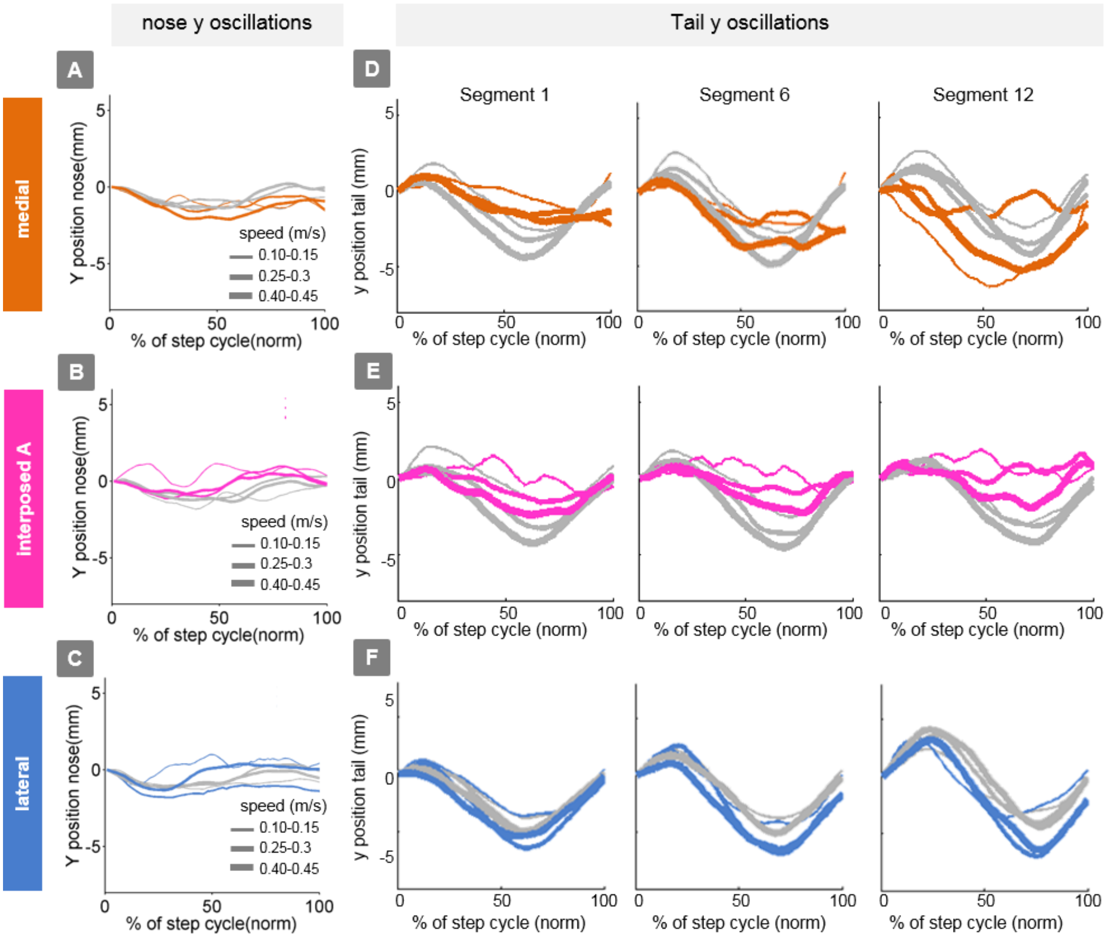

**Figure 4.9. Nose and tail movements across speed bins for medial, int A and lateral nuclei optogenetic manipulation.**

**(A-C)** Average interpolated (y) trajectory of nose aligned with stance onset of the front right paw for **(A)** medial nucleus perturbation **(B)** interposed A nucleus perturbation **(C)** lateral nucleus perturbation. **(D-F)** Average interpolated (y) trajectory of tail segment 1, 6, 12 aligned with stance onset of the hind right paw, respectively for **(D)** medial nucleus perturbation **(E)** interposed A nucleus perturbation **(F)** lateral nucleus perturbation.

more stable support configuration, which could be explained by postural instability. No significant differences were observed during activation of Pkj cells axons in the lateral nucleus (lateral $F_{(74,1)}$ = 0.8, p = 0.4, **Figure 4.8 D, H, L**).

Movements not just of the limbs, but of the entire body need to be coordinated during locomotion. In order to characterize whole-body locomotor movement in both stimulated strides and non-stim strides, we analyzed their head and tail movements while mice walked freely across the corridor. No significant differences were found in the side-to-side (y) nose movements during acute disruption of neural activity in medial and interposed nuclei (medial $F_{(63,1)}$ = 1.4, p = 0.24; intA $F_{(73,1)}$ =0.9, p =0.32, **Figure 4.9 A-C**). In contrast, impairments were restricted to tail oscillations during medial and interposed nuclei manipulation (**Figure 4.9 D-E**). The amplitude of the tail oscillation much was smaller in stimulated trials than non-stim trials, suggesting a restriction of the tail movement (medial $F_{(63,1)}$ = 13,4, p <0.001; intA $F_{(73,1)}$ =16,1, p <0.001, **Figure 4.9 C, F**).

Taken together, these findings indicate that the perturbation of each cerebellar nuclei result in different motor impairments, suggesting that the different nuclei are responsible for different locomotor aspects, consistent with previous studies.

## 4.4 Discussion

In this study, we combined optogenetic tools and quantitative behavioral analysis to explore how different output regions of the cerebellum differentially contribute to locomotor coordination. The combination of these tools provides a powerful system to understand mouse locomotion. It is now possible to establish relationship between, acute changes in neural activity of individual cell type and specific motor output in freely walking mice.

Our results with acute manipulation are broadly consistent with previous anatomical and lesion studies (Chambers and Sprague 1955, Udo, Matsukawa et al. 1979, Morton and Bastian 2007). They also suggest a medial-to-lateral functional organization of cerebellar outputs. We demonstrated that **(a)** acute disruption of neural activity in medial nucleus led to severe impairments across the whole body. **(b)** Perturbation during optogentic manipulation of the interposed A nucleus were restricted to the right side of the body (ipsilateral to the fiber implementation) and in particular to front right limb. **(c)** No motor alteration was observed during lateral nucleus manipulation on overground locomotion.

The LocoMouse system allowed to differentiate and describe in great detail specific motor perturbation that resulted from acute manipulation of each nucleus. In the medial nucleus manipulation mice reduce forward velocity and become nearly immobile throughout period of light stimulation. Walking speed during photostimulation was much slower. Gait parameters in all four paws were severely impaired both in the spatial and temporal aspects. In addition, gait parameters did not vary (in proportion) with increasing walking speeds. Mice drastically increased the number of paws on the ground during locomotion. These findings could be explained by postures and balance instability where whole body parts must be affected.

During Interposed nucleus manipulation mice drastically reduce speed at the stimulus onset. However, they still maintained the ability to walk. Analysis on side-to-side (y) movement revealed that mice shifted to the right (ipsi) side immediately after stimulation onset, suggesting a perturbation on the right side of the body. Mild impairments on basic stride parameters (spatial and temporal) and paw trajectories were revealed. Once again, those impairments were restricted to the right side of the body, in particular to the front right limb. These findings indicates that interposed A nucleus is more involved in the ipsilateral limb motor control (deficits on the stride length of hind left paw are due to the symmetrical trot).

Finally, the lateral nucleus manipulation did not show any alteration during overgound locomotion, suggesting that lateral nucleus is not required during ongoing movements or in simple behaviors such as walking in a straight line.

# 5

# LocoMouse is a sensitive tool to assess detailed motor function in spinal cord mutant mice

**5.1 Introduction**
**5.2 Methods**
**5.3 Results**
  - **5.3.1 Using LocoMouse to reveal specific motor impairments in spinal cord mutant mice**
  - **5.3.2 Kinematic parameters of a single limb:** Stride length is impaired
  - **5.3.3 3D paw trajectories:** Side to side (y) and vertical (z) movement are perturbed during swing phase
  - **5.3.4 Interlimb:** Gait and support patterns are preserved during overground locomotion
  - **5.3.5 Nose and tail oscillation across speed bins and tail segments**: Impairments are restricted to tail segments

**5.4 Discussion**

**Manuscript in preparation:**

Alexandra I. Rosa*, Ana S. Machado*, Sara Ferreira, Domingos Henrique**, Megan R. Carey**, Cell-fate decisions mediated by Notch signaling during spinal cord embryonic development affect motor performance of individual limbs and tail in adulthood.

**Author contributions**

*AIR and ASM Co-first authors. **DH and MRC Co-last authors. AIR, ASM, DH and MRC, Conception and design, Analysis and interpretation of data, Drafting or revising the article. AIR and ASM, data collection. SF, Sample preparation

## 5.1 Introduction

The quantitative framework for whole-body coordination (LocoMouse system) revealed specific impairments that are associated with ataxic mutant mice during overground locomotion (described in **chapter 2** and **3**). Thus, the combination of high temporal-spatial resolution with precise quantitative analysis is fundamental to reveal specific motor impairements (Brooks and Dunnett 2009, Anderson and Perona 2014, Veloz, Zhou et al. 2015). Although, the LocoMouse system revealed in great detail locomotor impairments in cerebellum mutant mice, it's not known if it's reproducible to other regions of the nervous system (Machado, Darmohray et al. 2015). The next question is: Can LocoMouse identify and differentiate locomotor parameters that are associated with perturbations in other locomotor circuits? Are those parameters specific of spinal cord mutation? To investigate the robustness and specificity of the LocoMouse system, spinal cord mutant mice were used.

During spinal cord development, the Notch signaling pathway is required for cell diversity (Peng, Yajima et al. 2007). In Mice, there are several genes coding for Notch ligands, some of them are the 3 Delta ligands, *Delta1*, *Delta3* and *Delta4* (also known as *Dll1*, Dll3 and *Dll4*) (Louvi and Artavanis-Tsakonas 2006). During the development of spinal cord V2 domain, *Dll1* and *Dll4* ligands cooperate to generate cell diversity (Rocha, Lopes et al. 2009, Ramos, Rocha et al. 2010). V2a and V2b Interneurons (INs) are generated in this domain. Simultaneous deletion of one copy of *Dll1* and two copies of *Dll4* result into an increase of V2a INs and a decrease in V2b INs.

Mice normally use trotting at fasts speeds. Transgenic mouse model in which the V2a interneurons have been ablated showed transition to a galloping as speed increases. Left–right limb coordination is alterted at fasts speeds (Crone 2008, Crone, Zhong et al. 2009, Azim, Jiang et al. 2014). Although no apparent locomotor aleration in mice with deletion in *Dll*1/2 were visible by eye observation, we used the LocoMouse (Machado, Darmohray *et al*., 2015) system to quantify specifically putative impairments in locomotion. Here we show that deleting two *Dll4* copies or one *Dll1* copy and two *Dll4* copies results in individual limb and tail motor deficits while interlimb coordination was preserved, no alteration in gait pattern was observed even at fasts speeds. We also correlated these alterations with histology analysis of adult spinal cords.

## 5.2 Methods

### Ethics Statement

Animal experiments were approved by the Animal Ethics Committee of IMM (AEC_027_2010_DH_Rdt_general_IMM) and were conducted according to National and European Regulations.

### Mouse housing and breeding

All animals were fed *ad-libitum* and housed in SPF facilities.

The *Nestin-Cre* strain (Tronche, Kellendonk et al. 1999) was a kind gift from Rüdiger Klein (Max Planck Institute, Munich, Germany). Floxed *Dll1* (Hozumi, Negishi et al. 2004) and floxed *Dll4 (Koch, Fiorini et al. 2008)* mice were kindly provided by Julian Lewis (Cancer Research UK, London, UK).

Mice carrying either the conditional floxed *Dll1* allele (*Dll1*f/f) or the floxed *Dll4* allele (*Dll4*f/f) were crossed with *Nestin-Cre* mice and the *Dll1*f/+*Nestin-Cre* or *Dll4*f/+*Nestin-Cre* progeny was identified by PCR. *Dll4*f/+*Nestin-Cre* mice were crossed with *Dll4*f/f mice to produce litters containing conditional single knockout mice (*Dll4*f/f*Nestin-Cre*) and littermate controls. While *Dll4*f/f*Nestin-Cre* mice are viable and fertile, *Dll1* conditional deletion is embryonically fatal.

The *Dll1* and *Dll4* mice were intercrossed to obtain double mutant animals with different allelic dosages and sibling controls.

### Spinal cord collection and preparation for immunofluorescence

Briefly, adult spinal cords were collected in cold PBS and fixed in 4% paraformaldehyde at 4ºC overnight. After fixation, specimens were cryoprotected in 30% sucrose and embedded in 7.5% gelatin: 15% sucrose. Spinal cords were then conserved at -80ºC until sectioning in a cryostat. Cervical and thoracic sections of 12 µm were used in the analysis.

### Immunofluorescence

For immunofluorescence, sections were degelatinized at 37ºC for 20 min, followed by a pre-treatment with glycine 0.1 M for 10 min at room temperature (RT). Permeabilization was performed using Tritonx100 (0.5%) for 10 min, followed by blocking (either or 6% albumin in TBST for 1h30 min or 10% Fetal Bovine Serum in TBST for 30 min, at RT). Primary antibodies against NeuN (MAB377 Merck Millipore) or CHX10 (Exalpha X1180P) were incubated O/N at 4ºC. Sections were then subsequently washed and incubated with appropriate secondary antibodies (Molecular Probes) for 1 h at RT. DAPI counterstain and Mowiol mounting followed.

### Animals and data collection on LocoMouse

Data collection was performed on four groups of animals **(a)** *Dll1f/+Dll4*f/+*Nestin-Cre* mice (N=6; n=7495; female=1; male=5; 3-5 months old) **(b)** *Dll4*f/f*Nestin-Cre* mice (N=5; n=7025; male=5; 3-5 months old) **(c)** *Dll1*f/+*Dll4*f/f*Nestin-Cre* mice (N=5; n=6637; female=1; male=4; 3-5 months old) and **(d)** their littermate controls (N=18; n=21,501; female=5; male=14; 2 -5 months old)

Mice were handled by the experimenter and allowed to acclimate to the LocoMouse setup before data collection. Animals were weighed before each session. Mice walked freely between two dark boxes on either end of the glass corridor. No food or water restriction or reward was used. For a more detailed description of the LocoMouse setup please read paper (Machado, darmohray et al., 2015)

More than 15 corridor passages (trials) were collected in each of five daily sessions. Movies were collected at 400 frames per second with a spatial resolution of 1440x250 pixels. A total of 21,501 strides were collected from littermate controls, which corresponds to 1131 ± 134 strides per mouse. For *Dll1*f/+*Dll4*f/+*Nestin-Cre* mice we collected a total of 7495 strides (1249 ± 238 strides per mouse). For *Dll4*f/f*Nestin-Cre* mice we collected a total of 7025 strides per mouse (1045 ± 224 strides per animal per paw) and for *Dll1*f/+*Dll4*f/f*Nestin-Cre* mice we collected a total of 6637 strides (1327 ± 324 strides per mouse).

### Data acquisition

Movies were collected at 400 frames per second with a spatial resolution of 1440x250 pixels. Acquisition software was written in Labview and uses 2 National Instruments boards (PCIe 1433 and BNC 2120) to record and save the movies, in real time. The tracking algorithm and data analysis software were written in Matlab (Mathworks) and performed offline. The LocoMouse Tracker code used in this paper can be downloaded from GitHub (https://github.com/careylab/LocoMouse).

### Data analysis

Tracking and data analysis were performed offline. We used the tracking algorithm and data analysis software from the LocoMouse system . The LocoMouse Tracker can be downloaded from GitHub (https://github.com/careylab/LocoMouse).

The stride is composed by the swing and stance phase. The trajectories of individual paws were automatically broken down into swing and stance phases based on the first derivative of the paw position trajectories. Individual strides were defined from stance onset to subsequent stance onset. For each stride, average walking speed was calculated by dividing the forward motion of the body center during that stride by the stride duration. All data was sorted into speed bins (0.05 m/s bin width) in a stridewise manner, with a minimum stride count criterion of 5 strides per bin, per animal. A list of individual limb movements and interlimb coordination and its calculation is provided:

**Trial analysis**

Velocity (x,y): Instantaneous trail velocity relative to nose by trial (m/s)

Trial duration: Total trial duration (s)

Stance onset: All the stance onset in time of FR paw during trial (s)

**Individual limb parameter**

Cadence: Inverse of stride duration (s-1)

Swing velocity: x displacement of single limb during swing phase divided by swing duration (m/a).

Stride length: x displacement from touchdown to touchdown of single limb (mm).

Stance duration: Time in milliseconds that foot is on the ground during stride (ms).

Trajectories: Trajectories were aligned to swing onset and resampled to 100 equidistant points using linear interpolation. Interpolated trajectories were then binned by speed and the average trajectory was computed for each individual animal and smoothed with a Savitzky-Golay first-order filter with a 3-point window size (% norm).

Interlimb and whole-body coordination parameters

Stance phase: relative timing of limb touchdowns to stride cycle of reference paw. Calculated as: (stance time−stance timereference paw)/stride duration (%).

Supports: support types were categorized by number of paws on ground expressed as a percentage of the total stride duration for each stride. Paw support categories are four, three, two diagonals, two other (homolateral and homologous), one, and zero (%).

Immuno-positive cells were counted and expressed as a percentage of total cell numbers ($DAPI^+$). Images were taken with a motorized widefield fluorescence Microscope (Zeiss Axiovert 200M). Except when otherwise specified, a minimum of 3 animals (from independent litters) were analyzed.

**Statistical analysis**

Statistical analyses were done in Matlab and R. For all comparisons, models were selected by comparing equations specifying additive fixed-effects terms with those specifying n-way interaction terms using a likelihood-ratio test and inspection of statistical significance of included terms. Depending on the comparison, fixed-effects terms included a subset of the following variables: speed, genotype and paw. All models were random-intercepts models with subject as a random covariate. Unless otherwise indicated, results are reported as conditional F tests with Satterthwaite degrees of freedom correction.

Cell counting results were represented as mean ± standard error of the mean. Statistical significance was considered when $p<0.05$ using the student's t-test.

## 5.3 Results

### 5.3.1 Using LocoMouse to reveal specific motor impairments in spinal cord mutant mice

The LocoMouse system (**Figure 5.1. A-B**) was used to quantify specific motor impairments in different groups of spinal cord mutant mice: **(a)** *Dll1*f/+*Dll4*f/+*Nestin-Cre* (green) N=6; **(b)** *Dll4*f/f*Nestin-Cre* N=5 (red); **(c)** *Dll1*f/+*Dll4*f/f*Nestin-Cre* N=5 (blue) (**Figure 5.1. C**). As it was previous described in **chapter 2**, the LocoMouse apparatus is composed by two dark boxes, a high-speed camera, a glass corridor, a mirror and motion sensors (**Figure 5.1 A**). Individual trials (single movies) consisted in single passages on the corridor. Each group of animals ran 5 sessions (with ~ 20 trials each) during a week. Movies, were than processed offline using the LocoMouse Tracker (Machado, Darmohray et al., 2015, GitHub: https://github.com/careylab/LocoMouse). The LocoMouse Tracker automatically detects and tracks the position of all four paws, nose and 15 tail segments in 3D with high temporal (2.5ms) and spatial resolution (**Figure 5.1. B**). The tracks of the four paws were then divided into swing and stance phases for further analysis.

For a general overview of the animal's performance in the behavioral task, the total trial duration were analyzed. Only *Dll4*f/f*Nestin-Cre* (red) mice showed longer trial durations (**Figure 5.1. D**). No impairments were observed for *Dll1*f/+*Dll4*f/+*Nestin-Cre* mice (green).

### 5.3.2 Kinematic parameters of a single limb: Stride length is impaired in *Dll4*f/fNestin-Cre and *Dll1*f/+*Dll4*f/fNestin-Cre mice

As a starting point for quantifying specific motor impairments we first analyzed the basic kinematic parameters, such as stride length (mm), cadence ($s^{-1}$) and stance duration (ms) across walking speeds (**Figure 5.2**). Since mice were allowed to walk freely in the corridor a

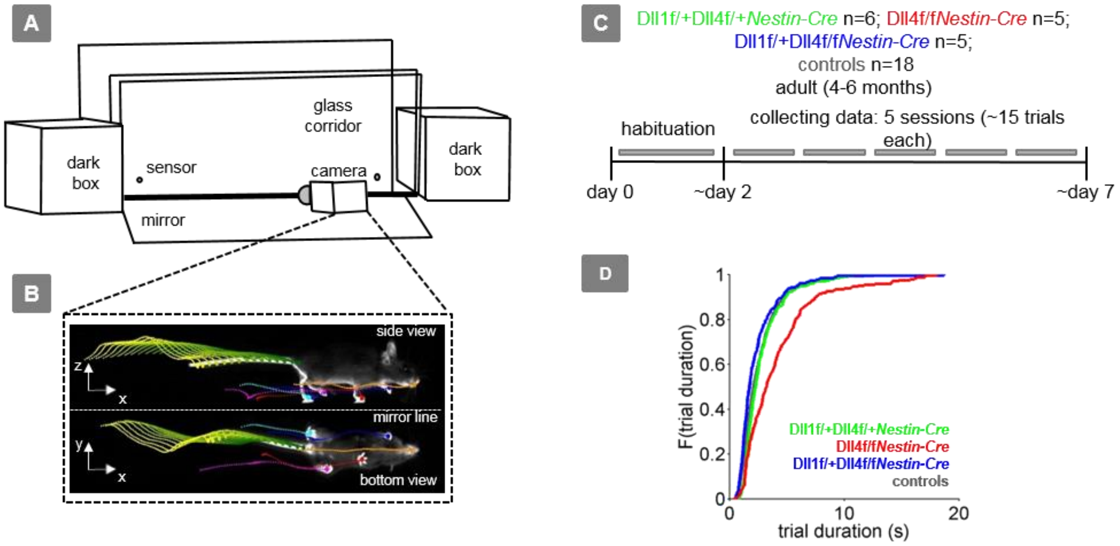

**Figure 5.1. Using the LocoMouse system to quantify specifically motor impairments in spinal cord mutant mice.**

**(A)** LocoMouse setup schematic, composed of two dark boxes, a glass corridor, motion sensors, a camera and a mirror (at 45º). Mice cross the corridor from one dark box to another. **(B)** An example of a single frame captured at 400 frames per second with the side and bottom view (mirror reflection). Continuous tracks (in x, y, z) for nose, paws and tail segments are plotted on top of the frame. The tracks were obtained from the LocoMouse Tracker (ref). **(C)** Experimental protocol. Three groups of spinal cord mutant mice, *Dll1f/+Dll4f/+Nestin-Cre* (green, n=6), *Dll1f/+Dll4*f/f*Nestin-Cre* (blue, n=5), *Dll4*f/f *Nestin-Cre* (red, n=5), and their littermate controls n=18 were tested. After habitation, animals ran 5 sessions (~15 passages each session) in the LocoMouse system during a week. **(D)** Cumulative distribution of trial duration for each group.

variety of walking speeds was obtained. We therefore sorted all strides for individual mice into speed bins in a stridewise manner and analyzed them with respect to the mouse's walking speed. A total of 10894 strides from the front right (FR) paw were collected. *Dll4*f/f*Nestin-Cre* (red) mice walked slower when compared to the other groups. (**Figure 5.2. A**). As it was previous described, kinematic parameters vary with walking speed (Clarke and Still, 1999; Lalonde and Strazielle, 2007; Batka et al., 2014; Machado, Darmohray *et al*., 2015). (**Figure 5.2. B-D**).

Taking into consideration the walking speeds of each group, only the stride length showed significant perturbations. The stride length was shorter for *Dll4*f/f*Nestin-Cre* (red) and *Dll1*f/+*Dll4*f/f*Nestin-Cre* (blue) mice, even when compared with the model prediction (dash grey lines) (**Figure 5.2. C**). Both front and hind paws showed shorter stride lengths (*Dll1*f/+*Dll4*f/+*Nestin-Cre*: $F_{(49.5,1)}$=2.1, p=0.02; *Dll4*f/f*Nestin-Cre:* $F_{(39.4,1)}$=4.2, p=0.04; *Dll1*f/+*Dll4*f/f*Nestin-Cre:* $F_{(44.4,1)}$=6, p=0.01, **Figure 5.2. H**).

The model prediction, which accurately predicted the control animals, was based on the

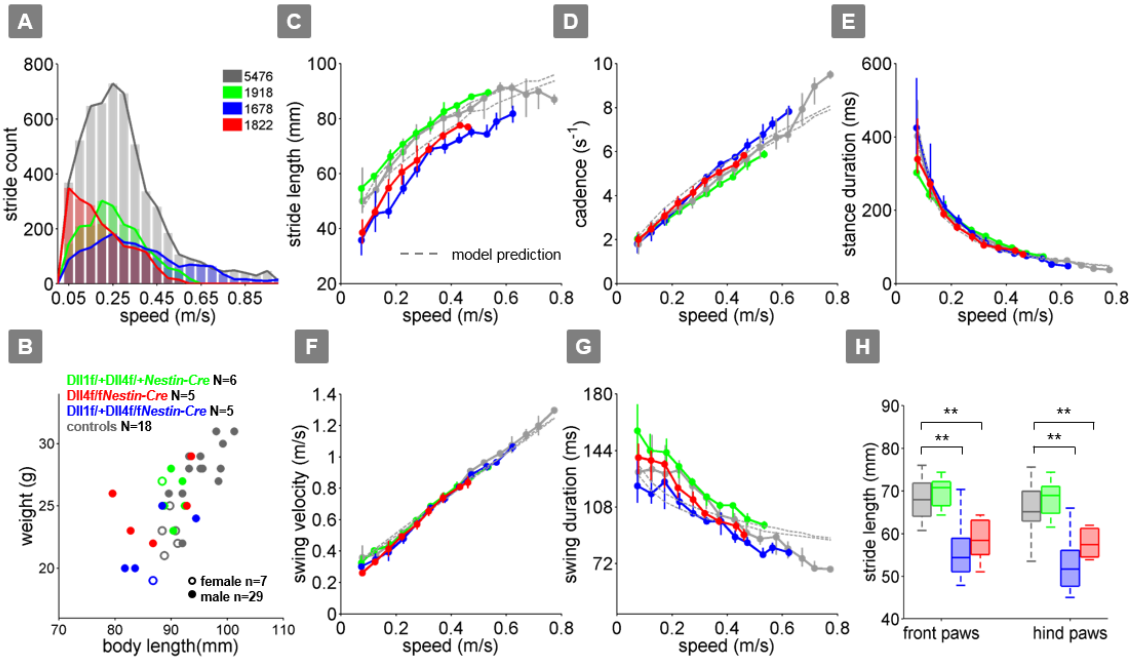

**Figure 5.2. Stride length is impaired in *Dll4*f/f*Nestin-Cre* and *Dll1*f/+*Dll4*f/f*Nestin-Cre* mice.**

**(A)** Stride count histogram binned by average walking speed for each group. Strides are divided into speed bins of 0.05 m/s. A total of 10894 strides from the FR paw were collected during a week and further analyzed. **(B)** Specific mouse properties for all 35 animals. *Dll1*f/+*Dll4*f/+*Nestin-Cre* n=6; *Dll1*f/+*Dll4*f/f*Nestin-Cre* n=5, *Dll4*f/f*Nestin-Cre* n=5 and littermate controls n=18. Each animal is plotted as a circle, open circles are females n=7 and solid are males n=23. **(C-G)** Basic stride parameters: **(C)** Stride length (mm), **(D)** cadence ($s^{-1}$) and **(E)** stance duration (s) **(F)** swing velocity (m/s) **(G)** swing duration (ms) by walking speed for the FR paw. The median and ± 25th, 75th percentiles are represented for each group of animals. Dash grey lines represent the model prediction based on the walking speed and weight of the animals (maximum and minimum values). **(H)** Box plots (median and 25th, 75th percentiles values) are used to compare the data distribution of stride length at a speed bin of 0.25 m/s . Front and hind paws are represented for each group.

linear mixed-effects model that took into consideration the speed and weight of group animal (Machado, Darmohray et al., 2015). Animal properties were plotted in **Figure 5.2 B** and although there was a slight difference in weight between groups (Control mice w=26.6g; *Dll1*f/+*Dll4*f/+*Nestin-Cre* (green) w=25.8; *Dll4*f/f*Nestin-Cre* (red) w=25g; *Dll1*f/+*Dll4*f/f*Nestin-Cre* (blue) w=22.6g), in general those differences were not meaningful. Cadence, swing velocity and stance duration did not show impairments ($F_{(74.6,3)}$=2.35, p=0.8 and $F_{(639,3)}$=0.52, p=0.7, **Figure 5.2 D, E, F**). Swing duration for *Dll4*f/f*Nestin-Cre* (red) and *Dll1*f/+*Dll4*f/f*Nestin-Cre* (blue) was, on average, slightly lower than the control animals (but with no statistically significant differences; $F_{(32.9,3)}$=2.3, p=0.1). No impairment was observed in the kinematic parameters for *Dll1*f/+*Dll4*f/+*Nestin-Cre* mice (green).

### 5.3.3 3D paw trajectories: Side to side (y) and vertical (z) movement are perturbed during swing phase for *Dll4*f/fNestin-Cre and *Dll1*f/+*Dll4*f/fNestin-Cre mice

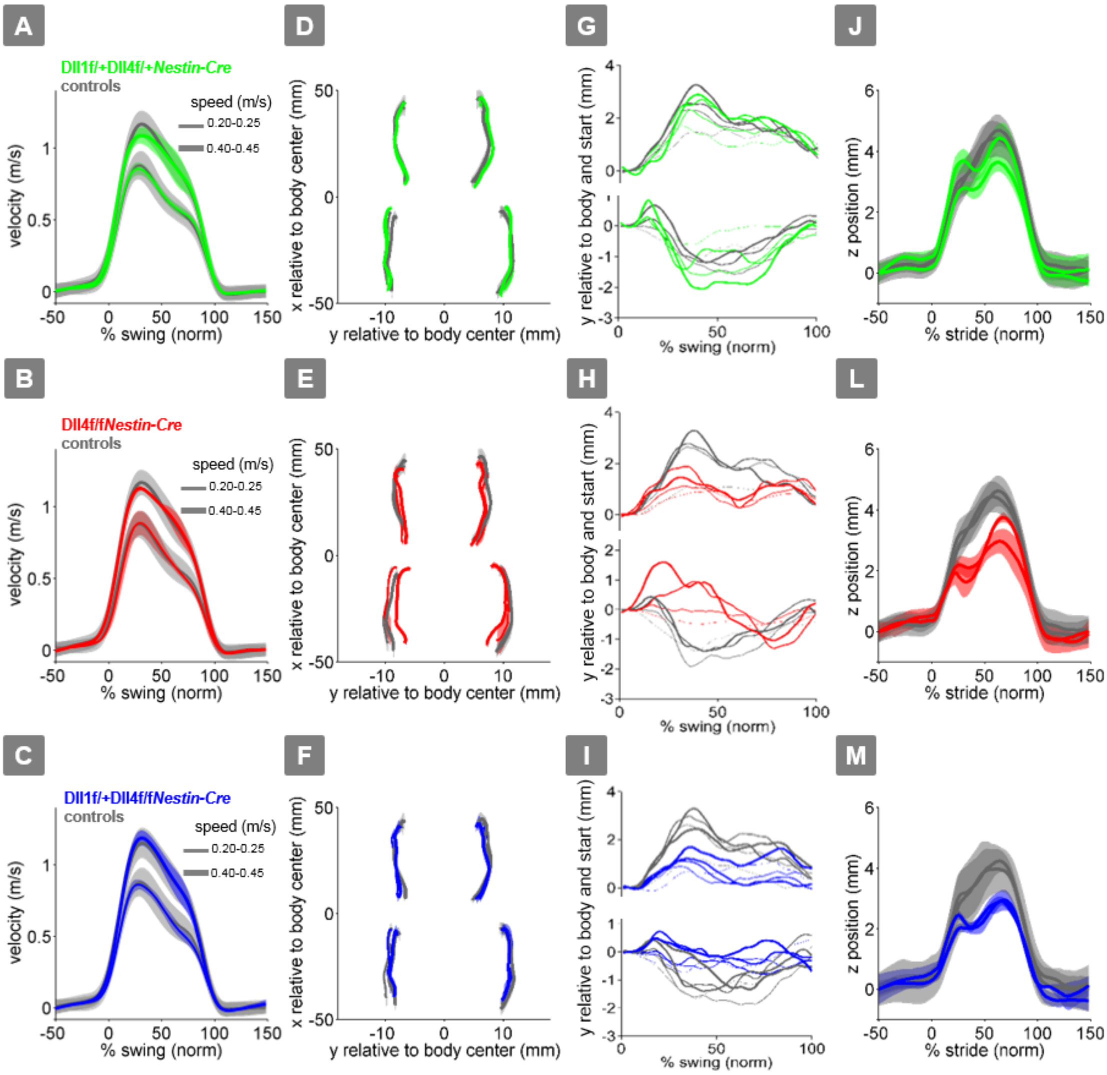

**Figure 5.3. Side to side (y) and vertical (z) movement are perturbed during swing phase for *Dll4*f/f*Nestin-Cre* and *Dll1*f/+*Dll4*f/f*Nestin-Cre* mice.**

**(A-C)** Average instantaneous x velocity of FR paw during swing phase for **(A)** *Dll1*f/+*Dll4*f/+*Nestin-Cre* (green) mice **(B)** *Dll4*f/f*Nestin-Cre* (red) mice **(C)** *Dll1*f/+*Dll4*f/f*Nestin-Cre* (blue) mice and size-matched controls (grey). **(D-F)** Average x-y position of four paws relative to body center during swing. **(D)** *Dll1*f/+*Dll4*f/+*Nestin-Cre* (green) mice **(E)** *Dll4*f/f*Nestin-Cre* (red) mice **(F)** *Dll1*f/+*Dll4*f/f*Nestin-Cre* (blue) mice and size-matched controls (grey). **(G-I)** Average side to side movement (y) for FR (top) and FL (bottom) paws relative to body midline across a range of speeds: 0.15 – 0.45 m/s. **(G)** *Dll1*f/+*Dll4*f/+*Nestin-Cre* (green) mice **(H)** *Dll4*f/f*Nestin-Cre* (red) mice **(I)** *Dll1*f/+*Dll4*f/f*Nestin-Cre* (blue) mice and size-matched controls (grey). **(J-M)** Average vertical (z) position for FR paw relative to ground during swing. **(J)** *Dll1*f/+*Dll4*f/+*Nestin-Cre* (green) mice **(L)** *Dll4*f/f*Nestin-Cre* (red) mice **(M)** *Dll1*f/+*Dll4*f/f*Nestin-Cre* (blue) mice and size-matched controls (grey). Thick lines represent average values and shadows standard deviation.

Next we examined the continuous 3D paw trajectories for size-matched control, and spinal cord mutant mice: *Dll1*f/+*Dll4*f/+*Nestin-Cre, Dll4*f/f*Nestin-Cre* and *Dll1*f/+*Dll4*f/f*Nestin-Cre* mice (**Figure 5.3**). Spinal cord mutant mice when compared to size-matched control animals did not exhibit differences in forward paw velocity profile across speeds (**Figure 5.3. A-C**). Forward paw velocity profile changes with speed, Paw velocity peaked early during swing and decelerated before stance onset across speeds. No significant differences between paws and genotypes were observed ($F_{(472.6,3)}$=0.74, p=0.5).

We then analyzed the off-axis movements (y and z trajectories). The distance in y from the body center to all four paws (base of support) for the spinal cord mutants were not altered $F_{(39,3)}$=0.3, p=0.8, **Figure 5.3 D-F**). However, the side-to-side trajectory (y excursion) during swing for both *Dll4*f/f*Nestin-Cre* (red) and *Dll1*f/+*Dll4*f/f*Nestin-Cre* (blue) mice showed impairments relative to control animals (**Figure 5.3 G-I** *Dll1*f/+*Dll4*f/+*Nestin-Cre*: $F_{(16.9,1)}$=0.74, p=0.4; *Dll4*f/f*Nestin-Cre:* $F_{(19.3,1)}$=10.9, p=0.003; *Dll1*f/+*Dll4*f/f*Nestin-Cre:* $F_{(10.9,1)}$=7.3, p=0.02). Further, analysis of the vertical (z) trajectories revealed significantly differences for *Dll4*f/f*Nestin-Cre* (red) and *Dll1*f/+*Dll4*f/f*Nestin-Cre* (blue) mice (**Figure 5.3 J-M**). Lower vertical z positions across speeds was exhibited for front and hind paws (*Dll1*f/+*Dll4*f/+*Nestin-Cre*: $F_{(34.2.,1)}$=0.67, p=0.4; *Dll4*f/f*Nestin-Cre:* $F_{(40.9,1)}$=30.5, p<0.001; *Dll1*f/+*Dll4*f/f*Nestin-Cre:* $F_{(30.9,1)}$=23, p<0.001). No impairment was observed in the 3D paw trajectory for *Dll1*f/+*Dll4*f/+*Nestin-Cre* (green) mice.

### 5.3.4 Interlimb: Gait and support patterns are preserved during overground locomotion

Wildtype mice walked in a symmetrical trot pattern across speeds – each diagonal pair of limbs moved together and alternated with the other pair, represented as a polar plot in **Figure 4. A** (bottom) and in a more conventional format the Hildebrand pots in **Figure 4. B.** In the polar plot the phase of the step cycle in which each limb enters stance were plotted. Each paw is aligned to the onset of FR paw. Distances from the origin represent walking speeds. The FR paw was represented as solid circles, the FL paw as triangles, HR paw as diamond markers and HL paw as solid squares **Figure 5.4. A** (top). In our experiments, no other gait patterns besides the symmetrical trot pattern was observed in the range of speeds analyzed (0.05-0.8 m/s), as previously described (Machado, Darmohray et al., 2015). Surprisingly, the symmetrical trot pattern was preserved in all spinal cord mutant mice when compared to control (**Figure 5.4. C-D: top row)**. The left-right alternation was maintained (*Dll1*f/+*Dll4*f/+*Nestin-Cre*: $F_{(106.3,1)}$=2.4, p=0.1; *Dll4*f/f*Nestin-Cre:* $F_{(102.1,1)}$=1.9, p=0.2; *Dll1*f/+*Dll4*f/f*Nestin-Cre:* $F_{(97.2,1)}$=0.29, p=0.6)., **Figure 5.4. C-D: bottom row)**. No increase in variability was observed.

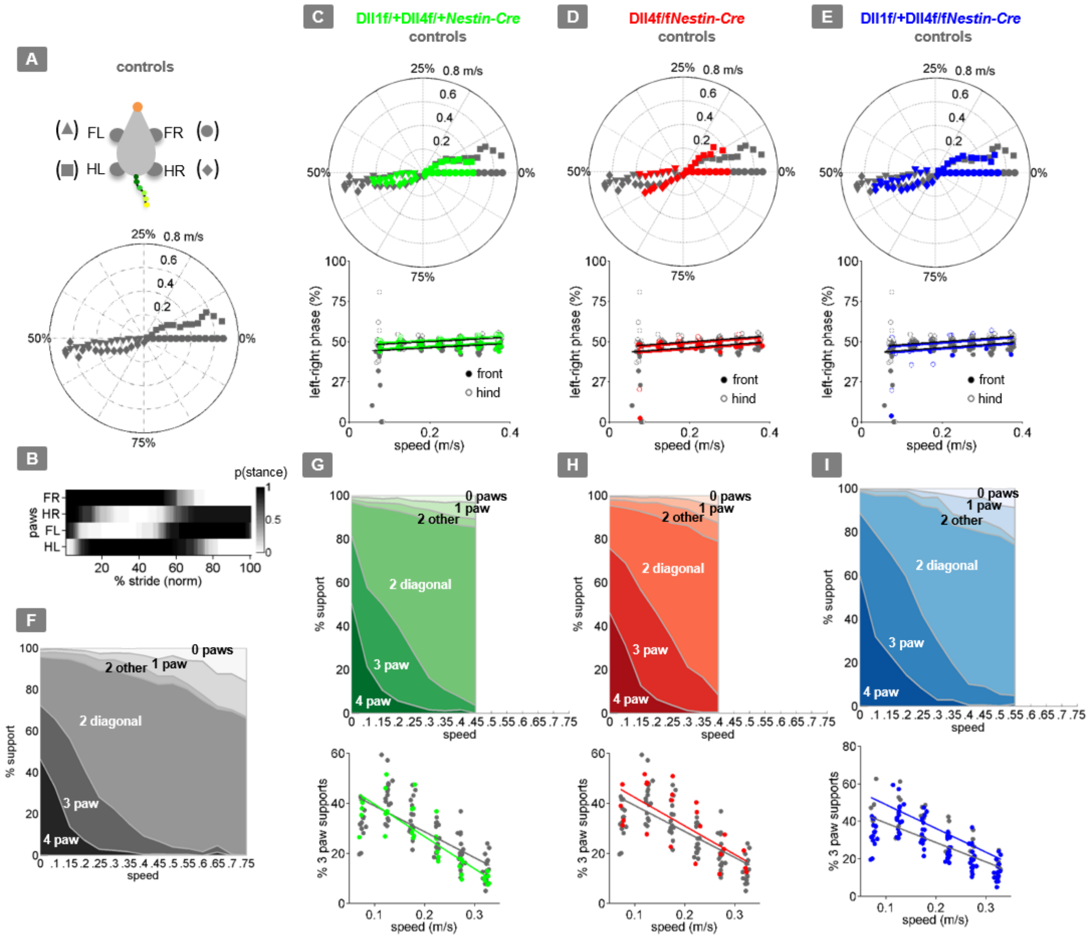

**Figure 5.4. Gait and support patterns are preserved during overground locomotion.**

**(A, C-E)** Polar plot indicating the phase of the step cycle in which each limb enters stance, aligned to stance onset of FR paw (circle marker). Distances from the origin represent walking speed, average values are plotted. The FR paw is represented as a circle marker, FL- triangle, HR – diamond and HL – square marker. **(A)** Polar plot for control mice. **(B)** Average Hildebrand plot aligned to FR stance onset for speeds between 0.15 and 0.20 m/s. Grayscale represents probability of stance. **(C-E)** Top row: Polar plots for spinal cord mutant mice (colors) overlaid on top of control animals (grey). Bottom row: Left-right phase for spinal cord mutant mice (colors) and controls (grey) across speeds. Circles show average values for each animal. Lines show fit of linear-mixed effects model for each variable. **(F-I)** Support patterns. Area plot of average paw support types as a percentage (%) of stride cycle, across speeds for **(F)** controls, **(G)** top row – *Dll1*f/+*Dll4*f/+*Nestin-Cre* (green) mice; **(H)** top row - *Dll4*f/f*Nestin-Cre* (red) mice; **(I)** top row - *Dll1*f/+*Dll4*f/f*Nestin-Cre* (blue). **(G-I)** Bottom row: Percentage of 3 paws support for each animal (circles) - average values across speeds. Lines show fit of linear-mixed effects model.

Support patterns, or the configuration of paws on the ground at any given time, vary systematically with walking speed (Górska et al., 1999). Typically, wildtype mice had two diagonal paws on the ground at any given time (2-paw diagonal support), but had support patterns that ranged from 3 paws on the ground during slow walking to 0 paw supports, or brief periods of flight, during running at higher speeds, due to changes in stance to swing phasing. The supports pattern for control animals were represented in **Figure 5.4 F,** while the spinal cord mutant mice were represented in **Figure 5.4 G-I** (top row)**.** No differences were observed between the mutants and control animals. As an example, the percentage of 3 paw support was used to highlight this point. (*Dll1*f/+*Dll4*f/+*Nestin-Cre*: $F_{(312.,1)}$=1.7, p=0.2; *Dll4*f/f*Nestin-*

*Cre:* $F_{(232,1)}=0.8$, p=0.4; *Dll1*f/+*Dll4*f/f*Nestin-Cre:* $F_{(302,1)}=0.9$, p=0.3, **Figure 5.4 G-I** bottom row).

### 5.3.5 Nose and tail oscillation across speed bins and tail segments: Impairments are restricted to tail movement in *Dll4*f/fNestin-Cre and *Dll1*f/+*Dll4*f/fNestin-Cre mice

In order to characterize whole-body locomotor coordination in both control and spinal cord mutant mice, we analyzed their head and tail movements while they walked freely across the corridor. In the size-matched control animals and *Dll1*f/+*Dll4*f/+*Nestin-Cre* (green) mice the lateral movements of nose and tail segments were similar to each other (*Dll1*f/+*Dll4*f/+*Nestin-Cre*: nose $F_{(14.9,1)}=1.5$, p=0.6 and tail $F_{(153,1)}=2.3$, p=0.8 , **Figure 5.5 A, D)**.

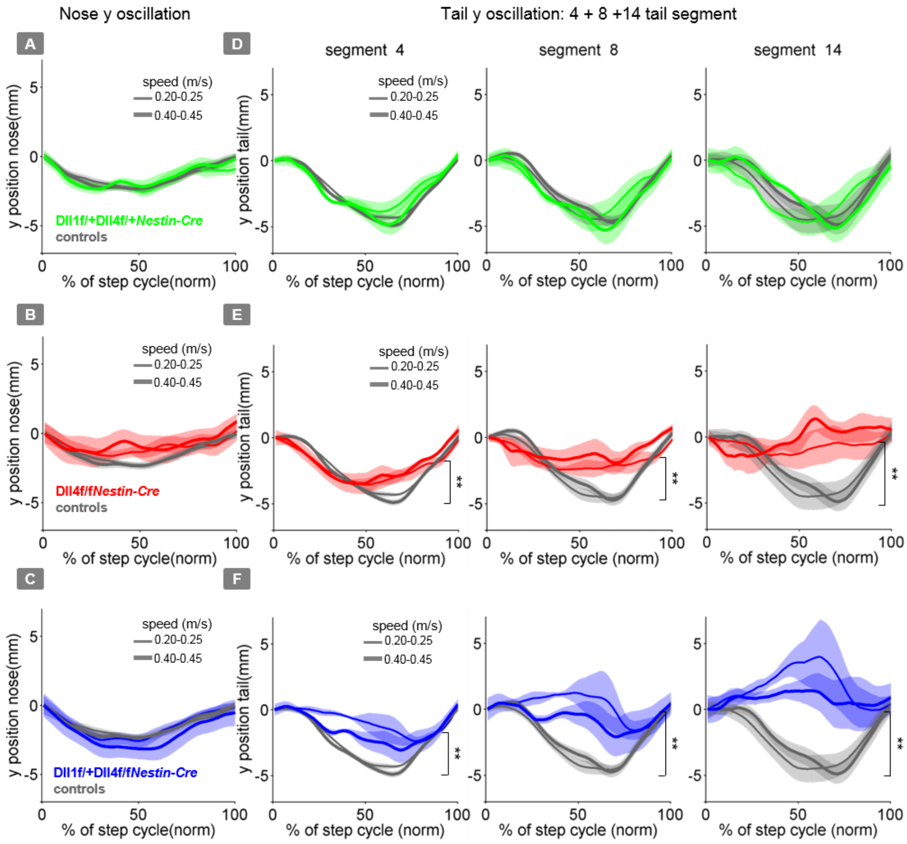

**Figure 5.5. Nose and tail oscillation across speed bins and tail segments. Impairments are restricted to tail movement in *Dll4*f/f*Nestin-Cre* and *Dll1*f/+*Dll4*f/f*Nestin-Cre* mice.**

**(A-C)** Average interpolated side to side (y) trajectory of nose for **(A)** *Dll1*f/+*Dll4*f/+*Nestin-Cre* (green) mice; **(B)** *Dll4*f/f*Nestin-Cre* (red) mice; **(C)** *Dll1*f/+*Dll4*f/f*Nestin-Cre* (blue) and control (grey) mice. Nose trajectories are aligned with stance onset of the front right paw. **(D-F)** Average interpolated (y) trajectory of tail segment: 4, 8, 14 for (D) *Dll1*f/+*Dll4*f/+*Nestin-Cre* (green) mice; **(E)** *Dll4*f/f*Nestin-Cre* (red) mice; **(F)** *Dll1*f/+ *Dll4*f/f*Nestin-Cre* (blue) and control (grey) mice. Tail trajectories are aligned with stance onset of the hind right paw. Thick lines and shadows represent the average values and standard deviation, respectively, for each group of animals.

In contrast, impairments of *Dll4*f/f*Nestin-Cre* (red) and *Dll1*f/+*Dll4*f/f*Nestin-Cre* (blue) mice were restricted to tail oscillations, while the lateral nose movement was preserved ($F_{(22.5,2)}$=1.7, p=0.4, **Figure 5 5 B, C)**. The amplitude of the tail oscillation was much smaller than size-matched control animals ($F_{(232.1,2)}$=30.7, p<0.001, **Figure 5.5 E, F**).

Taken together, these results suggest that the impairments in the spinal cord mutant mice, namely *Dll4*f/f*Nestin-Cre* (red) and *Dll1*f/+*Dll4*f/f*Nestin-Cre* (blue), were restricted to intralimb parameters while the interlimb coordination was preserved. Lateral (y) and vertical (z) movement were clearly perturbed in both single paw movement and tail segments. The kinematic parameters revealed perturbation on a spatial level, with shorter stride lengths.

## Histologic characterization of *Dll1* and/or *Dll4* mutant spinal cords

We characterized *Dll1* and/or *Dll4* mutant cervical and thoracic spinal cords in terms of total numbers of neurons (NeuN positive) and V2a interneurons (CHX10 positive). Cervical spinal cords of *Dll4*f/f*Nestin-Cre* mutants did not exhibit significant changes in the numbers of NeuN positive neurons (**Figure 5.6 A** and **B**). However, the numbers of V2a interneurons increased from 2,2±0,4% in the wildtype to 4,0±0,2% in the *Dll4*f/f*Nestin-Cre* mutant (p<0,05, **Figure 5.6 C** and **D**). Thoracic spinal cord exhibited no significant changes in the numbers of either NeuN positive neurons or V2a interneurons (**Figure 5.6 A-D**).

Numbers of NeuN positive neurons increased from 16,0±1,4% in the wildtype to 22,8±0,9% in the *Dll1f/+Dll4*f/f*Nestin-Cre* mutant cervical spinal cord (p<0,05, **Figure 5.6 A** and **B**). V2a interneurons increased from 2,2±0,4% to 4,2±0,6% (p<0,05, **Figure 5.6 C** and **D**). In the same mutants, thoracic spinal cord had significant changes in the numbers NeuN positive neurons (from 17,9±0,6% to 24,3±3,0%, p<0,05, **Figure 5.6 A** and **B**) and V2a interneurons (from 4,0±0,3% to 7,5±1,0%, p<0,05, **Figure 5.6 C** and **D**).

Overall, both *Dll4*f/f*Nestin-Cre* and *Dll1f/+Dll4*f/f*Nestin-Cre* exhibited increases in the numbers of V2a INs: *Dll4*f/f*Nestin-Cre* at the cervical level and *Dll1f/+Dll4*f/f*Nestin-Cre* both in cervical and thoracic spinal cord segments. Numbers of total neurons are only increased in *Dll1f/+Dll4*f/f*Nestin-Cre* mice in the cervical and thoracic segments of the spinal cord.

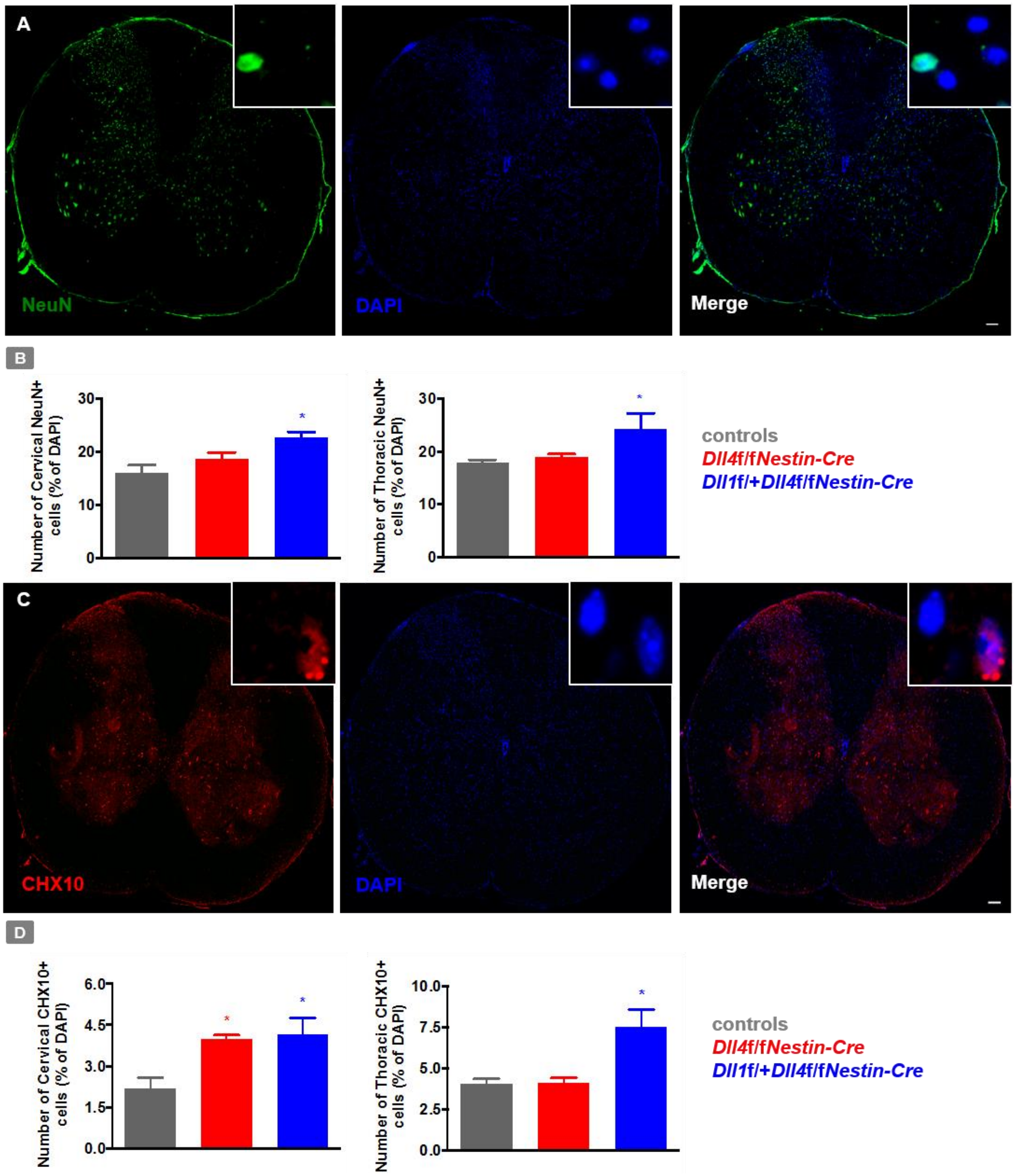
A
NeuN
DAPI
Merge
B
Number of Cervical NeuN+ cells (% of DAPI)
30
20
10
0
*
Number of Thoracic NeuN+ cells (% of DAPI)
30
20
10
0
*
controls
Dll4f/fNestin-Cre
Dll1f/+Dll4f/fNestin-Cre
C
CHX10
DAPI
Merge
D
Number of Cervical CHX10+ cells (% of DAPI)
6.0
4.5
3.0
1.5
0.0
*
*
Number of Thoracic CHX10+ cells (% of DAPI)
10.0
7.5
5.0
2.5
0.0
*
controls
Dll4f/fNestin-Cre
Dll1f/+Dll4f/fNestin-Cre

**Figure 5.4. Gait and support patterns are preserved during overground locomotion.**

**(A, C-E)** Polar plot indicating the phase of the step cycle in which each limb enters stance, aligned to stance onset of FR paw (circle marker). Distances from the origin represent walking speed, average values are plotted. The FR paw is represented as a circle marker, FL- triangle, HR – diamond and HL – square marker. **(A)** Polar plot for control mice. **(B)** Average Hildebrand plot aligned to FR stance onset for speeds between 0.15 and 0.20 m/s. Grayscale represents probability of stance. **(C-E)** Top row: Polar plots for spinal cord mutant mice (colors) overlaid on top of control animals (grey). Bottom row: Left-right phase for spinal cord mutant mice (colors) and controls (grey) across speeds. Circles show average values for each animal. Lines show fit of linear-mixed effects model for each variable. **(F-I)** Support patterns. Area plot of average paw support types as a percentage (%) of stride cycle, across speeds for **(F)** controls, **(G)** top row – *Dll1*f/+*Dll4*f/+*Nestin-Cre* (green) mice; **(H)** top row - *Dll4*f/f*Nestin-Cre* (red) mice; **(I)** top row - *Dll1*f/+*Dll4*f/f*Nestin-Cre* (blue). **(G-I)** Bottom row: Percentage of 3 paws support for each animal (circles) - average values across speeds. Lines show fit of linear-mixed effects model.

## 5.4 Discussion

The LocoMouse system combines high spatial-temporal resolution with machine learning techniques to automatically track the different body parts, allowing mice to walk as naturally as possible (Machado, Darmohray et al., 2015). The LocoMouse System allowed for detailed characterization of specific motor perturbations that resulted from deletion of the *Dll1* and/or *Dll4* ligands in the developing V2 domain of the spinal cord. This will contributed to an understanding of the role the cells (particularly in the spinal cord) under the developmental programming of the notch signaling pathway play in locomotion. The ability to quantify with high sensitivity and precision motor impairments is particularly crucial when motor perturbations in mice are difficult to observe using the human eye, which was the case of *Dll1* and/or *Dll4* mutant mice.

Our main findings in *Dll4f/fNestin-Cre* and *Dll1*f/+*Dll4*f/f*Nestin-Cre* mice are related to impairments in intra-limb and tail parameters. We found that (a) stride lengths were shorter; (b) limb trajectories were particularly perturbed in the y and z dimensions; and (c) side-to-side tail movement was impaired. No motor impairments were observed in *Dll1f/+Dll4f/+Nestin-Cre* mice.

*Dll1* and *Dll4* are required to generate cell diversity in the pV2 domain. *Dll4*+ precursors have been speculated to give rise to V2a INs, whereas the neighboring *Dll4-* precursors, which receive the *Dll4* ligand and activate the Notch pathway, differentiate into V2b INs (Peng, Yajima et al. 2007). Accordingly, our histology results showed that deletion of the two *Dll4* alleles (*Dll4f/fNestin-Cre* mice) in the spinal cord results in an increase of V2a INs (CHX10 positive cells), at the level of the cervical spinal cord. The increase of V2a INs is probably responsible for the observed perturbation of limb and tail trajectories during overground locomotion. In addition, impairment in forelimbs could cause abberant hindlimb movements as well.

In the spinal cord domains where *Dll1* is the only expressed Notch ligand, inactivation leads to an increased rate of neurogenesis and premature differentiation of neural progenitors. In the pV2 domain where *Dll1* is co-expressed with *Dll4*, progenitors are not exhausted and cell diversity is maintained: *Dll4* partially compensates for *Dll1* loss (Rocha et al 2009).~

In *Dll1*f/+*Dll4*f/f*Nestin-Cre* mice, deletion of one copy of *Dll1* and two copies of *Dll4* in the spinal cord results in an aggravation of phenotype comparing to *Dll4*f/f*Nestin-Cre* mice: there is an increase of V2a INs not only at the cervical level but also at the thoracic level. NeuN+

neurons at the level of the cervical and thoracic spinal cord were also increased in *Dll1*f/+*Dll4*f/f*Nestin-Cre* mice. In accordance with the higher values of V2 INs, the differences observed in the intra-limb parameters were also more dramatic for *Dll1*f/+*Dll4*f/fNestin-Cre mice when compared to *Dll4f/fNestin-Cre* mice. The stride length is clearly shorter and the y excursion of the tail is more impaired. *Dll1f/+Dll4f/+Nestin-Cre* spinal cords were not analyzed histologically as no motor impairments were observed in these mice.

As a conclusion, increasing numbers of V2 INs, resulting from deletion of *Dll1* and/or *Dll4*, leads to specific impairments restricted to intra-limb parameters, while the interlimb coordination was preserved. *Dll1*f/+*Dll4*f/f*Nestin-Cre* mice had a more striking phenotype as compared to *Dll4f/fNestin-Cre* mutants.

# 6

# Conclusions

## The use of LocoMouse to quantify whole-body coordination in mice

Here I described the LocoMouse system, an automated tool for specific quantitative kinematic analysis in small laboratory animals, such as mice. With the LocoMouse we can observe the animal from 2 sides simultaneously which provides sensitive, specific and detailed readouts for movement (in 3 dimensions, x, y and z) of all different body parts, i.e. nose, limbs, tail. This also makes LocoMouse a unique translational tool given that most of motor impairments in humans are assessed in a similar way (Machado, Darmohray et al. 2015).

Mice walk as naturally as possible through the LocoMouse corridor and data is collected automatically. In this way, animals are accurately and consistently screened for locomotor impairments in a high-throughput fashion. A tracking code was also developed to maximize the throughput. It combines machine learning and multi-target tracking algorithms (Russell, de Agapito et al. 2011) with high spatiotemporal resolution. With the LocoMouse tracking system and during this project we tracked animals of different sizes, different ages, different genders, different mutant mouse models, acute manipulation and track trajectories across several walking speeds. Hundreds or even thousands of strides per animal were used to quantify locomotion.

The ability to collect such a large dataset was fundamental for establishing a comprehensive framework for whole-body coordination in mice. To this multidimensional dataset we applied multilevel linear mixed effects model  to quantify and predict individual limb gait parameters. From these approach, several equations can now be used to predict stride parameters for a given mouse walking at a particular speed. The whole-body movement quantification, quantifying limbs, nose and tail movement relative to each other, were crucial to identify specific core features of ataxia.

## Ataxic mutant mice used as a model to investigate cerebellar contributions to coordinated movement

To investigate the role of cerebellum in gait coordination we used *pcd* and *reeler* mice as cerebellar ataxic mice. The major neuroanatomical finding in *pcd* is the complete postnatal degeneration of cerebellar Purkinje cells and subsequent loss of granule cells and related structures (Mullen et al., 1976; Lalonde and Strazielle, 2007; Morton and Bastian, 2007). While, in *reeler* neurodegeneration is associated with abnormal localization of neurons, a failure of neuronal layer formation and a reduce number of cells in cerebellum. In light of these extensive anatomical defects and the existing body of literature on mouse ataxia, the remarkable preservation of forward paw motion in *pcd* (all four paw) and in *reeler* (only front paws) was surprising. Moreover, previous studies have associated Purkinje cell modulation with the step cycle of individual limbs (Armstrong and Edgley, 1984; Edgley and Lidierth, 1988; Udo et al., 2004) and movement kinematics (Pasalar et al., 2006; Heiney et al., 2014). The most likely interpretation of the surprisingly intact forward paw motion in *pcd* and *reeler* is that it reflects the presence of inevitable compensatory mechanisms. Given this capacity for compensation, the specific and persistent impairments in multi-joint, interlimb, and whole-body coordination in *pcd* and *reeler* are particularly striking.

While many lines of evidence suggest that the cerebellum provides internal models for motor control (Wolpert et al., 1998; Ito, 2008), there has been disagreement about the nature of these models (Ebner and Pasalar, 2008; Medina, 2011). Studies from some systems, including eye movements, have suggested that the cerebellum acts as an inverse model that computes a command to achieve desired movement (Shidara et al., 1993). Other work, particularly on reaching movements, the cerebellar-like nuclei of electric fish, and locomotor adaptation, has suggested that the cerebellum provides a forward model that predicts the consequences of movements (Bastian et al., 1996; Kennedy et al., 2014; Pasalar et al., 2006; Morton and Bastian, 2006). These predictions can then be used to optimize joint angle combinations within a limb (Bastian et al., 1996), synchronize interlimb coordination or to cancel out the unintended passive consequences of movements of other parts of the body. We found that while on-axis paw kinematics are preserved in the absence of cerebellar a normal function, the ability to predict and actively cancel the passive consequences of movements of other parts of the body appears to be beyond the limits of compensatory mechanisms available to *pcd* and *reeler* mice. Therefore, our results raise the intriguing possibility that the absence of forward models, rather than a failure to execute appropriate movement kinematics per se, could form the basis for impaired coordination associated with gait ataxia in mice.

Given the diversity of cerebellar phenotypes, it is expected that the specific features of gait ataxia will vary across mouse models (Lalonde and Strazielle, 2007). Strikingly, that was not the case when quantification on locomotor deficits in *reeler* mice was made. The neurodegeneration in *reeler* mice was not specific to the cerebellum region as it was in *pcd* mice. In addition, *pcd* mice neurodegeneration was pot-natal. Although *reeler* mice were visibly more ataxic than *pcd* mice, they share similar and specific core features. In *reeler* mice hind paws were completely altered at the level of the individual limb parameters. However, front paws are remarkably preserved, the rest of impairments are restricted to multi-joint, interlimb, and whole-body coordination like in *pcd* mice. The consistency of this features across cerebellar mutant mice strength our idea on cerebellar contributions to coordinated movement.

### Combining optogenetic tools with LocoMouse revealed specific gait parameters of the different cerebellar outputs

Most of what is known from medial-to-lateral organization and the contributions of different cerebellar regions to motor coordination comes from lesion experiments, ataxic mutant mice and patients with cerebellar disorders (Morton and Bastian 2007). These manipulations are chronic and irreversible. Furthermost, they are poorly spatially defined. Thus, lack of specificity and compensatory mechanisms are unavoidable (Morton and Bastian 2007).

Optogenetic tools allows us to manipulate the activity of selective neural populations. It combines genetics and optical methods to selectively stimulate or silence specific neurons with a high temporal precision and reversibility (Zhang et al., 2007). In this project, we combined optogenetic tools with the LocoMouse system to differentiate and quantify locomotor aspects associated with manipulation of different deep cerebellar nuclei.

Since it was not possible to genetically target the different deep cerebellar nuclei, we used L7CreChR2 mice to manipulate the cerebellar outputs. In these mice, ChR2 is expressed in Purkinje cells. Purkinje cells are the cerebellar cortex output and they inhibit the deep cerebellar nuclei. Therefore, buy activating Purkinje cells we can increase inhibition to the deep cerebellar nuclei.

Acute disruption of neural activity in DCN led to specific motor deficits associated to each nucleus. This was already expected from previous lesion and anatomy studies (Chambers and Sprague 1955). Activation of Purkinje cells terminals in the medial nucleus led to severe motor deficits across all four paws, reduce (in some animals almost immobilized) velocity and increase of the number of paws on the ground. These features suggest a posture and balance instability. These behavior is consistent with the medial nucleus projections (Morton and Bastian 2007). Medial nucleus projects to the ipsi vestibular nucleus and then to the medial motor system which will influencing the lateral vestibulaspinal tracks. Vestibulaspinal tracks are responsible to maintain posture and balance during ongoing movements (Sprague and Chambers 1953, Chambers and Sprague 1955). Interposed A nuclei manipulation revealed motor deficits at the level of the limb movement control. Both spatial and temporal parameters of the front right paw were specific altered (ipsilateral to nucleus manipulation). The interposed nuclei project to the red nucleus and to the thalamic nuclei. These nuclei then project directly to the lateral motor system. Finally, no deficits on ongoing movements during overground locomotion were observed in the lateral nucleus manipulation. The lateral nucleus projects to the lateral motor system, in particular, to the ventrolateral nucleus of the thalamus and then to the motor cortex (Asanuma, Thach et al. 1983). Lesions in this nucleus have suggested a role in the initiation of planned and complexed movements and not on the execution of ongoing movement of simple behavior such as walking in a straight line.

### LocoMouse applications: Motor impairments in spinal cord mutant mice and the effect of serotonin activation in motor coordination

*Spinal cord mutant mice: Mutation in the notch signaling pathway*

The LocoMouse allowed to describe in detail specific motor perturbations that resulted from deletion of the *Dll1* and/or *Dll4* ligands in the developing V2 domain of the spinal cord, therefore, contributing to the understanding of the role of Notch signaling pathway in neurogenesis. The main findings are related to impairments in intra-limb and tail parameters, while interlimb coordination was preserved. Alterations in histologic analysis of adult spinal cords are also consistent with the motor deficits. Manuscript in preparation: Alexandra I. Rosa*., Ana S. Machado*., Sara Ferreira, Domingos Henrique*., Megan R. Carey*., *Cell-fate decisions mediated by Notch signaling during spinal cord embryonic development affect motor performance of individual limbs and tail in adulthood*.

*Serotonin activation and its implications in motor coordination*

The LocoMouse system was used to access the effect of serotonin activation on motor coordination (data not showed in this thesis). In the this study, they found that activating dorsal raphe nucleus (DRN) 5-HT neurons induced a strong suppression of spontaneous locomotor behavior in the open field with rapid kinetics (onset ≤ 1 s). Inhibition of locomotion was independent of measures of anxiety or motor impairment and could be overcome by strong motivational drive. This work is in press at eLife (Patrícia A. Correia*, Eran Lottem*, Dhruba Banerjee, Ana S. Machado, Megan R. Carey, Zachary F. Mainen, *Transient inhibition and long-term facilitation of locomotion by phasic optogenetic activation of serotonin neurons*, submitted)

### Cerebellar contributions to coordinated locomotion

It is interesting to consider that both cerebellar mutant mice (chronic manipulation) and mice with acute manipulations revealed perturbations in limb interjoint coordination, interlimb coordination and tail segment oscillation.

Acute manipulation through Purkinje cells activation led to motor deficits during individual limb movements. These findings are consistent with studies that associated Purkinje cells modulation with the step cycle of individual limbs (Armstrong and Edgley, 1984; Edgley and Lidierth, 1988; Udo et al., 2004) and movement kinematics (Pasalar et al., 2006; Heiney et al., 2014). However, *pcd* and *reeler* mice showed an intact forward paw motion. The differences between these two manipulations could be explained by differences between chronic and acute manipulation. As it was previous mentioned, the most likely interpretation of the surprisingly intact forward paw motion in *pcd* and *reeler* mice is that it reflects the presence of inevitable compensatory mechanisms.

In addition to this, during acute manipulation the limbs movement amplitude (z) was suppressed, while in the chronic manipulation limbs movement amplitude increased. A similar observation was found in the tail oscillation. This could be explained by the fact that in *pcd* and *reeler* mice Purkinje cells were absent or reduced, whereas in the acute manipulation Purkinje cells were activated, suggesting a potential role of Purkinje cells in movement amplitude modulation. In any case, both manipulations chronic and acute revealed impairments in the same core features.

Comparisons between cerebellar ataxic mice with spinal cord mutant mice and (mice with activation of 5-HT neurons – not shown) allowed us to differentiate and strength our findings on cerebellum-dependent locomotor parameters. Spinal cord mutant mice revealed specific impairments at the intralimb level, while in cerebellar mutant mice the motor perturbations were more restricted to impairments on coordinating movements across whole body. No motor deficits were found during 5-HT neurons activation. We characterized distinct motor deficits associated with manipulations in different brain regions and identified and quantified core features of cerebellar ataxia in mice.

## Future work

Due to the different domains embraced in this thesis, suggestions for future work are divided according to the following categories: (i) tracking improvement; (ii) optimizing DCN manipulation; (iii) Apply the quantitative framework for mouse locomotion that we have developed to other mouse mutants and manipulations.

(i) Tracking improvement:

- Speedup the tracking process (ideally to real-time);
- Improve the SVM feature detector by incorporating a larger training set of good and bad tracks;
- Apply new algorithms techniques like convolutional neural networks to increase the detection accuracy of the different mouse body parts;
- Expand the tracking system to other experimental conditions, e.g. treadmill, ladders. In addition, apply the tracking system to non-black 6 mice.

(ii) Optimize DCN manipulation:

- Fine-tuning the stimulation conditions for each deep cerebellar nucleus;
- Improving data analysis to precise temporal manipulation.

(iii) Apply the quantitative framework for mouse locomotion that we have developed to other mouse mutants and manipulations.

## Concluding remarks

In conclusion, the novel quantitative framework for mouse locomotion presented in this project highlights the importance of considering 3D, interlimb and whole-body coordination and dissociating them from the control of individual paw kinematics, particularly when analyzing cerebellar contributions to locomotion. Together with the sophisticated genetic tools available for manipulating neural circuits in mice, the current approach makes mouse locomotion a powerful system for investigating the neural control of coordinated movement and establishing relationships between neural circuit activity and behavior.

# References

Anderson, D. J. and P. Perona (2014). "Toward a science of computational ethology." Neuron 84(1): 18-31.

Armstrong, D. M. (1986). "Supraspinal contributions to the initiation and control of locomotion in the cat." Prog. Neurobiol. 26: 273-361.

Asanuma, C., W. Thach and E. Jones (1983). "Anatomical evidence for segregated focal groupings of efferent cells and their terminal ramifications in the cerebellothalamic pathway of the monkey." Brain Research Reviews 5(3): 267-297.

Asanuma, C., W. Thach and E. Jones (1983). "Distribution of cerebellar terminations and their relation to other afferent terminations in the ventral lateral thalamic region of the monkey." Brain Research Reviews 5(3): 237-265.

Azim, E., J. Jiang, B. Alstermark and T. M. Jessell (2014). "Skilled reaching relies on a V2a propriospinal internal copy circuit." Nature 508: 357-363.

Basso, D. M., L. C. Fisher, A. J. Anderson, L. B. Jakeman, D. M. Mctigue and P. G. Popovich (2006). "Basso Mouse Scale for locomotion detects differences in recovery after spinal cord injury in five common mouse strains." Journal of neurotrauma 23(5): 635-659.

Bastian, A., T. Martin, J. Keating and W. Thach (1996). "Cerebellar ataxia: abnormal control of interaction torques across multiple joints." Journal of Neurophysiology 76(1): 492-509.

Bates, D., M. Maechler, B. Bolker and S. Walker (2014). "lme4: Linear mixed-effects models using Eigen and S4." R package version 1(7).

Batka, R. J., T. J. Brown, K. P. Mcmillan, R. M. Meadows, K. J. Jones and M. M. Haulcomb (2014). "The need for speed in rodent locomotion analyses." The Anatomical Record 297(10): 1839-1864.

Beckers, M.-C., I. Bar, T. Huynh-Thu, C. Dernoncourt, A. L. Brunialti, X. Montagutelli, J.-L. Guénet and A. M. Goffinet (1994). "A high-resolution genetic map of mouse chromosome 5 encompassing the reeler (rl) locus." Genomics 23(3): 685-690.

Bellardita, C. and O. Kiehn (2015). "Phenotypic characterization of speed-associated gait changes in mice reveals modular organization of locomotor networks." Current Biology 25(11): 1426-1436.

Blatt, G. J. and L. M. Eisenman (1988). "Topographic and zonal organization of the olivocerebellar projection in the reeler mutant mouse." Journal of Comparative Neurology 267(4): 603-615.

Brooks, S. P. and S. B. Dunnett (2009). "Tests to assess motor phenotype in mice: a user's guide." Nature Reviews Neuroscience 10(7): 519-529.

Brown, T. G. (1911). "The intrinsic factors in the act of progression in the mammal." Proceedings of the Royal Society of London. Series B, containing papers of a biological character 84(572): 308-319.

Brown, T. G. (1914). "On the nature of the fundamental activity of the nervous centres; together with an analysis of the conditioning of rhythmic activity in progression, and a theory of the evolution of function in the nervous system." The Journal of Physiology 48(1): 18-46.

Camera, D., N. A. Boase, S. Kumar, D. V. Pow and P. Poronnik (2014). "Subtle gait abnormalities in Nedd4 heterozygous mice." Behavioural brain research 260: 15-24.

Castagna, C., P. Aimar, S. Alasia and L. Lossi (2014). "Post-natal development of the Reeler mouse cerebellum: an ultrastructural study." Annals of Anatomy-Anatomischer Anzeiger 196(4): 224-235.

Cendelin, J. (2014). "From mice to men: lessons from mutant ataxic mice." Cerebellum & Ataxias 1(1): 4.

Cendelín, J., J. Voller and F. Vožeh (2010). "Ataxic gait analysis in a mouse model of the olivocerebellar degeneration." Behavioural brain research 210(1): 8-15..

Chambers, W. W. and J. M. Sprague (1955). "Functional localization in the cerebellum: Somatotopic organization in cortex and nuclei." AMA Archives of Neurology & Psychiatry 74(6): 653-680.

Chen, L., S. Bao, J. M. Lockard, J. Kim and R. F. Thompson (1996). "Impaired classical eyeblink conditioning in cerebellar-lesioned and Purkinje cell degeneration (pcd) mutant mice." The Journal of Neuroscience 16(8): 2829-2838.

Clark, D. A., L. Freifeld and T. R. Clandinin (2013). "Mapping and cracking sensorimotor circuits in genetic model organisms." Neuron 78(4): 583-595.

Clarke, K. and J. Still (1999). "Gait analysis in the mouse." Physiology & behavior 66(5): 723-729.

Clendenin, M., C.-F. Ekerot, O. Oscarsson and I. Rosen (1974). "The lateral reticular nucleus in the cat I. Mossy fibre distribution in cerebellar cortex." Experimental brain research 21(5): 473-486.

Crone, S. A. (2008). "Genetic ablation of V2a ipsilateral interneurons disrupts left-right motor coordination in mammalian spinal cord." Neuron 60: 70-83.

Crone, S. A., G. Zhong, R. Harris-Warrick and K. Sharma (2009). "In mice lacking V2a interneurons, gait depends on speed of locomotion." The Journal of Neuroscience 29(21): 7098-7109.

Crosby, E. C. (1962). Correlative anatomy of the nervous system, Macmillan.

Dale, N. and F. M. Kuenzi (1997). "Ion channels and the control of swimming in the Xenopus embryo." Prog. Neurobiol. 35: 729-756.

De Zeeuw, C. I. and C. H. Yeo (2005). "Time and tide in cerebellar memory formation." Current opinion in neurobiology 15(6): 667-674.

De Zeeuw, C. I., C. Hansel, F. Bian, S. K. Koekkoek, A. M. Van Alphen, D. J. Linden and J. Oberdick (1998). "Expression of a protein kinase C inhibitor in Purkinje cells blocks cerebellar LTD and adaptation of the vestibulo-ocular reflex." Neuron 20(3): 495-508.

Dickinson, M. H. (2000). "How animals move: an integrative view." Science 288: 100-106.

Dorman, C. W., H. E. Krug, S. P. Frizelle, S. Funkenbusch and M. L. Mahowald (2014). "A comparison of DigiGait™ and TreadScan™ imaging systems: assessment of pain using gait analysis in murine monoarthritis." Journal of pain research 7: 25.

Dougherty, K. J., L. Zagoraiou, D. Satoh, I. Rozani, S. Doobar, S. Arber, T. M. Jessell and O. Kiehn (2013). "Locomotor rhythm generation linked to the output of spinal shox2 excitatory interneurons." Neuron 80(4): 920-933.

Drew, T. and D. S. Marigold (2015). "Taking the next step: cortical contributions to the control of locomotion." Curr. Opin. Neurobiol. 33: 25-33.

Drew, T., S. Prentice and B. Schepens (2004). "Cortical and brainstem control of locomotion." Prog. Brain Res. 143: 251-261.

Dubuc, R. (2008). "Initiation of locomotion in lampreys." Brain Res. Rev. 57: 172-182.

Earhart, G. M. and A. J. Bastian (2001). "Selection and coordination of human locomotor forms following cerebellar damage." Journal of Neurophysiology 85(2): 759-769.

Eccles, J. C. (2013). The cerebellum as a neuronal machine, Springer Science & Business Media.

Falconer, D. (1951). "Two new mutants,'trembler'and 'reeler', with neurological actions in the house mouse (Mus musculus L.)." Journal of genetics 50(2): 192-205.

Fernandez-Gonzalez, A., A. R. La Spada, J. Treadaway, J. C. Higdon, B. S. Harris, R. L. Sidman, J. I. Morgan and J. Zuo (2002). "Purkinje cell degeneration (pcd) phenotypes caused by mutations in the axotomy-induced gene, Nna1." Science 295(5561): 1904-1906.

Fortier, P., A. Smith and S. Rossignol (1987). "Locomotor deficits in the mutant mouse, Lurcher." Experimental brain research 66(2): 271-286.

Garnier, C., M. Falempin and M.-H. Canu (2008). "A 3D analysis of fore-and hindlimb motion during locomotion: comparison of overground and ladder walking in rats." Behavioural brain research 186(1): 57-65.

Goffinet, A., K.-F. So, M. Yamamoto, M. Edwards and V. Caviness (1984). "Architectonic and hodological organization of the cerebellum in reeler mutant mice." Developmental Brain Research 16(2): 263-276.

Gorska, T., W. Zmysłowski and H. Majczyński (1998). "Overground locomotion in intact rats: interlimb coordination, support patterns and support phases duration." Acta neurobiologiae experimentalis 59(2): 131-144.

Goulding, M. (2009). "Circuits controlling vertebrate locomotion: moving in a new direction." Nat Rev Neurosci 10(7): 507-518.

Grillner, S. (1975). "Locomotion in vertebrates: central mechanisms and reflex interactions." Physiol. Rev. 55: 247-304.

Grillner, S. (2003). "The motor infrastructure: from ion channels to neuronal networks." Nature Rev. Neurosci. 4: 573-586.

Grillner, S. and T. M. Jessell (2009). “Measured Motion: Searching for Simplicity in Spinal Locomotor Networks.” Curr. Opin. Neurobiol. 19(6): 572–586.

Guillot, T. S., S. A. Asress, J. R. Richardson, J. D. Glass and G. W. Miller (2008). "Treadmill gait analysis does not detect motor deficits in animal models of Parkinson's disease or amyotrophic lateral sclerosis." Journal of motor behavior 40(6): 568-577.

Hamburgh, M. (1963). "Analysis of the postnatal developmental effects of “reeler,” a neurological mutation in mice. A study in developmental genetics." Developmental biology 8(2): 165-185.

Hamers, F. P., A. J. Lankhorst, T. J. van Laar, W. B. Veldhuis and W. H. Gispen (2001). "Automated quantitative gait analysis during overground locomotion in the rat: its application to spinal cord contusion and transection injuries." Journal of neurotrauma 18(2): 187-201.

Herbin, M., R. Hackert, J.-P. Gasc and S. Renous (2007). "Gait parameters of treadmill versus overground locomotion in mouse." Behavioural brain research 181(2): 173-179.

Hozumi, K., N. Negishi, D. Suzuki, N. Abe, Y. Sotomaru, N. Tamaoki, C. Mailhos, D. Ish-Horowicz, S. Habu and M. J. Owen (2004). "Delta-like 1 is necessary for the generation of marginal zone B cells but not T cells in vivo." Nat Immunol 5(6): 638-644.

Ito, M. (1972). "Neural design of the cerebellar motor control system." Brain research 40(1): 81-84.

Itō, M. (1984). The cerebellum and neural control, Raven Pr.

Jansen, J. and A. Brodal (1940). "Experimental studies on the intrinsic fibers of the cerebellum. II. The cortico-nuclear projection." Journal of Comparative Neurology 73(2): 267-321.

Jordan, L. M. (1998). "Initiation of locomotion in mammals." Ann. NY Acad. Sci. 860: 83-93.

Jordan, L. M., J. Liu, P. B. Hedlund, T. Akay and K. G. Pearson (2008). "Descending command systems for the initiation of locomotion in mammals." Brain Res. Rev. 57: 183-191.

Kale, A., I. Amende, G. P. Meyer, J. C. Crabbe and T. G. Hampton (2004). "Ethanol's effects on gait dynamics in mice investigated by ventral plane videography." Alcoholism: Clinical and Experimental Research 28(12): 1839-1848.

Kandel, E. R., J. H. Schwartz, T. M. Jessell, S. A. Siegelbaum and A. Hudspeth (2000). Principles of neural science, McGraw-hill New York.

Kang, W.-Y., S.-S. Kim, S.-K. Cho, S. Kim, H. Suh-Kim and Y.-D. Lee (2010). "Migratory defect of mesencephalic dopaminergic neurons in developing reeler mice." Anatomy & cell biology 43(3): 241-251.

Kasper, J., R. Schor and V. Wilson (1988). "Response of vestibular neurons to head rotations in vertical planes. I. Response to vestibular stimulation." Journal of neurophysiology 60(5): 1753-1764.

Kiehn, O. (2006). "Locomotor circuits in the mammalian spinal cord." Ann. Rev. Neurosci. 29: 279-306.

Kiehn, O. (2011). "Development and functional organization of spinal locomotor circuits." Curr. Opin. Neurobiol. 21: 100-109.

Kiehn, O. (2016). "Decoding the organization of spinal circuits that control locomotion." Nat Rev Neurosci 17(4): 224-238.

Kim, J. C., M. N. Cook, M. R. Carey, C. Shen, W. G. Regehr and S. M. Dymecki (2009). "Linking genetically defined neurons to behavior through a broadly applicable silencing allele." Neuron 63(3): 305-315.

Koch, U., E. Fiorini, R. Benedito, V. Besseyrias, K. Schuster-Gossler, M. Pierres, N. R. Manley, A. Duarte, H. R. Macdonald and F. Radtke (2008). "Delta-like 4 is the essential, nonredundant ligand for Notch1 during thymic T cell lineage commitment." J Exp Med 205(11): 2515-2523.

Koopmans, G. C., R. Deumens, G. Brook, J. Gerver, W. M. Honig, F. P. Hamers and E. A. Joosten (2007). "Strain and locomotor speed affect over-ground locomotion in intact rats." Physiology & behavior 92(5): 993-1001

Kotchabhakdi, N. and F. Walberg (1978). "Cerebellar afferent projections from the vestibular nuclei in the cat: an experimental study with the method of retrograde axonal transport of horseradish peroxidase." Experimental brain research 31(4): 591-604.

Lalonde, R. and C. Strazielle (2007). "Brain regions and genes affecting postural control." Progress in neurobiology 81(1): 45-60.

Lawrence, D. G. and H. G. Kuypers (1968). "The functional organization of the motor system in the monkey." Brain 91(1): 15-36.

Le Marec, N. and R. Lalonde (1997). "Sensorimotor learning and retention during equilibrium tests in Purkinje cell degeneration mutant mice." Brain research 768(1): 310-316.

Leblond, H., M. L'Espérance, D. Orsal and S. Rossignol (2003). "Treadmill locomotion in the intact and spinal mouse." The Journal of neuroscience 23(36): 11411-11419.

Lisberger, S. (1988). "The neural basis for motor learning in the vestibulo-ocular reflex in monkeys." Trends in neurosciences 11(4): 147-152.

Lisberger, S. and W. Thach (2013). "The cerebellum." Principles of Neural Science: 960-981.

Lisberger, S. G. (2009). "Internal models of eye movement in the floccular complex of the monkey cerebellum." Neuroscience 162(3): 763-776.

Louvi, A. and S. Artavanis-Tsakonas (2006). "Notch signalling in vertebrate neural development." Nature Reviews Neuroscience 7(2): 93-102.

Luo, L., E. M. Callaway and K. Svoboda (2008). "Genetic dissection of neural circuits." Neuron 57(5): 634-660.

Machado, A. S., D. M. Darmohray, J. Fayad, H. G. Marques and M. R. Carey (2015). "A quantitative framework for whole-body coordination reveals specific deficits in freely walking ataxic mice." eLife 4: e07892.

Manto, M. and D. Marmolino (2009). "Animal models of human cerebellar ataxias: a cornerstone for the therapies of the twenty-first century." The Cerebellum 8(3): 137-154.

Marder, E. and D. Bucher (2001). "Central pattern generators and the control of rhythmic movements." Curr. Biol. 11: R986-R996.

Marple-Horvat, D., J. Criado and D. Armstrong (1998). "Neuronal activity in the lateral cerebellum of the cat related to visual stimuli at rest, visually guided step modification, and saccadic eye movements." The Journal of Physiology 506(2): 489-514.

Matsushita, M., N. Okado, Y. Hosoya and M. Ikeda (1981). "Descending projections from the spinal and mesencephalic nuclei of the trigeminal nerve to the spinal cord in the cat. A study with the horseradish peroxidase technique." Journal of Comparative Neurology 196(2): 173-187.

Mauk, M. and W. Thach (2008). "Cerebellum." Fundamental Neuroscience 3: 751-774.

Mendes, C. S., I. Bartos, T. Akay, S. Márka and R. S. Mann (2013). "Quantification of gait parameters in freely walking wild type and sensory deprived Drosophila melanogaster." Elife 2: e00231.

Mendes, C. S., I. Bartos, Z. Márka, T. Akay, S. Márka and R. S. Mann (2015). "Quantification of gait parameters in freely walking rodents." BMC biology 13(1): 1.

Mikoshiba, K., S. Kohsaka, K. Takamatsu, E. Aoki and Y. Tsukada (1980). "Morphological and biochemical studies on the cerebral cortex from reeler mutant mice: development of cortical layers and metabolic mapping by the deoxyglucose method." Journal of neurochemistry 34(4): 835-844.

Morton, S. M. and A. J. Bastian (2006). "Cerebellar contributions to locomotor adaptations during splitbelt treadmill walking." The Journal of neuroscience 26(36): 9107-9116.

Morton, S. M. and A. J. Bastian (2007). "Mechanisms of cerebellar gait ataxia." The Cerebellum 6(1): 79-86.

Mullen, R. J., E. M. Eicher and R. L. Sidman (1976). "Purkinje cell degeneration, a new neurological mutation in the mouse." Proceedings of the National Academy of Sciences 73(1): 208-212.

Nakagawa, S. and H. Schielzeth (2013). "A general and simple method for obtaining R2 from generalized linear mixed-effects models." Methods in Ecology and Evolution 4(2): 133-142.

Nguyen-Vu, T. B., R. R. Kimpo, J. M. Rinaldi, A. Kohli, H. Zeng, K. Deisseroth and J. L. Raymond (2013). "Cerebellar Purkinje cell activity drives motor learning." Nature neuroscience 16(12): 1734-1736.

Orlovsky, G. N., T. G. Deliagina and S. Grillner (1999). Neural Control of Locomotion. From mollusc to man, Nature Publishing Group.

Palliyath, S., M. Hallett, S. L. Thomas and M. K. Lebiedowska (1998). "Gait in patients with cerebellar ataxia." Movement disorders 13(6): 958-964.

Pearson, K. G. (2004). "Generating the walking gait: role of sensory feedback." Prog. Brain Res. 143: 123-129.

Peng, C. Y., H. Yajima, C. E. Burns, L. I. Zon, S. S. Sisodia, S. L. Pfaff and K. Sharma (2007). "Notch and MAML signaling drives Scl-dependent interneuron diversity in the spinal cord." Neuron 53(6): 813-827.

Purves, D., G. Augustine, D. Fitzpatrick, W. Hall, A. LaMantia and L. White "Neuroscience. 2012." Sunderland, Mass.: Sinauer Associates.

Ramos, C., S. Rocha, C. Gaspar and D. Henrique (2010). "Two Notch ligands, Dll1 and Jag1, are differently restricted in their range of action to control neurogenesis in the mammalian spinal cord." PloS one 5(11): e15515.

Raymond, J. L., S. G. Lisberger and M. D. Mauk (1996). "The cerebellum: a neuronal learning machine?" Science 272(5265): 1126.

Rocha, S. F., S. S. Lopes, A. Gossler and D. Henrique (2009). "Dll1 and Dll4 function sequentially in the retina and pV2 domain of the spinal cord to regulate neurogenesis and create cell diversity." Developmental biology 328(1): 54-65.

Rossignol, S., R. Dubuc and J. P. Gossard (2005). "Dynamic sensorimotor interactions in locomotion." Physiol. Rev. 86: 89-154.

Russell, C., L. de Agapito and F. Setti (2011). Efficient Second Order Multi-Target Tracking with Exclusion Constraints. BMVC, Citeseer

Sheets, A. L., P.-L. Lai, L. C. Fisher and D. M. Basso (2013). "Quantitative evaluation of 3D mouse behaviors and motor function in the open-field after spinal cord injury using markerless motion tracking." PloS one 8(9): e74536.

Sheets, A. L., P.-L. Lai, L. C. Fisher and D. M. Basso (2013). "Quantitative evaluation of 3D mouse behaviors and motor function in the open-field after spinal cord injury using markerless motion tracking." PloS one 8(9): e74536.

Shik, M. L. and G. N. Orlovsky (1976). "Neurophysiology of locomotor automatism." Physiological reviews 56(3): 465-501.

Shik, M., F. Severin and O. GN (1966). "Control of walking and running by means of electrical stimulation of mid-brain." BIOPHYSICS-USSR 11(4): 756-&.

Silvia Arber (2012). “Motor Circuits in Action: Specification, Connectivity, and Function, Neuron.“ Neuron 74(6): 975-989.

Sprague, J. M. and W. W. Chambers (1953). "Regulation of posture in intact and decerebrate cat: I. Cerebellum, reticular formation, vestibular nuclei." Journal of neurophysiology 16(5): 451-463.

Stanfield, B. B. and W. M. Cowan (1979). "The morphology of the hippocampus and dentate gyrus in normal and reeler mice." Journal of Comparative Neurology 185(3): 393-422.

Stolze, H., S. Klebe, G. Petersen, J. Raethjen, R. Wenzelburger, K. Witt and G. Deuschl (2002). "Typical features of cerebellar ataxic gait." Journal of Neurology, Neurosurgery & Psychiatry 73(3): 310-312.

Stroobants, S., I. Gantois, T. Pooters and R. D'Hooge (2013). "Increased gait variability in mice with small cerebellar cortex lesions and normal rotarod performance." Behavioural brain research 241: 32-37.

Suidan, G. L., D. Duerschmied, G. M. Dillon, V. Vanderhorst, T. G. Hampton, S. L. Wong, J. R. Voorhees and D. D. Wagner (2013). "Lack of tryptophan hydroxylase-1 in mice results in gait abnormalities." PloS one 8(3): e59032.

Terashima, T., Y. Inoue, K. Inoue, K. Mikoshiba and Y. Tsukada (1983). "Distribution and morphology of corticospinal tract neurons in reeler mouse cortex by the retrograde HRP method." Journal of Comparative Neurology 218(3): 314-326.

Thach, W. T., H. Goodkin and J. Keating (1992). "The cerebellum and the adaptive coordination of movement." Annual review of neuroscience 15(1): 403-442.

Tronche, F., C. Kellendonk, O. Kretz, P. Gass, K. Anlag, P. C. Orban, R. Bock, R. Klein and G. Schutz (1999). "Disruption of the glucocorticoid receptor gene in the nervous system results in reduced anxiety." Nat Genet 23(1): 99-103.

Udo, M., K. Matsukawa and H. Kamei (1979). "Effects of partial cooling of cerebellar cortex at lobules V and IV of the intermediate part in the decerebrate walking cats under monitoring vertical floor reaction forces." Brain research 160(3): 559-564.

Udo, M., K. Matsukawa, H. Kamei and Y. Oda (1980). "Cerebellar control of locomotion: effects of cooling cerebellar intermediate cortex in high decerebrate and awake walking cats." Journal of Neurophysiology 44(1): 119-134.

Veloz, M. F. V., K. Zhou, L. W. Bosman, J.-W. Potters, M. Negrello, R. M. Seepers, C. Strydis, S. K. Koekkoek and C. I. De Zeeuw (2015). "Cerebellar control of gait and interlimb coordination." Brain Structure and Function 220(6): 3513-3536.

Voogd, J. and M. Glickstein (1998). "The anatomy of the cerebellum." Trends in cognitive sciences 2(9): 307-313.

Walter, J. T., K. Alvina, M. D. Womack, C. Chevez and K. Khodakhah (2006). "Decreases in the precision of Purkinje cell pacemaking cause cerebellar dysfunction and ataxia." Nature neuroscience 9(3): 389-397.

Wang, T., J. Parris, L. Li and J. I. Morgan (2006). "The carboxypeptidase-like substrate-binding site in Nna1 is essential for the rescue of the Purkinje cell degeneration (pcd) phenotype." Molecular and Cellular Neuroscience 33(2): 200-213.

Wilson, D. and R. Wyman (1965). "Motor output patterns during random and rhythmic stimulation of locust thoracic ganglia." Biophysical Journal 5(2): 121.

Wuehr, M., R. Schniepp, J. Ilmberger, T. Brandt and K. Jahn (2013). "Speed-dependent temporospatial gait variability and long-range correlations in cerebellar ataxia." Gait & posture 37(2): 214-218.

Yu, J. and E. Eidelberg (1983). "Recovery of locomotor function in cats after localized cerebellar lesions." Brain research 273(1): 121-131.

Zhang, F., A. M. Aravanis, A. Adamantidis, L. de Lecea and K. Deisseroth (2007). "Circuit-breakers: optical technologies for probing neural signals and systems." Nature Reviews Neuroscience 8(8): 577-581.

Zörner, B., L. Filli, M. L. Starkey, R. Gonzenbach, H. Kasper, M. Röthlisberger, M. Bolliger and M. E. Schwab (2010). "Profiling locomotor recovery: comprehensive quantification of impairments after CNS damage in rodents." Nature methods 7(9): 701-708.